THE TWO-FLUID MODEL WITH INTERFACIAL AREA TRANSPORT EQUATION IN GAS-DISPERSED CONDENSING FLOWS

BY

VINEET KUMAR

DISSERTATION

Submitted in partial fulfillment of the requirements
for the degree of Doctor of Philosophy in Nuclear, Plasma and Radiological Engineering
in the Graduate College of the
University of Illinois at Urbana-Champaign, 2019

Urbana, Illinois

Doctoral Committee:

Assistant Professor Caleb Brooks, Chair
Professor Rizwan Uddin
Associate Professor Tomasz Kozlowski
Professor Emeritus Surya Pratap Vanka

ABSTRACT

The interfacial area transport equation (IATE) has been proposed to satisfy the closure of the interfacial area concentration in the two-fluid model. The IATE provides a dynamic prediction of flow structure consistent with the two-fluid model and has been studied extensively for adiabatic two-phase flows. However, the IATE still requires attention in flows with phase change, specifically the benchmarking of the IATE in condensing gas-dispersed bubbly flows. Extending the analysis to condensing cap/slug flows, in the present two-group IATE model formulation, the inter-group mass transfer term, which is critical for proper accounting of the bubble groups, only considers the expansion of group-1 bubbles (spherical and distorted bubbles) to group-2 bubbles (cap, slug and churn-turbulent bubbles). In condensing flows, the inter-group mass transfer term is dominated by group-2 bubbles condensing to group-1 bubbles. Therefore, the modeling of the condensation interfacial area and volume sink term is revisited, and by coupling the IATE and continuity equations the sensitivity of modeling parameters is directly investigated.

A new annulus facility is built in which experimental adiabatic steam-water flow data is collected which includes gas-dispersed condensing flow data for validating the proposed one-group and two-group condensation model. The facility includes five instrumentation ports located in the unheated section to provide high-resolution two-phase measurements in addition to local pressure and local liquid temperature measurements. The dataset consists of a total of eighty-five conditions spanning across system pressures, mass fluxes, inlet liquid subcooling, and inlet void fractions. The new dataset is developed for validation of one-dimensional system codes and multi-dimensional fluid dynamics codes and fills an important gap in the adiabatic steam-water flow database literature.

Three datasets have been used for validation consisting of condensing two-phase flow data in the unheated section of a vertical annulus with conditions spanning a range of pressures, inlet subcoolings and mass fluxes. For bubbly flows, the coupled void transport - IATE simulation results in good agreement in the predictions of the void fraction and the interfacial area concentration under nearly all sixty conditions with the proposed modifications to the condensation model. Considering the two-group two-fluid IATE model formulation, the inter-group mass transfer term is modified to be applicable for all flow conditions. The group-2 Nusselt number correlation is also modified to account for the appropriate heat transfer length scale for group-2 bubbles. A second inter-group transfer coefficient is introduced for the proposed model, and a closure relation is provided. Validation of the proposed two-group two-fluid model against the new dataset shows good agreement with experimental data with the significant improvement over the

one-group IATE model for conditions with substantial group-2 void fraction throughout the simulation domain.

ACKNOWLEDGEMENTS

I am enormously grateful to my advisor, Professor Brooks, for his guidance, support and mentorship throughout the PhD program and for giving me this wonderful opportunity. His commitment and dedication has inspired me to strive to do better in my career.

I appreciate the support and the valuable inputs from my other committee members: Professor Rizwan Uddin, Professor Tomasz Kozlowski, and Professor Surya Pratap Vanka.

I would like to sincerely thank all my Multiphase Thermo-fluid Dynamics Laboratory (MTDL) colleagues, past and present, especially Zhiee Jhia Ooi, Joe Bottini, and Nate Colgan, without whose support and assistance wouldn't have allowed me to complete my research.

I owe a huge debt of gratitude to the staff at the Machine shop for their help in putting together the parts for the experimental test facility which I used for my graduate work. A special note of thanks to the administrative staff at the graduate office for their prompt assistance in addressing any queries I had regarding the PhD program.

I am grateful to my friends and family for their continuous support and encouragement over the years.

Lastly, I would like to acknowledge two departmental fellowships which helped support my graduate work: the Barclay Jones Fellowship and the Felix T. Adler Fellowship. I would also like to thank the DOE for providing support through the NEUP program (Project ID: DOE-16-10630) which provided funding for the construction of the experimental facility as well as funding a summer internship to Idaho National Laboratory.

TABLE OF CONTENTS

NOMENCLATURE

A	area [m^2]
a_i	interfacial area concentration [1/m]
C_{ct}	bubble interface roughness factor [-]
C_o	distribution parameter [-]
C_∞	asymptotic value of the distribution parameter [-]
c_p	specific heat capacity [J/kg-K]
D	diameter [m]
D_c	critical bubble diameter [m]
D_h	hydraulic diameter [m]
f	particle distribution function [m^{-6}]
g	acceleration due to gravity [m/s^2]
G	mass flux [kg/m^2-s]
h	specific enthalpy [J/kg]
h_c	condensation heat transfer coefficient [W/m^2-K]
h_{fg}	latent heat of vaporization [J/kg]
Ja	Jakob number [-]
j	superficial velocity [m/s]
k	thermal conductivity [W/m-K]
L_c	heat transfer length scale [m]
m	mass [kg]
Nu_c	condensation Nusselt number [-]
P	pressure [Pa]
Pr	Prandtl number [-]
p_c	fraction of bubbles in the inertially controlled region [-]
Re	Reynolds number [-]
S	particle source per unit mixture volume [m^{-6}]
U	rise velocity [m/s]
v	local velocity [m/s]
t	time [s]
T	temperature [K]
W_G	channel gap width [m]
z	axial location [m]

Greek

α	void fraction [-]
α_t	thermal diffusivity [m^2/s]
β	non-dimensional boundary diameter [-]
Γ	mass generation rate per unit volume [kg/m^3-s]
ΔT_{sub}	liquid subcooling [K]
Δz	node length [m]
ε	turbulent eddy dissipation rate [m^2/s^3]
η	condensation volume sink term [kg/m^3-s]
κ	group-2 shape coefficient [-]
μ	dynamic viscosity [Pa-s]
ξ	non-dimensional bubble volume [-]
ρ	density [kg/m^3]
σ	surface tension [N/m]
ϕ	interfacial area source/sink term [1/m-s]
χ	inter-group mass transfer coefficient [-]

ψ	shape factor [-]

Subscripts

b	boundary/bubbly flow regime
bc	boundary
CO	inertially controlled condensation
Conv	convection
c	critical
DP	pressure change
f	liquid condition
g	vapor condition
in	inlet or inflow condition
j	interface
max	maximum
min	minimum
PC	thermally controlled condensation
p	peak
RC	random collision
SO	shearing off
sat	saturation condition
Sm	Sauter Mean
TI	turbulent impact
t	total
WN	wall nucleation
WE	wake entrainment

Mathematical symbols

‹ ›	area averaged quantity
« »	void fraction weighted area averaged quantity
max()	maximum function
min()	minimum function

LIST OF TABLES

LIST OF FIGURES

CHAPTER 1. INTRODUCTION

Two-phase flows are ubiquitous in engineering systems across industries spanning energy, transport, process plants, etc. A good understanding of two-phase flows is required for efficient design of engineering systems and prediction of their operational safety limits. The multiscale nature of two-phase flows, especially phase-change flows, have posed considerable challenges in developing a broad theoretical understanding of them. However, over the years modeling techniques for two-phase flows have significantly improved, and the current focus is on rigorous verification and validation of these simulation tools. In this chapter, the importance of modeling gas-dispersed condensing flows is highlighted through experimental and computational approaches.

1.1. Significance

The design and accurate modeling of two-phase flow are important in predicting the thermohydraulic phenomenon in various engineering systems. Often these systems are very large with complex geometries, and full-scale experimentation is expensive and time consuming. Therefore, accurate two-phase-flow models tested and validated with scaled experiments are important. Considerable progress in two-phase flow modeling has been achieved over the past fifty years, especially for gas-dispersed flow with the establishment of a theoretical framework and development of constitutive relationships.

The main difficulties in the modeling of two-phase flow in terms of the local instant formulation based on single-phase flow formulation arise from the presence of multiple, deformable, moving interfaces which make the problem mathematically and numerically intractable. Therefore, some sort of averaging procedure is required to obtain a macroscopic formulation and to partially eliminate the burden of resolving the local instant features. Furthermore, there exist multiple scales in a two-phase flow, and it is necessary to consider the cascading effects of the different flow physics at various scales, principally classified as: system scale where system transients and component interactions are important, macroscopic scale required for two-phase flow structures and transport of mass, momentum and energy, mesoscale where interfacial exchanges of mass, momentum and energy are considered and finally, microscopic scale where fine structures, wall nucleation, condensation, molecular transport etc. are defined (Ishii and Hibiki, 2011). The two-fluid model (Ishii and Hibiki, 2011) is considered the most rigorously defined macroscopic formulation of the thermo-fluid dynamics of two-phase flow

systems either in its full three-dimensional representation or area-averaged one-dimensional equations.

The two-fluid model forms the backbone of reactor safety codes which have become increasingly relied upon for determination of safety margins, course of accident progression, design of new reactor concepts and systems, regulatory justification, as well as recovery of conservatism imposed by regulations. Even with the emergence of higher-fidelity computational tools such as CFD, the complexity of full-scale nuclear reactors will continue to demand accurate system codes for practical engineering solutions. Safety analysis codes continue to play an important role in reactor analysis given the diversity of system phenomena and wide range of system conditions. It remains critical for current and future reactor concepts that safety analysis codes such as RELAP5 and TRACE continue to be improved through better modeling and comprehensive validation. With the increasing push towards long-term passive cooling systems based on natural circulation, it is important to obtain a better understanding of the two-phase flow operational regime at low-pressure, low-flow conditions. Recent application of the RELAP5/MOD 3.3 code (Fullmer et al., 2016) in a vertical annulus subcooled flow boiling system showed that condensation and flashing were consistently underpredicted at low-pressure, low-flow conditions in the unheated section of the channel. The annulus facility, described in Section 2.2, consists of three instrumentation ports which span the heated length succeeded by two ports in the unheated length. Figure 1.1 (a) and (b) show the RELAP5 void fraction predictions with the experimental results as a function of non-dimensional distance in the test section for an elevated-pressure and low-pressure condition and (c) default model void fraction prediction vs. experimental data for all the conditions at the end of the test section.

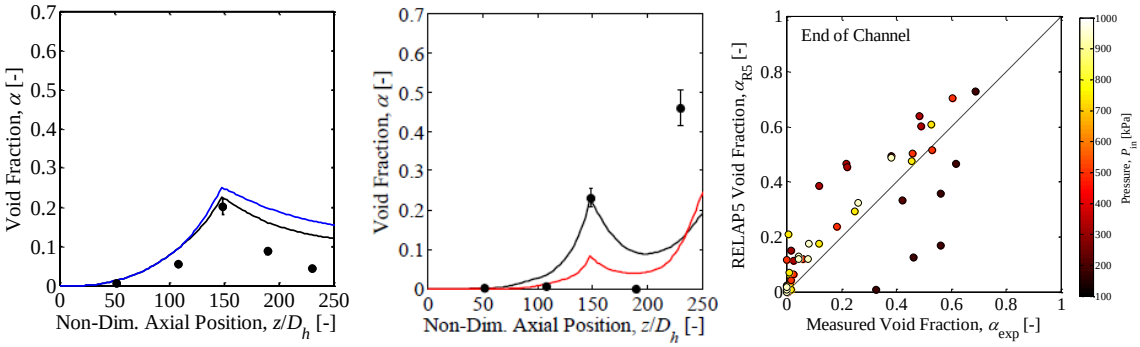

Figure 1.1 Comparison of experimental void fraction (black markers) with (a) default model (black), Option 45 (blue) for P_{in} = 947 kPa, $j_{f,in}$ = 1.0 m/s, $\Delta T_{sub,in}$ = 12°C, q_w''= 209 kW/m^2, (b) Default model (black) and original RELAP5 subcooled boiling model (red) for P_{in} = 183 kPa, $j_{f,in}$ = 0.24 m/s, $\Delta T_{sub,in}$ = 18°C, q_w''= 61 kW/m^2 and (c) Comparison for entire database at exit of the heated section based on system pressure using the default model (Fullmer et al., 2016).

In general, it is observed that the RELAP5 code predictions worsen at low pressures especially in the unheated section where it is driven by condensation. The common theme through each of these processes (boiling, condensation, flashing) is the requirement to correctly predict a relative temperature. The error in the prediction of saturation temperature and bulk liquid temperature alone may be small, but conditions driven by the difference between the two temperatures present a fundamental difficulty for system codes. The propagation of even small errors in temperature or pressure can result in significant phase-change errors when the two temperatures are similar. Historically, this error has not been an insurmountable issue as design basis accidents employ pump-driven, long-term cooling. However in low-pressure, low-flow conditions, void fraction dictates the flow condition, and error in the void fraction prediction will propagate more significantly to error in flow rate and hence, cooling capability, clouding the conservative approach. Significant improvement of the existing constitutive relations is required in order to meet these new challenges.

1.2. Theoretical Background

1.2.1. Two-fluid Model

The two-fluid model consists of conservation equations for mass, momentum and energy for each phase which are coupled through interfacial transfer terms. The two-fluid model can be applied to a wide variety of flow conditions which gives it increased flexibility over local instant formulation and mixture-based approaches. It takes into account the dynamic and non-equilibrium interactions between phases which make it a powerful tool to analyze two-phase flows. However, the transfer processes of each phase are specified by separate balance equations which increases the number of field equations as well as constitutive relations. The field equations are obtained by Eulerian time-averaging of the local instant formulation. The general balance equations for mass, momentum and enthalpy of the k^{th} phase are given as,

$$\frac{\partial\left(\alpha_k\rho_k\right)}{\partial t}+\nabla\cdot\left(\alpha_k\rho_k\hat{\boldsymbol{v}}_k\right)=\Gamma_k, \tag{1.1}$$

$$\frac{\partial\left(\alpha_k\rho_k\hat{\boldsymbol{v}}_k\right)}{\partial t}+\nabla\cdot\left(\alpha_k\rho_k\hat{\boldsymbol{v}}_k\hat{\boldsymbol{v}}_k\right)=\begin{cases}-\alpha_k\nabla p_k+\nabla\cdot\left[\alpha_k\left(\bar{\boldsymbol{\tau}}_k+\boldsymbol{\tau}_k^T\right)\right]+\alpha_k\rho_k\hat{\boldsymbol{g}}_k+\hat{\boldsymbol{v}}_{ki}\Gamma_k+\boldsymbol{M}_{ik}\\ -\nabla\alpha_k\cdot\boldsymbol{\tau}_{ki}+\left(p_{ki}-p_k\right)\nabla\alpha_k\end{cases}, \tag{1.2}$$

$$\frac{\partial\left(\alpha_k\rho_k\hat{h}_k\right)}{\partial t}+\nabla\cdot\left(\alpha_k\rho_k\hat{h}_k\hat{\mathbf{v}}_k\right)=\begin{cases}-\nabla\cdot\left[\alpha_k\left(\bar{\boldsymbol{q}}_k+\boldsymbol{q}_k^T\right)\right]+\alpha_k\dfrac{D_k}{Dt}p_k+\Gamma_k\hat{h}_{ki}\\ +a_i q_{ki}^{''}+\left(p_k-p_{ki}\right)\dfrac{D_k}{Dt}\alpha_k+\phi_k\end{cases}, \tag{1.3}$$

where $\alpha_k \rho_k$, $\hat{v}_k$, p_k, $\hat{g}_k$, $\hat{h}_k$, $\bar{\tau}_k$, τ_k^T, $\bar{q}_k$, q_k^T, are the void fraction, density, mass-weighted mean gas velocity, pressure, mass-weighted mean gravity, mass-weighted mean virtual enthalpy, mean viscous stress, turbulent stress, mean heat conduction flux, turbulent heat flux for the k^{th} phase; Γ_k, M_{ik}, v_{ki}, τ_{ki}, p_{ki}, h_{ki}, $q_{ki}^{''}$, and ϕ_k are the mass generation, generalized interfacial drag, interfacial velocity, interfacial shear stress, interfacial pressure, interfacial enthalpy, interfacial heat flux, and viscous dissipation for the k^{th} phase. The presence of the interfacial transfer terms makes the two-fluid model complex because of the constitutive modeling required (Ishii and Mishima, 1984; Ishii and Hibiki, 2011). In the context of the current research work, the mass generation term, Γ_k is the most important interfacial transfer term, defined as the product of the interfacial area concentration, a_i, and a driving flux, which is the mass generation rate per unit area given by,

$$\Gamma_k = -\, a_i \dot{m}_k, \tag{1.4}$$

where,

$$a_i \equiv \frac{1}{L_s} = \frac{1}{T}\sum_j \frac{1}{\left|v_i.n\right|_j}, \tag{1.5}$$

and $\dot{m}_k$ is the mass generation rate per unit area of the k^{th} phase, L_s is the length scale of the interface, v_i is the interface velocity, T is the averaging time, j denotes the j^{th} interface passing through a point in time T, and n is the normal vector. From Eq. (1.4), it can be determined that the degree of coupling between the two phases is determined by the interfacial area concentration. Furthermore, void fraction and interfacial area concentration are the two fundamental first-order geometrical parameters for two-phase flows and are closely related to two-phase flow regimes. The interfacial area concentration is typically determined by flow-regime-dependent static correlations in thermal hydraulic codes like TRACE and RELAP. However, the main drawback to using static correlations is that they do not fully reflect the true dynamic nature of the evolving two-phase flow structures. Additionally, the correlations require separate transition criteria which are validated using steady-state experiments for a certain operational range. Furthermore, the static correlations may cause numerical instabilities when applied to two-phase transients (Hibiki and Ishii, 2000b). Kocamustafaogullari and Ishii (1995) proposed the Interfacial Area Transport Equation (IATE) to

dynamically calculate the local, instantaneous interfacial area concentration to better represent the effects of changes in interfacial structure and flow regime transition. The Interfacial Area Transport Equation eliminates the discontinuities which arise when using transition criteria based static correlations. The IATE is discussed in detail in the following section.

Not long after the demonstration of the IATE in bubbly flows, the pursuit to capture higher void fraction regimes was met with the realization that modeling small spherical bubbles and large cap/slug bubbles are governed by different mechanisms, requiring separate treatment known as the two-group two-fluid model (Ishii and Kim, 2004). The two-group two-fluid model allows for separate description of the transport of group-1 bubbles (i.e. spherical and distorted bubbles) and group-2 (i.e. cap, slug, and churn-turbulent bubbles) requiring two gas-phase conservation equations and IATEs. Considering the practical difficulties in solving two gas-phase momentum equations, Sun et al. (2003) proposed the modified two-group two-fluid IATE model by combining the two gas-phase momentum equations into a simplified momentum equation based on an averaged group-1 and group-2 velocity and recommended a modified drift flux model to solve for the gas-phase velocity difference. The modified two-group two-fluid model conservation equations, assuming a single gas-phase pressure for both the bubble groups, are given by,

$$\frac{\partial\left(\alpha_{g1}\rho_g\right)}{\partial t}+\nabla\cdot\left(\alpha_{g1}\rho_g\boldsymbol{v}_{g1}\right)=\Gamma_{g1}-\Delta\dot{m}_{12}, \tag{1.6}$$

$$\frac{\partial\left(\alpha_{g2}\rho_g\right)}{\partial t}+\nabla\cdot\left(\alpha_{g2}\rho_g\boldsymbol{v}_{g2}\right)=\Gamma_{g2}+\Delta\dot{m}_{12}, \tag{1.7}$$

$$\frac{\partial\left(\alpha_g\rho_g\boldsymbol{v}_g\right)}{\partial t}+\nabla\cdot\left(\alpha_g\rho_g\boldsymbol{v}_g\boldsymbol{v}_g\right)=\begin{cases}-\nabla\cdot\left[\rho_g\dfrac{\alpha_{g1}\alpha_{g2}}{\alpha_g}\left(\boldsymbol{v}_{g1}-\boldsymbol{v}_{g2}\right)^2\right]-\alpha_g\nabla p_g\\+\alpha_g\nabla\cdot\left[\left(\boldsymbol{\tau}_g^{\mu}+\boldsymbol{\tau}_g^{T}\right)\right]+\alpha_g\rho_g g\\+\left[\Gamma_{g1}\boldsymbol{v}_{gi1}+\Gamma_{g2}\boldsymbol{v}_{gi2}+\Delta\dot{m}_{12}\left(\boldsymbol{v}_{g2}-\boldsymbol{v}_{g1}\right)\right]\\+\left(\boldsymbol{M}_{ig1}+\boldsymbol{M}_{ig2}\right)+\left(p_{gi}-p_g\right)\nabla\alpha_g\end{cases}, \tag{1.8}$$

$$\frac{\partial\left(\left(1-\alpha_g\right)\rho_f\boldsymbol{v}_f\right)}{\partial t}+\nabla\cdot\left(\left(1-\alpha_g\right)\rho_f\boldsymbol{v}_f\boldsymbol{v}_f\right)=\begin{cases}-\left(1-\alpha_g\right)\nabla p_f+\left(1-\alpha_g\right)\rho_f g\\+\left(1-\alpha_g\right)\nabla\cdot\left[\left(\boldsymbol{\tau}_f^{\mu}+\boldsymbol{\tau}_f^{T}\right)\right]+\boldsymbol{v}_{fi}\Gamma_f\\+\boldsymbol{M}_{if}+\left(p_{fi}-p_f\right)\nabla\left(1-\alpha_g\right)\end{cases}, \tag{1.9}$$

$$\frac{\partial\left(\alpha_g\rho_g h_g\right)}{\partial t}+\nabla\cdot\left(\alpha_g\rho_g h_g\boldsymbol{v}_g\right)=\begin{cases}-\nabla\cdot\left[\alpha_g\left(\boldsymbol{q}_g^{C}+\boldsymbol{q}_g^{T}\right)\right]+\alpha_g\dfrac{D_g p_g}{Dt}+\Gamma_g h_{gi}\\+a_i q_{gi}^{''}+\phi_g\end{cases}, \tag{1.10}$$

$$\frac{\partial\left(\left(1-\alpha_g\right)\rho_f h_f\right)}{\partial t}+\nabla\cdot\left(\left(1-\alpha_g\right)\rho_f h_f \boldsymbol{v}_f\right)=\begin{cases}-\nabla\cdot\left[\left(1-\alpha_g\right)\left(\boldsymbol{q}_f^C+\boldsymbol{q}_f^T\right)\right]+\Gamma_f h_{fi}\\ +\left(1-\alpha_g\right)\dfrac{D_f p_f}{Dt}+a_i q_{fi}^{''}+\phi_f\end{cases}, \quad (1.11)$$

where,

$$\alpha_{g1}+\alpha_{g2}=\alpha_g, \quad (1.12)$$

$$\Gamma_{g1}+\Gamma_{g2}=\Gamma_g, \quad (1.13)$$

$$\boldsymbol{v}_g=\frac{\alpha_{g1}\boldsymbol{v}_{g1}+\alpha_{g2}\boldsymbol{v}_{g2}}{\alpha_g}, \quad (1.14)$$

where $\Delta\dot{m}_{12}$ is the inter-group mass transfer rate from group-1 to group-2, $\boldsymbol{\tau}_k^C$, $\boldsymbol{\tau}_k^T$, $\boldsymbol{q}_k^C$, $\boldsymbol{q}_k^T$ are the void-weighted mean viscous stress, turbulent stress, mean heat conduction flux, and turbulent heat flux for the k^{th} phase and $q_{ki}^{''}$ is the interfacial area concentration weighted interfacial heat flux for the k^{th} phase. Additional closure relations for the modified two-group two-fluid IATE model are provided in Sun et al. (2003).

1.2.2. Interfacial Area Concentration Correlations

An exhaustive review of IAC correlations is provided in Ozar et al. (2012). Ozar et al. (2012) classifies the prediction methods of IAC into the following approaches: empirical correlations, semi-theoretical models, population balance approaches and simulations. The first two approaches form the basis of IAC correlations. Using simple geometrical considerations, Ishii and Mishima (1980) developed the following correlation for the bubbly flow regime,

$$\left\langle a_i\right\rangle=\frac{6\left\langle\alpha_g\right\rangle}{\left\langle D_{Sm}\right\rangle}=\frac{6\left\langle\alpha_g\right\rangle}{\left\langle D_v\right\rangle}\frac{\left\langle D_v\right\rangle}{\left\langle D_{Sm}\right\rangle}, \quad (1.15)$$

where D_{Sm} is the Sauter mean diameter and D_v is the bubble particle diameter. The ratio of the bubble particle diameter to the Sauter mean diameter is defined as the shape factor which is 1.0 for a spherical bubble and is a function of Eotvos number for distorted bubbles. Ishii and Mishima (1980) extended Eq. (1.15) for the slug/churn-turbulent flow regime in the following manner,

$$\langle a_i \rangle = \frac{4.5 C_{ct}}{D_h} \frac{\langle \alpha_g \rangle - \langle \alpha_{gs} \rangle}{1 - \langle \alpha_{gs} \rangle} + \frac{6 \langle \alpha_{gs} \rangle}{D_{Sm,1}} \frac{1 - \langle \alpha_g \rangle}{1 - \langle \alpha_{gs} \rangle}, \tag{1.16}$$

where α_{gs} is the bubbly-slug flow transitional void fraction and C_{ct} is a factor to represent the bubble interface roughness factor in churn-turbulent flow. The first term on the right-hand side is the contribution from the liquid slug assuming the slug bubble occupies 90% of the channel hydraulic diameter. The second term on the right-hand side is the contribution from small spherical/distorted bubbles in the liquid slug and in the liquid film surrounding the slug bubble. The IAC correlation used in RELAP5/MOD3.3 (2010) for bubbly and slug flow regimes is based on Eq. (1.16) where the bubbly-to-slug transition criterion is a function of the system mass flux. The IAC correlation is given as,

$$\langle a_i \rangle = \frac{4.5(2.0)}{D_h} \frac{\langle \alpha_g \rangle - \langle \alpha_{gs} \rangle}{1 - \langle \alpha_{gs} \rangle} + \frac{3.6 \langle \alpha_{gs} \rangle}{\langle D_b \rangle} \frac{1 - \langle \alpha_g \rangle}{1 - \langle \alpha_{gs} \rangle}, \tag{1.17}$$

where the value of the roughness factor, C_{ct}, is 2.0 and ‹D_b› is the average bubble diameter which is calculated using a Weber-number-based criterion. In TRACE V5.0 (2007), a simple Laplace length formulation is used to calculate IAC for the bubbly flow regime in the following manner,

$$\langle a_i \rangle = \frac{6 \langle \alpha_g \rangle}{\langle D_b \rangle}, \quad \langle D_b \rangle = 2 \sqrt{\frac{\sigma}{g(\rho_f - \rho_g)}}. \tag{1.18}$$

Similar to RELAP5, TRACE 5.0 employs a bubbly-slug transition criteria which is a function of the system mass flux. It must be mentioned that the IAC correlations listed in Table A.1 for RELAP and TRACE assume bubbly flow by employing the bubbly-slug transition criterion for the range of experimental void fraction and corresponding system mass fluxes used in the current benchmarking study. The IAC correlation proposed by Zeitoun et al. (1994) is an empirical model correlated to area-averaged void fraction, local subcooling, mass flux and thermophysical fluid properties using condensing steam-water data (summarized in Chapter 2) given by,

$$\langle a_i \rangle = 3.24 \left(\frac{\sigma}{g(\rho_f - \rho_g)} \right)^{-0.55} \langle \alpha_f \rangle^{0.757} \left(\frac{G}{\mu_f} \right)^{-1}, \tag{1.19}$$

where α_f is the liquid void fraction. The IAC correlation proposed by Dejesus and Kawaji (1990) is an empirical model correlated with the following area-averaged quantities: two-phase frictional

pressure drop, superficial liquid and gas velocities and liquid void fraction, using experimental data of air-CO_2 mixture and NaOH solution for flow conditions varying from bubbly to churn-turbulent flow, given by,

$$\langle a_i \rangle = 167.6 \langle j_g \rangle^{0.61} \langle j_f \rangle^{0.34}, \tag{1.20}$$

where j_g is the superficial gas velocity and j_f is the superficial liquid velocity. The main limitation of using empirically developed IAC correlations is the need for flow regime maps based on the flow configuration and the lack of applicability beyond the range of experimental data used to develop the correlation. IAC correlations developed using a semi-theoretical approach have similar limitations with respect to flow configuration, geometry, flow regime, etc. For a first-principles-based approach, the Interfacial Area Transport Equation is discussed in the following section.

1.2.3. Interfacial Area Transport Equation

The Interfacial Area Transport Equation (IATE) proposed by Ishii and colleagues (Kocamustafaogullari and Ishii, 1995; Ishii and Kim, 2004) is based on the Boltzmann transport equation by correlating the particle distribution function to the local interfacial area concentration. Yao and Morel (2004) derived the volumetric interfacial area balance equation by two methods: the number density equation and the Liouville equation with the resultant IATE formulation similar to that of Ishii and colleagues (Kocamustafaogullari and Ishii, 1995; Ishii and Kim, 2004) which is adopted in this study. A review of the various approaches used in deriving the IATE is given by Delhaye (2001). The sources and sinks of the IATE are broadly divided into two categories: change in bubble number density and change in bubble volume. Changes in bubble number density come from two mechanisms: interactions between bubbles, such as bubble break-up and coalescence, and phase change, such as wall nucleation and bubble collapse through condensation. Changes in bubble volume are due to changes in pressure due to compressibility and due to volume expansion without change in bubble number density such as evaporation and contraction due to condensation. Under adiabatic flow conditions, transport of interfacial area concentration is simplified to volume change due only to pressure and number density change due to interaction mechanisms. The three-dimensional interfacial area transport equation for bubbly flows, called the one-group IATE (Wu et al., 1998; Hibiki and Ishii, 2000a), is given as,

$$\frac{\partial a_i}{\partial t} + \nabla \cdot \left(a_i \mathbf{v}_i \right) = \frac{2}{3} \left(\frac{a_i}{\alpha_g} \right) \left\{ \frac{\partial \alpha_g}{\partial t} + \nabla \cdot \left(\alpha_g \mathbf{v}_g \right) - \eta_{ph} \right\} + \sum_j \phi_j + \phi_{ph}, \tag{1.21}$$

where ϕ_{ph} is the interfacial area source/sink term due to phase change, η_{ph} is the volume change associated with phase change and ϕ_j is the interfacial area source/sink term due to bubble interaction mechanisms. The term in brackets on the right-hand side of Eq. (1.21) represents the change in interfacial area concentration due to volume change at a fixed bubble number density while the other terms represent the change in interfacial area concentration due to change in number density. Since phase-change mechanisms are already incorporated for in ϕ_{ph}: η_{ph} is subtracted from the volume-change term to avoid double counting.

Considerable progress has been achieved in the mechanistic modeling of bubble interaction mechanisms largely due to both bubble coalescence from random collision of bubbles driven by turbulence and bubble breakup due to turbulent impact (Wu et al., 1998; Hibiki and Ishii, 2000a). The models proposed by Hibiki and Ishii (2000a) for the bubble-bubble and bubble-eddy collision frequencies used in the bubble random collision and bubble breakup mechanisms, respectively, are primarily based on the assumptions that the turbulence of the liquid phase is isotropic and that the bubble and eddy sizes lie in the inertial subrange. The bubble random collision ϕ_{RC} and turbulent impact ϕ_{TI} models based on Hibiki and Ishii (2000a) are given by,

$$\phi_{RC} = -\left(\frac{\alpha_g}{a_i}\right)^2 \frac{C_{RC}^{(1)}\alpha_g^2\varepsilon^{1/3}}{D_{Sm}^{11/3}\left(\alpha_{g,\max}-\alpha_g\right)} \exp\left(-C_{RC}^{(2)}\left(\frac{D_{Sm}^5\rho_f^3\varepsilon^2}{\sigma^3}\right)^{1/6}\right), \tag{1.22}$$

$$\phi_{TI} = \left(\frac{\alpha_g}{a_i}\right)^2 \frac{C_{TI}^{(1)}\left(1-\alpha_g\right)\varepsilon^{1/3}}{D_{Sm}^{11/3}\left(\alpha_{g,\max}-\alpha_g\right)} \exp\left(-C_{TI}^{(2)}\left(\frac{\sigma}{\rho_f D_{Sm}^{5/3}\varepsilon^{2/3}}\right)\right), \tag{1.23}$$

where ε is the turbulence energy dissipation rate obtained using the mechanical energy equation (Kocamustafaogullari et al.,1994; Hibiki and Ishii, 2000a) and σ is the surface tension. The model constants used in the equations are given in Table A.3 (Appendix A). Over the past couple decades, interaction mechanisms for bubbly flows have been developed for different geometries such as rectangular channels (Kim, 1999), round pipes (Wu et al., 1998; Hibiki and Ishii, 2000a), small diameter pipes (Hibiki et al., 2001), large diameter pipes (Schlegel et al., 2015) and annuli (Hibiki et al., 2003). However, interaction mechanisms have been shown to be negligible in flows with phase change (Park et al., 2007; Brooks et al., 2014; Ma et al., 2015; Brooks and Hibiki, 2016) which prompts more focus on improving IATE prediction in boiling and condensing flows.

A recent focus is applying the one-group IATE for subcooled boiling flows. In subcooled boiling, the phase-change mechanisms to be considered in the IATE are: wall nucleation, growth

of vapor bubbles due to bulk evaporation, shrinkage and collapse of vapor bubbles due to bulk condensation. The wall nucleation area source term, ϕ_{WN}, is typically described as the product of the nucleation site density (N_n), bubble departure frequency (f_d) and bubble departure diameter (D_d) (Hibiki and Ishii, 2003). The wall nucleation area source term can be expressed as,

$$\phi_{WN} = \frac{N_n f_d \xi_H}{A_c} \pi D_d^{\,2}, \tag{1.24}$$

where ξ_H and A_c are the heated perimeter and the cross-sectional area of the boiling channel, respectively. The active nucleation site density indicates the number of active sites of nucleating bubbles per unit surface area. The bubble departure diameter is defined as the mean diameter of the departing bubbles from all active sites from the heated surface, and the mean frequency of departing bubbles is described by the bubble departure frequency. Among the nucleation site density models available in the literature, the mechanistic correlation developed by Hibiki and Ishii (2003) was validated extensively with pool boiling and forced convection data with an average prediction accuracy of 28.5%. Brooks and Hibiki (2015) used an energy balance method along with a comprehensive database to provide correlations for the bubble departure frequency and bubble departure diameter accurate to within 34% and 22%, respectively. This is a marked improvement over older models which had errors on the order of 100% in the prediction of the experimental bubble departure frequency and bubble departure diameter (Brooks and Hibiki, 2015). Brooks and Hibiki (2015) found the wall nucleation area source term and volume source term in the IATE equation can be determined using the aforementioned models to within 65% and 90% accuracy, respectively, thereby highlighting the challenges in modeling wall nucleation. It is also important to note that the wall nucleation source term provides the boundary condition to calculate the volumetric vapor production, Γ_g, in the two-fluid model. Therefore, its accurate prediction is critical for good predictions using the two-fluid model. The volumetric vapor production term, Γ_g, consists of two terms: wall nucleation and evaporation. A review of the evaporation/wall nucleation heat flux models for subcooled boiling based on the wall heat flux partitioning method are given in Basu et al. (2005). Finally, the subcooled boiling volume source term from wall nucleation, η_{WN}, must be subtracted from the Γ_g term for reasons highlighted earlier. The η_{WN} term is much smaller in magnitude compared to the area source term and is often neglected (Ishii and Hibiki, 2011), but for completeness it is given as,

$$\eta_{\mathrm{WN}} = \frac{\pi}{6} D_d^3 \frac{N_n f_d \xi_H}{A_c}. \tag{1.25}$$

The IATE sink terms due to condensation are based on the model of Park et al. (2007), discussed in detail in the next chapter, wherein the condensation region is divided into two regimes: thermally controlled condensation and inertially controlled condensation. Therefore, the IATE area sink terms due to condensation are,

$$\phi_{CO} = -\pi \beta_{bc}^2 D_{Sm}^2 \frac{n_b}{t_c}, \tag{1.26}$$

$$\phi_{PC} = \frac{2}{3}\left(\frac{a_i}{\alpha_g}\right)\eta_{PC}. \tag{1.27}$$

The three-dimensional IATE formulation of Yao and Morel (2004), Kocamustafaogullari and Ishii (1995), and Ishii and Kim (2004) have been implemented by several researchers in Computational Fluid Dynamics (CFD) codes (Yao and Morel, 2004; Bae et al., 2010; Michta, 2011; Goodheart et al., 2013; Park et al., 2013; Alali, 2014; Shademan et al., 2014; Nguyen et al., 2015) coupling the IATE and the two-fluid model. While the combined uncertainties in the closure relationships of the two-fluid model and IATE can be considerable, most codes give reasonable overall qualitative predictions of the radial profiles of void fraction and interfacial area concentration. In order to decouple the two-fluid model from the IATE and isolate the effects of the condensation model of Park et al. (2007), Brooks et al. (2014), Ma et al. (2015) and Brooks and Hibiki (2016) used the experimental data of void fraction, liquid temperature, pressure and gas velocity to validate the (one-dimensional) area-averaged form of the IATE. Furthermore, this ensured that the volume change due to expansion term in the IATE was accurate to within experimental uncertainty thereby isolating the effect of the source and sink terms. In the study by Brooks and Hibiki (2016), the simulated interfacial area concentration was within 20% of the experimental data. However, Brooks and Hibiki (2016) found that condensation was overpredicted with the model of Park et al. (2007) and compensated by proposing the use of a lower subcooling temperature which was justified using the bubble-layer-averaged model (Hibiki et al., 2003).

The area-averaged IATE, which is the focus of the current study, can be obtained by cross-sectional averaging of the three-dimensional form of the IATE. The one-dimensional IATE can be given as (Hibiki and Ishii, 2000a),

$$\frac{\partial\langle a_i\rangle}{\partial t}+\frac{\partial}{\partial z}\left(\langle a_i\rangle\langle\langle v_{\mathrm{i}}\rangle\rangle_{a_i}\right)=\begin{cases}\dfrac{2}{3}\left(\dfrac{\langle a_i\rangle}{\langle\alpha_g\rangle}\right)\left\{\dfrac{\partial\langle\alpha_g\rangle}{\partial t}+\dfrac{\partial}{\partial z}\left(\langle\alpha_g\rangle\langle\langle v_g\rangle\rangle\right)-\langle\eta_{ph}\rangle\right\}\\ +\sum_j\langle\phi_j\rangle+\langle\phi_{ph}\rangle\end{cases}, \quad (1.28)$$

where ‹ › stands for area-averaged parameter, « »$_{ai}$ represents interfacial-area-concentration-weighted parameter and « » stands for void-weighted parameter. The interfacial-area-weighted gas velocity is assumed to be approximately equal to the void-weighted gas velocity (Hibiki and Ishii, 2000a; Brooks et al., 2012a),

$$\langle\langle v_{\mathrm{i}}\rangle\rangle_{a_i}\equiv\frac{\langle a_i v_i\rangle}{\langle a_i\rangle}\approx\frac{\langle\alpha_g v_g\rangle}{\langle\alpha_g\rangle}\equiv\langle\langle v_{\mathrm{g}}\rangle\rangle, \quad (1.29)$$

The area-averaged void fraction, ‹α_g›, can be determined by the void transport equation which is obtained by rearranging the gas continuity equation and is given as,

$$\frac{\partial\langle\alpha_g\rangle}{\partial t}+\frac{\partial}{\partial z}\left(\langle\alpha_g\rangle\langle\langle v_{\mathrm{g}}\rangle\rangle\right)=\left[\frac{\langle\Gamma_g\rangle}{\rho_g}-\frac{\langle\alpha_g\rangle}{\rho_g}\left(\frac{\partial\rho_g}{\partial t}+\frac{\partial}{\partial z}\left(\rho_g\langle\langle v_{\mathrm{g}}\rangle\rangle\right)\right)\right]. \quad (1.30)$$

If the void fraction is known, then the IATE and void transport equations can be decoupled, and the void dependence on the right-hand side of Eq. (1.28) can be satisfied by interpolating between void fraction measurements, henceforth referred to as the decoupled model. In the decoupled model, the volume change term in the IATE is not sensitive to other parameters in the Γ_g model since the void fraction is supplied. Although the interaction mechanisms of Hibiki and Ishii (2000a) were derived for adiabatic flows, it is consistent with vapor-water phase-change flows (Brooks and Hibiki, 2016). It must be noted that the exact form of the area-averaged IATE source and sink terms involve many covariances, but the functional form of the area-averaged IATE would be the same if the hydraulic diameter were taken as the length scale over which the equations were averaged (Wu et al., 1998). This assumption holds true for a relatively uniform void distribution with no heat addition and can be extended to condensing flows with the assumption of uniform subcooling. By algebraic manipulation of Eqns. (1.28) and (1.30) and dropping the time derivative term for steady state, the general source and sink terms contributing to change in interfacial area concentration, Δ‹a_i›, are given by,

$$\Delta\langle a_i \rangle = \frac{\Delta z}{\langle\langle v_g \rangle\rangle}\left\{\langle \phi_{Ex} \rangle + \langle \phi_{DP} \rangle + \sum_j \langle \phi_j \rangle + \langle \phi_{ph} \rangle + \langle \phi_{Conv} \rangle\right\}, \tag{1.31}$$

where ϕ_{Ex} is the source term due to expansion, ϕ_{ph} is the source/sink term due to phase change, ϕ_{DP} is the source/sink term due to pressure change, ϕ_j is source/sink term due to the j^{th} bubble interaction mechanism and ϕ_{Conv} is the source/sink term due to convection.

The two-group two-fluid model (introduced in Section 1.2.1) accounts for the differences in the transport of group-1 bubbles and group-2 bubbles separately, necessitating a separate IATE for each bubble group. Some of the foundational works which established the theoretical framework of the two-group two-fluid model are: Ishii et al. (1998), Wu et al. (1998), Hibiki and Ishii (2000b), Fu and Ishii (2003a), Sun et al. (2003), Sun et al. (2004a) and Ishii and Kim (2004). This expansion in bubble groups also adds an additional set of conservation equations for the gas phase, and, therefore, correct tracking and partitioning of the gas phase into the bubble groups are critical. The responsibility of this bookkeeping is assigned to an inter-group mass transfer term and is required in the gas-phase conservation equations and IATEs. In the case of the two-group IATE, the inter-group transfer is an additional term accounting for the change in bubble group identity. Since the bubble group is based on bubble size with the boundary taken to be the maximum distorted bubble size, a bubble can change its group affiliation through interaction mechanisms, phase-change mechanisms and pressure change. The two-group IATE model (Ishii and Kim, 2004) is given as,

$$\frac{\partial a_{i,1}}{\partial t} + \nabla\cdot\left(a_{i,1}\mathbf{v}_{i1}\right) = \begin{cases} \left\{\frac{2}{3} - \chi\left(\frac{D_c}{D_{Sm,1}}\right)^2\right\}\left(\frac{a_{i,1}}{\alpha_{g1}}\right)\left\{\frac{\Gamma_{g1} - \eta_{ph,1}\rho_g - \Delta\dot{m}_{12}}{\rho_g} - \frac{\alpha_{g1}}{\rho_g}\frac{D\rho_g}{Dt}\right\}, \\ +\sum_j \phi_{j,1} + \phi_{ph,1} \end{cases} \tag{1.32}$$

$$\frac{\partial a_{i,2}}{\partial t} + \nabla\cdot\left(a_{i,2}\mathbf{v}_{i2}\right) = \begin{cases} \kappa\left(\frac{a_{i,2}}{\alpha_{g2}}\right)\left\{\frac{\Gamma_{g2} - \eta_{ph,2}\rho_g + \Delta\dot{m}_{12}}{\rho_g} - \frac{\alpha_{g2}}{\rho_g}\frac{D\rho_g}{Dt}\right\} + \\ \chi\left(\frac{D_c}{D_{sm,1}}\right)^2\left(\frac{a_{i,1}}{\alpha_{g1}}\right)\left\{\frac{\Gamma_{g1} - \eta_{ph,1}\rho_g - \Delta\dot{m}_{12}}{\rho_g} - \frac{\alpha_{g1}}{\rho_g}\frac{D\rho_g}{Dt}\right\} + \sum_j \phi_{j,2} \end{cases}, \tag{1.33}$$

$$\Delta\dot{m}_{12} = \rho_g\left\{\sum_j \eta_{j,12} + \chi\left(\frac{D_c}{D_{Sm,1}}\right)^3\left\{\frac{\partial\alpha_{g1}}{\partial t} + \nabla\cdot\left(\alpha_{g1}\mathbf{v}_{g1}\right) - \eta_{ph,1}\right\}\right\}, \tag{1.34}$$

where $\Delta\dot{m}_{12}$ is the inter-group mass transfer rate from group-1 to group-2 per unit mixture volume, χ is the inter-group mass transfer coefficient, κ is the group-2 shape coefficient (Ozar, 2009), $\eta_{j,12}$ is the net volume transfer rate from group-1 bubbles to group-2 bubbles due to the j^{th} interaction between the two bubble groups and D_c is the critical bubble diameter (Ishii and Zuber, 1979).

Substantial effort has gone toward formulating and benchmarking the interaction mechanisms for the two-group IATE model. Ishii et al. (1998) proposed five categories of interaction mechanisms for the two-group IATE model: coalescence due to random collisions driven by turbulence, coalescence due to wake entrainment, breakup due to the impact of turbulent eddies, shearing off small bubbles from cap bubbles, and the breakup of large cap bubbles due to flow instability on the bubble surface. Hibiki and Ishii (2000b) focused on bubbly-to-slug transition and categorized the two-group interaction mechanisms into four groups similar to Ishii et al. (1998) but neglected breakup of small bubbles from cap bubbles and the coalescence of small bubbles into cap bubbles as the bubble count in the transition regime was expected to be low in the experimental conditions studied. Hibiki and Ishii (2000b) proposed the following new two-group interaction mechanisms: coalescence of two cap bubbles due to wake entrainment, coalescence of a spherical/distorted bubble and a cap bubble due to wake entrainment, breakup of a cap bubble into two cap bubbles due to turbulent impact, and breakup of a cap bubble into a cap bubble and a small bubble due to turbulent impact. Hibiki and Ishii (2000b) benchmarked the area-averaged two-group IATE model with upward adiabatic air-water pipe data and obtained excellent predictions for the interfacial area concentration of the bubbly-slug transition with an average relative deviation of 3.61%, neglecting inter-group mass transfer due to bubble expansion. Fu and Ishii (2003a) derived mechanistic two-group interaction mechanisms covering bubbly, slug and churn flow regimes assuming representative cap and slug bubble shapes. Fu and Ishii (2003a) classified the modeling of the bubble interaction mechanisms for slug/cap bubbles into four major categories: coalescence due to acceleration of trailing group-2 bubbles in the wake region of a leading group-2 bubble, coalescence of group-1 bubbles in liquid slug to group-2 bubble due to random collision in the wake region driven by high turbulent intensity or by wake entrainment through recirculating vortex structures, shearing off of small bubbles at the skirt of group-2 bubble and break-up of group-2 bubbles due to turbulent disintegration. Fu and Ishii (2003b) benchmarked the area-averaged two-group IATE model of Fu and Ishii (2003a) using four-sensor conductivity probe data taken for upward air-water pipe flow, neglecting inter-group mass transfer due to bubble expansion. Fu and Ishii (2003b) determined closure coefficients for the newly proposed group-2 interaction mechanisms using the same dataset and obtained satisfactory results with ~15% error for bubbly-slug flow and slug flow conditions and ~11% error for churn-turbulent flow conditions. Sun et al.

(2004a) proposed mechanistic two-group bubble interaction mechanisms using a systematic integral approach for confined gas-liquid two-phase flow across different flow regimes by considering all the five major categories of interaction mechanisms proposed by Ishii et. al (1998). Sun et al. (2004b) benchmarked the area-averaged two-group IATE proposed by Sun et al. (2004a) using eleven datasets taken in an upward adiabatic bubbly flow conditions and 13 datasets taken in cap-turbulent and churn-turbulent flows and obtained good predictions of the interfacial area concentration with a maximum error of ~7%. Sun et al. (2004b) also formulated a correlation for the inter-group mass transfer coefficient using the data, which is discussed in a later section. Sun et al. (2004a, 2004b) are the only works to consider the two-group IATE model by including the full inter-group mass transfer term in their benchmark. Schlegel et al. (2015, 2017) performed an optimization of the coefficients in the two-group interaction mechanisms with an upward air-water dataset taken in large diameter pipes (0.152-0.304 m diameter) using the full one-dimensional two-group IATE model assuming a value of unity for the inter-group mass transfer coefficient. Schlegel et. al (2015, 2017) obtained satisfactory results in comparison to the data with a root-mean-squared error of 34.9%, although the coefficients obtained through this approach, particularly the inter-group mass transfer coefficient, have little physical justification.

While the work on interaction mechanisms in air-water flow has been substantial, few efforts have focused on the two-group two-fluid IATE model in phase-change flows. Ozar (2009) performed the first comprehensive experimental and modeling study looking at the application of the two-group IATE model in subcooled boiling flows. Ozar (2009) reviewed and formulated constitutive models used in the two-group IATE model for evaporation, wall nucleation, flashing and bulk condensation. Brooks et al. (2014) performed the first and only validation of the two-group IATE model with phase change (decoupled from the two-fluid model) for subcooled boiling flows with the data of Ozar et. al (2013) by incorporating bubble-layer averaging (Hibiki et. al, 2003) for the group-1 IATE and area-averaging for the group-2 IATE. Brooks et al. (2014) found that the contribution of interaction mechanisms is negligible in subcooled boiling flows with expansion with wall nucleation and bulk condensation being the dominant IATE mechanisms for group-1 bubbles and inter-group expansion being the dominant source for group-2 bubbles. While considerable attention has been placed on understanding subcooled and saturated boiling flows, their complex thermo-fluid dynamics can make it difficult to isolate phenomena such as wall nucleation, evaporation heat/mass transfer, condensation heat/mass transfer, pressure expansion/contraction, interfacial momentum transfer, bubble interaction mechanisms, etc. The focus of this work is to look at adiabatic phase-change flows through a combination of experimental and analytical approaches focusing on gas-dispersed condensing flows.

1.3. Required Improvements

There are three major improvements which have been identified in the application of IATE in phase-change flows. They are the following,

1. In all existing two-group IATE phase-change studies performed to date, the flow field has resulted in expansion of group-1 bubbles to group-2 bubbles through pressure or phase change. However, two-phase flows with inter-group transfer from group-2 to group-1 (through condensation or bubble contraction) has not been attempted, given in Eq. (1.34). Therefore, the current inter-group mass transfer model does not conserve mass for all flow conditions which presents a serious limitation.

2. The stated goal of decoupling the IATE from the two-fluid model in past condensing flow IATE studies is to isolate the IATE condensation sink terms as well as to provide a simple model to be easily adopted into a current two-fluid model solver. However, since the closure of the IATE requires modeling inherent to the closure of the gas-phase continuity equation, a coupled simulation of IATE and void fraction transport is yet to be performed. Therefore, the condensation phase-change terms in the IATE have not been systematically reviewed and benchmarked.

3. In general, more experimental conditions are required for validation of the IATE for condensing flows spanning a wide range of flow conditions. Out of the two condensing flow databases available in the public domain, the data of Zeitoun (1994) spans moderate mass fluxes and a wide range of subcooling around atmospheric system pressures. Although the database of Ozar et al. (2013) spans a wide range of systems pressures, only four suitable conditions exist for the present study. In conclusion, there is a need for a comprehensive database for condensing flows spanning a wide range of system conditions.

1.4. Objectives

The main contribution of this work is to evaluate the current state of two-fluid model capabilities in condensing flows, and, to achieve this goal, the following objectives have been met,

1. To address the lack of high-quality condensing flow data for code benchmarking, design and construct an annulus experimental test facility scaled on a BWR subchannel and perform experiments to acquire an extensive adiabatic steam-water flow database which includes condensing flow data.

2. Investigate and improve condensing bubbly flows by analyzing the condensation model of Park et al. (2007) for the one-group area-averaged IATE and validating it using the newly acquired data (Kumar et al., 2019) as well as available experimental data for condensing flows (Zeitoun, 1994; Ozar et al., 2013) covering a wide range of subcooling, pressure and flow rates. Furthermore, investigate the sensitivity of important parameters which impact the condensation model.

3. Review and analyze the current formulation of the two-group two-fluid IATE model and validate the model against the newly aquired dataset and evaluate its limitations.

4. Expand the current inter-group mass transfer term to incorporate inter-group mass transfer from group-2 to group-1, which is critical for condensing flows.

5. Provide closure relations for the newly proposed group-2 inter-group mass transfer coefficient and evaluate and propose modifications to the group-2 Nusselt number correlation.

6. Validate the proposed two-group two-fluid one-dimensional IATE formulation for condensing flows with the newly acquired data.

1.5. Outline of the Document

The existing condensation models and experimental data with two-phase measurements for condensing flows are comprehensively summarized in Chapter 2 and serve as the starting point for the research work. The need for more condensing flow data is addressed in Chapter 3 by the design and construction of an experimental facility. Description of the facility including instrumentation is summarized. A detailed discussion on the local data for three representative cases from the new dataset as well as a parametric study of area-averaged data is presented. In Chapter 4, the existing one-group IATE model is thoroughly reviewed with the new and available datasets and

modifications are proposed. A coupled void-transport-equation-IATE validation is conducted for the modified model apart from a sensitivity analysis. After a thorough benchmarking of the IATE condensing flow model for bubbly flows, the logical extension of the work using the two-group IATE model to capture cap/slug bubbly flow regimes is covered in Chapter 5. The current two-group IATE formulation is reviewed, and the inter-group mass transfer model is extended for condensing flows and validated with the newly acquired dataset. Finally, the research work is summarized and major contributions from the work are listed in Chapter 6, including proposed future work.

CHAPTER 2. EXISTING WORK

This chapter describes the existing work done on condensation in gas-dispersed flows focusing on both experimental datasets and modeling approaches. The first half of this chapter is a review of various approaches for condensation phase-change modeling: analytical, empirical and a combination of first-principles modeling and empiricism. The condensation model proposed by Park et al. (2007) is also discussed in the context of IATE. The second half of the chapter covers the existing experimental data available for validation of condensation phase-change models and highlights the need for more two-group condensing flow conditions.

2.1. Condensation Phase-change Modeling

In the context of reactor safety, Hsu (1981) recognized the following four scenarios where condensation plays a key role: condensation of vapor bubbles in the liquid during Emergency Core Cooling (ECC), condensation of vapor jets in the liquid in the containment, condensation of vapor on subcooled droplets in the ECC spray and condensation between two streams in the downcomer. The current study is focused on the first case, i.e. condensation of vapor bubbles (or gas-dispersed) in the subcooled liquid. Rayleigh (1917) was the first to theoretically model the dynamics of the collapse of a spherical cavity. Rayleigh (1917) assumed an idealized infinite liquid and analyzed the condensation process by considering a momentum transfer between the collapsing interface and the surrounding liquid, often described as Rayleigh's equation. Zwick and Plesset (1955) incorporated temperature effects into their analysis of a collapsing spherical vapor bubble in a stagnant uniform subcooled liquid by postulating that a decreasing vapor pressure at the interface of the bubble will slow down the collapsing process. Zwick and Plesset (1955) analytically solved the radial momentum equation with a temperature-dependent vapor pressure, derived using an energy balance at the liquid-vapor interface, with a thin thermal-boundary-layer approximation and found that the solution only marginally differed from Rayleigh (1917). Zuber (1961) studied the dynamics of the growth and collapse of a spherical vapor bubble in subcooled pool boiling and obtained good agreement with available experimental subcooled boiling data. Zuber (1961) found that while the experimental bubble growth time could be well predicted using a heat-transfer model based on an energy balance at the liquid-vapor interface and the transient heat conduction equation, the experimental bubble collapse time was better approximated by an inertial model (albeit with large scatter) resulting in similar bubble growth and collapse rates. Zuber (1961) reasoned that the bubble collapse process approximates an isothermal process in the limit of large thermal gradients because the heat released at the vapor-liquid interface is quickly transported via convection in the

liquid phase thereby preventing the growth of the thermal boundary layer. However, the subcooled boiling data analyzed by Zuber (1961) was taken at large subcooling ($\Delta T_{sub} > 30^{o}C$), and it is expected that thermal effects would control the bubble condensation rate at moderate to low subcooling. Florschuetz and Chao (1965) investigated the mechanics of a vapor bubble collapse in subcooled liquid, both analytically and experimentally in water and ethyl alcohol under free fall (sub-atmospheric) and atmospheric pressures. Florschuetz and Chao (1965) defined a dimensionless parameter, B_{eff}, which was a function of the Jacob number and liquid inertia, and determined that a thermally controlled collapse occurred at lower values of B_{eff} while an inertial collapse is likely at higher values of B_{eff} and a third category where both effects are of comparable importance. Florschuetz and Chao (1965) also stated that the translational bubble velocity, which is not considered in their theoretical analysis, enhances the heat transfer rates at the bubble interface. The relative motion between the bubble and the liquid, which is ignored in most of the earlier theoretical works, affects the condensation rate in the following ways: convection affects the heat transfer rate from and to the bubble surface, the nonuniform pressure field due to bubble motion can deform the bubble shape and, finally, the effect of added mass influences the heat transfer rate and bubble shape (Prosperetti, 2017). Abdelmessih et al. (1972) used high-speed photography to examine the effect of fluid velocity on the growth and collapse rates of vapor bubbles in subcooled flow boiling. Abdelmessih et al. (1972) showed that the maximum bubble radius and bubble span decrease for a given wall heat flux as the liquid velocity increases and proposed that liquid turbulence enhances the heat transfer rate at the bubble wall, triggering a faster collapse giving a more symmetrical bubble growth and collapse curve. Abdelmessih et al. (1972) concluded that bubble collapse is controlled by heat transfer at low liquid velocities and subcooling while turbulence and inertia control the rate of bubble collapse at higher velocities. Prosperetti (2017) stated that the difficulties in achieving precise control in condensation experiments is the reason for the focus shifting toward developing empirical correlations.

Ruckenstein (1959) studied the heat transfer between the superheated liquid and a moving vapor bubble using potential theory to obtain the velocity field around a solid sphere and the energy equation to solve for the temperature field. Ruckenstein (1959) proposed a Nusselt number correlation for the evaporation of a single vapor bubble as a function of the bubble Péclet number and stated that multi-bubble effects would require a modification of the correlation. Isenberg and Sideman (1970) investigated condensation of bubbles of volatile organic liquids in water and aqueous glycerol solutions both theoretically and experimentally at low Jacob numbers (ΔT_{sub}~3-6^{o}C). Isenberg and Sideman (1970) derived a condensation Nusselt number correlation using laminar flow theory combined with the energy equation and obtained good agreement with

experimental bubble collapse curves in water. Akiyama (1973) conducted subcooled pool boiling experiments to study the condensation of a moving vapor bubble in water and two organic liquids at atmospheric pressure for a range of subcooling, ΔT_{sub} (ΔT_{sub} ~ 2-50^{o}C). Akiyama (1973) used laminar heat transfer theory, like Isenberg and Sideman (1970), to derive a correlation for the collapsing bubble diameter using the Nusselt-number correlation proposed by Grober et al. (1955) but did not obtain a good agreement (~50-100%) with the experimental bubble collapse curves. Chen and Mayinger (1992) studied heat transfer at the interface of vapor bubbles condensing in different subcooled liquids (ethanol, propanol, R113 and water) using holographic interferometry and high-speed cinematography for a range of Jakob numbers, *Ja* (1< *Ja* <120). Chen and Mayinger (1992) proposed a condensation Nusselt-number correlation valid up to Reynolds numbers (based on the detachment diameter) of 10^4 and set heat transfer and inertially controlled condensation regimes to occur for Jacob numbers approximately below 60 and above approximately 100, respectively. The correlation of Chen and Mayinger (1992) is used in the TRACM/F90 (TRACE) code (Spore et al., 2000) in bubbly and slug flow regimes for bubble Reynolds numbers, Re_b, between 400 and 10^4. Zeitoun (1994) conducted experiments (described in Section 2.2) to study heat transfer due to condensation of vapor bubbles in subcooled flow boiling of water and is one of the few studies which looked at multi-bubble effects in a flow system. Zeitoun (1994) used the experimental data to correlate the condensation Nusselt number for steam-water flows as a function of the bubble Reynolds number (based on the Sauter mean bubble diameter, D_{Sm}), Jacob number and gas void fraction. Zeitoun (1994) stated that the void fraction dependence in the Nusselt number correlation is due to the fluid mixing caused by higher vapor concentration but did not provide an adequate justification for the inverse Jacob number dependence. Kosky (1968) studied the growth of slug vapor bubble in superheated water using high-speed visualization and extended Zwick and Plesset's (1955) asymptotic solution to obtain an analytical expression for the slug bubble length. Kosky (1968) found that the slug bubble length, obtained by assuming evaporation through a thin liquid film, matches the experimental data with marginal contribution to heat transfer from the hemispherical ends of the slug bubble. Garimella et al. (2016) modeled the condensation process of a slug bubble in microchannels by summing the heat transfer contributions from the liquid slug portion and the Tylor bubble portion. Garimella et al. (2016) used the hydraulic diameter as heat transfer length scale to model the liquid slug portion based on well-known single-phase Nusselt number correlations and derived an analytical expression for condensation heat transfer coefficient of the Taylor bubble based on the liquid film thickness as the heat transfer length scale. Garimella et al. (2016) benchmarked the proposed heat transfer model with experimental refrigerant heat transfer coefficients with a prediction accuracy of ±25% for 94% of the data. Both these studies

highlight the importance of the heat transfer length scale in the modeling of slug bubbles. Finally, the Nusselt number correlations used in this study are summarized in Table A.2 (Appendix A).

Park et al. (2007) proposed a new model for the condensation sink terms in the one-group area-averaged IATE model in condensing flows. In the condensation model proposed by Park et al. (2007), two different condensation regimes are considered: heat transfer and inertially controlled condensation. Thermally controlled condensation leads to a reduction in bubble size at constant bubble number density whereas inertially controlled condensation decreases the bubble number density. A schematic of the bubble growth and collapse process in subcooled boiling is shown in Figure 2.1 as a function of the nondimensional bubble diameter, β_b, versus nondimensional time, t^* (based on Zuber, 1961; Abdelmessih et al., 1972).

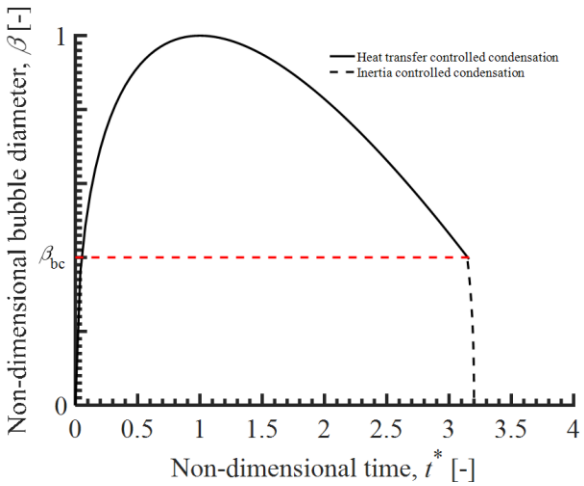

Figure 2.1 Schematic diagram showing the variation of the nondimensional bubble diameter during the bubble growth and collapse process in subcooled boiling.

The peak of the curve corresponds to the Sauter mean diameter, D_{Sm}, which is the maximum local bubble diameter and corresponds to the initial bubble diameter for the condensation process. As the bubble diameter decreases below the Sauter mean diameter, the condensation process is initially controlled by the heat transfer between the saturated gas bubbles and subcooled liquid and is inherently a slow process with a timescale, t_c, governed by an energy balance at the interface of a collapsing bubble, given as,

$$t_c = \frac{D_{Sm}^2 - D_{bc}^2}{4} \frac{\rho_g h_{fg}}{Nu_c k_f \Delta T_{sub}} = \frac{D_{Sm}^2 \left(1 - \beta_{bc}^2\right)}{4} \frac{1}{Nu_c \cdot Ja \cdot \alpha_t}, \tag{2.1}$$

where h_{fg} is the latent heat of vaporization, k_f is thermal conductivity, Nu_c is the condensation Nusselt number correlation, ΔT_{sub} is the liquid subcooling, Ja is the Jacob number, and α_t is the thermal diffusivity. On the other hand, the second stage of the condensation process is a fast process controlled by the balance between pressure and inertial forces, termed inertially controlled condensation. The bubble diameter in the second stage rapidly collapses from a boundary diameter, D_{bc}. The bubble collapse time in the inertially controlled condensation regime is given by the analysis of Rayleigh (1917) and is expressed as a function of the dimensionless boundary diameter, β_{bc} ($\beta_{bc} = D_{bc}/D_{Sm}$), as,

$$t^* = \frac{t}{D_{Sm}\sqrt{\left(\frac{3\rho_f}{8P}\right)}} = \int_{\beta_{bc}}^{1} \frac{\beta^{3/2}}{\left(1-\beta^3\right)} d\beta = f\left(\beta_{bc}\right), \tag{2.2}$$

where t^* is the nondimensional time, D_{Sm} is the Sauter mean diameter of the bubble at the start of condensation, P is the system pressure and ρ_f is the liquid density. A probability function, p_c, based on the bubble collapse time given in Eq. (2.2), denotes the probability that the bubble is in the inertia-controlled condensation region, given as,

$$p_c = \frac{\Delta t_{c,in}}{\Delta t_{c,th} + \Delta t_{c,in}} = \frac{f(0) - f\left(\beta_{bc}\right)}{f(0)}. \tag{2.3}$$

For the closure of the two-fluid model, the interfacial mass transfer rate, Γ_g, represents the rate of mass transfer between the gas and liquid phases due to phase change. The procedure followed by Park et al. (2007) to obtain the total mass transfer rate, Γ_g, from both the condensation processes is as follows. The bubble residence time, t_c, given by Eq. (2.1), is taken as the total residence time of the collapsing bubble since it is much greater than the inertially controlled residence time, given by Eq. (2.2). It must be noted that inertially controlled condensation results in volume transfer from the gas phase due to a decrease in the number density of bubbles, n_b, while thermally controlled condensation results in volume transfer due to changing bubble size at a fixed number density. Therefore, the rate of volume transfer per unit volume from the gas phase due to inertially controlled condensation, η_{CO}, and thermally controlled condensation, η_{PC}, are given as,

$$\eta_{CO} = -\frac{\pi D_{bc}^3}{6}\frac{n_b}{t_c}, \tag{2.4}$$

$$\eta_{PC} = (1 - p_c) \cdot n_b \cdot \frac{dV_b}{dt} = -\pi (1 - p_c) D_{Sm} \cdot n_b \cdot Nu_c \cdot Ja \cdot \alpha_t, \tag{2.5}$$

where V_b is the bubble volume. Finally, the total mass transfer rate is obtained by summation of the mass transfer rates from both the condensation mechanisms as,

$$\Gamma_g = \rho_g \eta_{CO} + \rho_g \eta_{PC}. \tag{2.6}$$

Park et al. (2007) also derived the corresponding condensation area sink terms, important from the perspective of the IATE which was discussed in Section 1.2.2. Finally, Park et al. (2007) recommended the Nusselt number correlation of Zeitoun (1994) in the condensation model.

2.2. Existing Experimental Work

A comprehensive list of forced-convection two-phase flow experimental studies that provide local void fraction and interfacial area concentration/bubble size measurements has been compiled by Lin and Hibiki (2014). Extensive research efforts have gone towards characterizing adiabatic air-water (or nitrogen-water) flows for various flow geometries which include different channel sizes, flow regimes and flow orientation, mostly near atmospheric pressure and room temperature conditions. However, the number of available experimental datasets that focus on phase-change flows are few in number (Lin and Hibiki, 2014). Although air-water data can be used toward understanding the hydrodynamics of phase interaction, modeling of thermal-fluid dynamics of phase-change flows requires a wide range of experimental datasets. These experiments range from studying separate effects like wall nucleation in subcooled boiling flows (Brooks et al., 2015; Ooi et al., 2018) to transport phenomena like boiling, condensation and flashing (Ozar et al., 2013). Some of the commonly used experimental techniques for measurement of local and/or area-averaged/chordal-averaged two-phase flow parameters are multi-sensor conductivity probes, multi-sensor optical fiber probes, wire-mesh sensors, gamma transmission and x-ray tomography, and high-speed video imaging. All of these measurement techniques have certain drawbacks, but the main advantage with multi-sensor conductivity probes is that they provide local time-averaged flow measurements of void fraction, gas velocity and interfacial area concentration in flow regimes spanning from bubbly up to churn-turbulent flows. A list of all the studies available with interfacial area concentration data in adiabatic two-phase flows has been compiled by Lin and Hibiki (2014) from which two studies with condensing flow data were used in the current analysis (Zeitoun, 1994; Ozar et al., 2013). The condensing data of Ma et al. (2015) is not used in the current study because

it was determined that insufficient data is available in the public domain to perform a validation study. It is important to note that only the experimental data of Ozar et al. (2013) was taken at high pressure (up to ~950 kPa) while the other two datasets (Zeitoun, 1994; Ma et al., 2015) were taken near atmospheric pressure.

The test facility of Ozar et al. (2013) is scaled based on a boiling water reactor subassembly and consists of two subsections: the primary loop and the pressurizing system. Water was held in a stainless-steel degassing tank with an internal volume of approximately 0.096 m^3 in the primary loop. The tank connects to a centrifugal pump through the return line. A globe valve was used on the inlet piping to control the flow rate along with the pump controller. A magnetic flowmeter, located downstream of the globe valve, was used for the flow rate measurements. The inlet subcooling was set using a preheater with a maximum power of 18 kW located downstream of the flow meter. The flow was divided into four separate lines using a header before it entered the test section. Finally, at the exit of the test section, the flow went through a shell-and-tube-type heat exchanger where the steam condensed. The pressurizing system consisted of high-pressure nitrogen tanks, a regulator and an accumulator tank which maintained a constant system pressure. The test section is a vertical annulus with an internal diameter of 19.1 mm and an external diameter of 38.1 mm (hydraulic diameter, D_h, of 19 mm). The total test section length is 4.477 m and consists of 2.845 m of heated length followed by 1.632 m of unheated length. The piping was well insulated throughout the length, and small guide pins were used downstream of each of the measurement ports to ensure proper alignment of the inner rod. The heat loss from the test section and pressure loss from the guide pins were found to be small (Ozar, 2009). Like the previous facility, this setup was used to study subcooled flow boiling in the heated section and condensation in the unheated region. Out of a total of five measurement ports, three ports covered the unheated section: ports 3, 4 and 5 at nondimensional distances, z/D_h, of 148.8, 189.3 and 229.9, respectively. The three instrumentation ports in the unheated section were used to measure the void fraction, interfacial area concentration, and gas velocity for each bubble group with four-sensor conductivity probes. The other relevant measurements for the condensation study included the system pressure and liquid subcooling temperatures along the unheated section, and flow rate measured with a magnetic flowmeter upstream of the test section. Four conditions were chosen for the current study out of a total of fifty-seven conditions from ports 3-5 so that the test matrix is restricted to condensing flows. The four conditions span the following parameters: pressure (504-947 kPa), inlet liquid subcooling (1.1-1.55 °C) and mass flux (927-948 kg/m^2-s).

Adiabatic steam water datasets (Zeitoun et al., 1994; Manera et al., 2006) are important in isolating condensation and pressure-driven phase-change (i.e. flashing) phenomena. Manera et al.

(2006) conducted stationary flashing flow steam-water experiments at atmospheric pressure. The experimental facility consists of a 1.95 m heated section with four parallel heated channels of diameter 20.4 mm (rod diameter of 12.5 mm, maximum power of 3 kW/rod) and four bypass channels (closed for the experiments described here) and a 3-m-long adiabatic section of diameter 47 mm. Two-phase characteristics are measured in the adiabatic section using needle probes located at six axial locations along the central axis of the riser section as well as two wire-mesh sensors (sampled at 1200 Hz) in the upper part of the adiabatic section, separated by an axial distance of 27.5 mm. Other instrumentation used in the facility consists of electromagnetic flow meters to measure the liquid flow rate, several thermocouples and absolute and differential pressure sensors. The test matrix spans the following ranges: test section inlet temperature (92-96.8 ^{o}C), liquid superficial velocities (011-0.14 m/s) and heater power (7.2-10.9 kW). The wire mesh sensors provide local void fraction, bubble size distributions and velocity of the steam bubbles which are produced due to flashing in the adiabatic section. Three-dimensional flow visualization, obtained using reconstruction techniques of the wire-mesh sensor data, are used to verify the flow-regime map of Mishima and Ishii (1984).

The experimental test loop used by Zeitoun (1994) consists of a 20-liter holding tank where the water temperature is regulated using an immersion heater and a cooling coil. The degassed water is pumped through a rotameter, a preheater and into the bottom of the vertical test section. Finally, the single-phase liquid at the end of the test section is pumped back to the holding tank. The test section is a vertical concentric annulus with an internal tube diameter of 12.7 mm divided into three axial sections and an external diameter of 25.4 mm (hydraulic diameter, D_h, of 12.7 mm). The three inner sections consist of a heated section of 0.306 m long made of thin walled stainless-steel tubes (0.25 mm thickness) followed and preceded by unheated sections of length 0.34 m and 0.5 m, respectively, made of 0.7-mm-thick copper tubes. The outer tube is made of plexiglass to permit visual observation. The setup was used to study subcooled flow boiling in the heated section and condensation in the unheated region. The void generated in the heated section acted as an inlet condition for the study of bubble size and condensation in the unheated section. The measurements taken for the condensation study include pressure at the test section inlet, liquid subcooling temperatures at the inlet and 10 cm along the unheated section, flow rate upstream of the test section, bubble size, and axial area-averaged void fraction. The bubble size and void fraction measurements were taken at various points along the channel. Additional details regarding the measurement techniques are described in Zeitoun (1994). The eight condensation datasets span the following parameters: pressure (103-180 kPa), inlet liquid subcooling (2.6-18.8°C), and mass flux (139.3-506.2 kg/m^2-s).

CHAPTER 3. EXPERIMENTAL APPROACH

The need for a comprehensive condensing flow database is articulated in Chapter 2, especially one with a sufficient number of two-group conditions to validate the proposed two-group IATE formulation for condensing flows. This chapter describes the experimental data collected in the new facility. A test matrix is formulated for performing condensation, flashing and saturation experiments in the annulus facility. The dataset was designed for validation of one-dimensional system codes and multi-dimensional computational fluid dynamics codes. Detailed local measurements of three representative cases are shown to highlight the complexity of local two-phase flow phenomena observed along the test section. A parametric analysis is also conducted to show the sensitivity of system parameters on the axially evolving two-phase flow. The focus of the adiabatic steam-water flow fills an important gap in validation data between the simplified hydro-dynamic data of air-water flow and the complex thermo-fluid dynamic data of boiling flows.

3.1. Experimental Facility

3.1.1. Description of Components

The schematic of the test facility shown in Figure 3.1 (a) consists of three sections; the primary loop, test section bypass and the pressurizer. In the primary loop, a vertical centrifugal pump (Grundfos, Olathe, KS) is capable of pumping water upto to a temperature of 180^{o}C and a pressure of 1 MPa. The pump motor speed can be regulated using a built-in controller which helps adjust the flow rate. An electromagnetic flowmeter (Siemens, Hauppauge, NY) located downstream of the pump is used for the flow rate measurements. After passing through the flowmeter, the water enters a vertical 18 kW preheater (Watlow, St. Louis, MO). The pre-heater is used to set the inlet subcooling to the test section and is governed by a PID controller (Tempco, Wood Dale, IL) based on a thermocouple located close to the exit of the preheater. The preheater is also used along with the cartridge heater in the test section to degas the system. A globe valve located downstream of the preheater is used for fine adjustment of flow rate and flow stabilization by providing a high frictional loss. The pump controller provides a course flow rate control while the globe valve is used for fine adjustments. After the globe valve, the flow enters the test section injection port.

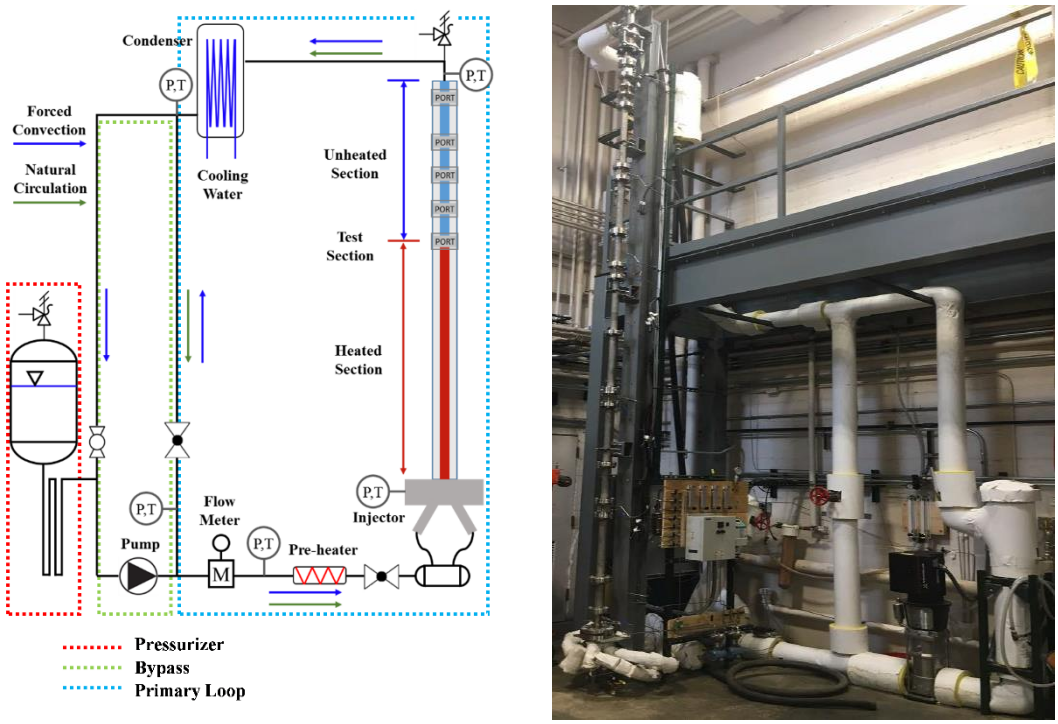

Figure 3.1 (a) Schematic of the experimental facility (b) Picture of the experimental facility without test section insulation

The test section is composed of several components: an injection port, five instrumentation ports, a cartridge heater, glass view ports, and stainless-steel piping sections for the outer wall. The test section is a vertical annulus of 5.19 m length with an external diameter of 38.1 mm of stainless-steel piping surrounding a 19.05 mm outer diameter stainless-steel rod. The start of the heated section is located 203 mm downstream of the inlet. The heated section, which is 3000 mm (±25 mm) long, is succeeded by 1990 mm of unheated section. Power to the cartridge heater rod is provided by a solid-state controller unit and has a maximum heating power of 54 kW or a maximum heat flux of 300 kW/m^2. The test section is well insulated with fiberglass throughout its length, and six spacers are used along the test section to ensure proper alignment of the inner rod.

The pressurizing system comprises of a pressurizing tank, nitrogen tank, regulator, and surge line. In addition to setting the pressure condition at the inlet of the test section, the pressurizing tank provides a compressible space to absorb pressure fluctuations in the primary loop. The pressurizing tank is filled with water up to three-fourth of its capacity with the remaining volume pressurized with nitrogen. The primary side of the facility and the pressurizing tank are connected with a surge line of over 5 m to limit the diffusion of nitrogen into the degassed system.

Table 3.1 Summary of the annulus facility

Parameter	Value
Geometry	Vertical internally-heated annulus
Inner diameter [mm]	19.05
Outer diameter [mm]	38.1
Heated length [m]	3.0
Unheated length [m]	1.99
Maximum Design Pressure [kPa]	1000
Maximum Heater power [kW]	54 (300 kW/m^2)
Maximum inlet velocity [m/s]	4.0

Water used in the test facility is filtered with a 1 MΩ four-bed water deionization system. To maintain the quality of the treated water approximately 10 ml morpholine solution and ammonium hydroxide is added to maintain the conductivity of water at a minimum of 40 μS. Non-condensable gases are removed from the system before each experiment through a careful degassing procedure. Water is heated with the preheater and the main cartridge heater to its saturation temperature in the test section, and the vapor is condensed in the condenser which causes the non-condensable gases to accumulate at the top of the facility. The trapped gases are eliminated frequently through vent lines.

Once the system is degassed, the cartridge heater and the preheater are used in conjunction to set the bulk temperature at the end of the heated section to the desired subcooling. The test conditions are set up based on three flow parameters, i.e. the system pressure, the subcooling at the end of the heated section, and the fluid flow rate. The system pressure is controlled through the pressurizing tank, the subcooling is set through the power level of main heater and the preheater, and the flow rate is changed through adjusting the pump motor speed and the frictional loss imposed at the globe valve. Steady-state conditions are achieved by balancing the heat removal with respect to the heat input through controlling the flow rate of the cooling water on the secondary side of the condenser.

3.1.2. Instrumentation

The local measurements of pressure, temperature and two-phase parameters (using four-sensor conductivity probes) are obtained using instrumentation ports shown in Figure 3.2. The unique feature of the instrumentation port is the traversing mechanism which is used for positioning the four-sensor conductivity probes and/or thermocouples at different radial locations. The traversing mechanism consists of a traversing table (Thor labs, Newton, NJ) controlled using precision screw gauges with a resolution of 10 μm fitted onto an angle plate which is attached to

the instrumentation port using stainless steel bellows. The conductivity probe is attached to the angle plate using Conax compression seal fittings (Conax Buffalo technologies, Buffalo, NY), through the bellows. The bellows ensure a flexible coupling between the traverse table and the instrumentation port as well as acting as a flexible sealant for pressure upto ~ 1MPa and temperatures upto 180^{o}C. Each instrumentation port can accommodate one traversing mechanism on each of its three sides with fittings for pressure taps and thermocouples machined on the fourth side. The pressure taps which are at the same elevation as the tip of the conductivity probe, are connected to one end of the differential transducer with the other end connected to the injection port. Therefore, local pressure measurements can be obtained with reference to the injection port. The summary of the instrumentation used in the experimental facility is given in Table 3.2.

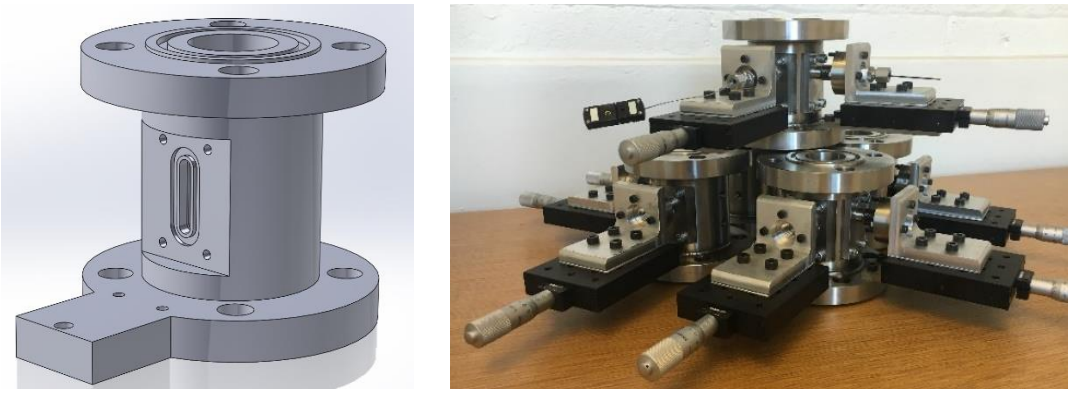

(a) **(b)**

Figure 3.2 (a) 3-D drawing of an instrumentation port without the traverse (b) Instrumentation ports for the test facility with traverses attached.

The local two-phase parameters i.e. void fraction, bubble interface velocity, interfacial area concentration and Sauter mean diameter are measured in the test section using four-sensor conductivity probes. Conductivity probes, proposed by Neal and Bankoff (1963), are a class of widely used electrical impedance probes for air-liquid flows, based on the principle of the difference in conductivities between the gas and the liquid phase. A single-probe consists of a needle which is insulated except for the tip (typically < 1mm diameter). When a voltage is applied to a sensor and the tip makes contact with the conducting liquid phase, the circuit is complete between the sensor and the ground yielding a baseline signal. The reverse happens during contact with the non-conducting gaseous phase resulting in an open circuit giving a high voltage signal. The local time-averaged void fraction is obtained by the proportion of the time occupied by the gaseous phase. Using two sensors (double sensor conductivity probe), the bubble interface velocity

can be measured by the time delay of the voltage signal between the leading and trailing probe. The interfacial area concentration is obtained from the bubble interface velocity using Eq. (1.11). There are two key assumptions adopted in the double sensor conductivity probe measurements; bubbles are spherical in shape and every part of the bubble can intersect the probe with equal probability (Wu and Ishii, 1999). Moreover, double sensor conductivity probes can only measure the bubble interfacial velocity component along the probe orientation. To remove the restrictions regarding the bubble shape and bubble velocity components, a four-sensor conductivity probe was proposed (Kataoka et. al, 1986; Revankar and Ishii, 1993), shown in Figure 3.3.

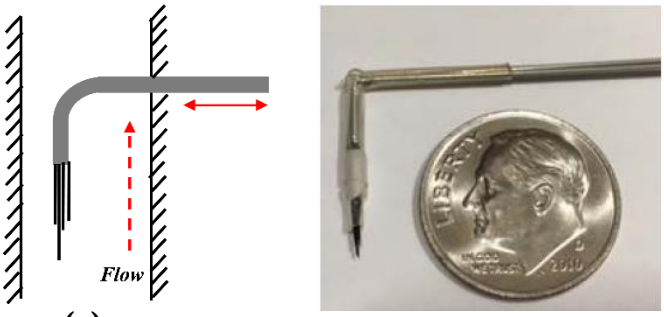

Figure 3.3 (a) Schematic of a four-sensor conductivity probe in the test section (b) Top-view of a four-sensor conductivity probe used in the current study.

The four-sensor conductivity probe consists of one leading sensor and three trailing sensors, forming three pairs of double sensor probes. The three pairs of double sensor probes are used to measure three independent interfacial bubble velocity components. The construction of the four-sensor conductivity probes used in this study follow from the foundational works by other researchers (Kataoka et. al, 1986, Revankar and Ishii, 1993, Kim et al., 2000). For signal processing, spherical and distorted bubbles are categorized as group-1 bubbles while cap, slug, and churn-turbulent bubbles are categorized as group-2 bubbles with the group boundary defined as the maximum distorted bubble diameter, D_c defined in Eq (1.11). The signal processing algorithms used to obtain the two-phase flow characteristics are based on Kim et al. (2000) and Fu (2001). Worosz et. al (2016) performed a detailed study to analyze various practical aspects of the conductivity probe measurement system. Based on previous works using similar probe design (Kim et al., 2000; Ozar et al., 2013a; Worosz et al., 2016), the uncertainty in two-phase parameters is taken as ±5% for void fraction, ±10% for interfacial area concentration and conservatively ±10% for gas velocity. A sampling duration of two minutes is used in the current study for all the conditions to ensure large number of bubbles measured. The uncertainty values for the measurements recorded in the test facility are summarized in Table 3.3.

Table 3.2 Summary of the instrumentation in the experimental facility

Measurement	Instrument	Axial Locations (z/D_h)
Void fraction Gas velocity Interfacial area concentration Sauter Mean diameter	Conductivity Probe	0.0, 19.5, 39.1, 60.5, 93.3 (11 radial locations)
Bulk Liquid temperature	T-type Thermocouples	T.S. Inlet, 0.0, 19.5, 39.1, 60.5, 93.3
Pressure	Pressure Transducer	T.S. Inlet, 0.0, 19.5, 39.1, 60.5, 93.3
Inlet liquid flow rate	Magnetic flow meter	Upstream of Injector

* z/D_h measured from reference location 1.0 (i.e. 1st measurement port)

Table 3.3 Measurement uncertainty in the experimental facility

Measurement	Uncertainty (Maximum)
Pressure [kPa]	±1.5 [a,b]
Temperature [^{o}C]	±0.1 [c,d]
Mass Flux [kg/m^2-s]	±7.0 [b,e]
Power [kW]	±1.7 [f,g]
Void fraction [-]	±5% [h]
Gas velocity [m/s]	±10% [h]
Interfacial area concentration [1/m]	±10% [h]

a. Product Data Sheet - Rosemount 3051 Pressure Transmitter, Emerson Process Management Sep. (2014).
b. OPERATING INSTRUCTIONS AND SPECIFICATIONS, NI 9203, National Instruments.
c. Wire Color codes and accuracy, Omega, https://www.omega.com/techref/colorcodes.html.
d. OPERATING INSTRUCTIONS AND SPECIFICATIONS, NI 9214 with TB-9214, National Instruments.
e. Operating Instructions - SITRANS F, Siemens (2010).
f. Users Manual, 80 Series V Multimeters, FLUKE (2008).
g. Instruction Sheet, i200/i200s AC Current Clamp, FLUKE (2005).
h. Kim et al. (2000), Ozar et al. (2013a), Worosz et al. (2016)

Table 3.4 Summary of test matrix.

Parameter	Value
No. of conditions	85
Port-1 Pressure [kPa]	190-930
Port-1 total void fraction [-]	3-43%
Mass Flux [kg/m^2-s]	258-1688
Port-1 subcooling [^{o}C]	0-3.3

3.2. Test Matrix

The conditions presented in this work span the following ranges: port-1 subcooling of 0-3.3 °C, total area-averaged port-1 void fraction of ~3-43% and test section mass flux of 258-1688 kg/m^2-s (summarized in Table 3.4). 29 conditions are recorded at low pressure (less than 400 kPa), and 56 conditions are taken at elevated pressure (between 500 and 930 kPa). Conditions for the new database are based on the combined influence of all the four parameters i.e. mass flux, inlet liquid subcooling, system pressure, and inlet void fraction. The database spans total area-averaged void fraction up to 65% at the exit of the test section. The proposed test matrix for two-group condensing cases is designed with the following considerations in mind;

1. At low pressures (approx. < 350 kPa), the local liquid temperature becomes superheated because of the continued pressure drop almost entirely due to the gravitational head causing flashing along the experimental domain. Flashing is an important phenomenon to take into account especially at low-pressure, low flow conditions and the closure relations for flashing require significant improvement.

2. It must be noted that suitable conditions for the new database will be based on the combined influence of all the four controlling parameters i.e. mass flux, inlet liquid subcooling, system pressure and inlet void fraction. Nonetheless, the influence of each of the four parameters can be analyzed separately as follows. A higher mass flux implies a smaller bubble residence time and consequently a lower condensation rate. A high mass flux could lead to an insignificant reduction in void fraction along the experimental domain and vice versa. Similarly, a higher subcooling would result in higher condensation rates, which is desirable. However, it should not be high enough that all the void condenses before the second measurement port. The same argument applies to the input void fraction which is indirectly controlled using the wall heat flux.

3. It is important that the new experimental database has sufficient number of one-group and two-group conditions which can be achieved by the following criteria; for one-group conditions, the group-2 void fraction should be a significantly lower proportion of the total void fraction and for two-group conditions, the inlet group-2 void fraction should be significant. Additionally, a higher proportion of group-2 void fraction could be considered for one-group analysis if the group-2 void fraction condenses immediately.

4. The condensation databases available in the public domain only provide a local subcooling instead of the local temperature profile which is required to calculate the area averaged subcooling. To provide for an accurate area averaged local subcooling, which is a critical input parameter for the one-dimensional condensation model validation, the temperature profile is measured in the current study.

3.3. Local Measurements of Two-Phase Parameters

Figures 3.4-3.6 (Kumar et al., 2019) show the local conductivity probe and thermocouple measurements for each instrumentation port for three representative conditions. The local two-phase parameters measured by the conductivity probe are the void fraction, α_g, the interfacial area concentration, a_i, the gas velocity, v_g, and the Sauter mean diameter, D_{Sm}. Every row of plots in the three figures corresponds to an instrumentation port, whose axial location with reference to port-1 is specified in the figure. For the two-phase (conductivity probe) measurements, black-circle markers indicate group-1 (small spherical/distorted bubbles) measured values, the blue-square markers indicate group-2 (cap/slug/churn-turbulent bubbles) measured values. All the local measurements are shown in terms of the non-dimensional radial location (henceforth referred to as radial location) with '0' referring to the inner-wall and '1' referring to the outer-wall. Both the conductivity probe and thermocouple measurements are taken at 11 radial locations (0.1-0.9) with a finer resolution in the near wall region. It is assumed in the measurement procedure that the steady state time-averaged flow condition has negligible circumferential variation in flow parameters.

General observations can be made for the conditions shown in Figures 3.4-3.6. At port-1, which is at the exit of the heated section, the group-1 void fraction has a heated-wall peak profile with the bubble layer thickness strongly dependent on the degree of liquid subcooling. The local liquid temperature measurements which are shown along with the saturation temperature based on local pressure, are the highest at the heated wall for port-1. However, in Figure 3.6, which is a saturated inlet condition, the group-1 wall peaking is absent which results in a uniform group-1 void fraction profile. For the downstream ports, the liquid temperature maintains the wall peaking for conditions shown in Figure 3.4 and Figure 3.5. The reason for the thermal boundary layer retaining its shape in the adiabatic region is because of the density gradient which is advected with the flow. The temperature profile flattens out eventually as the flow gets mixed. It must be stressed that extensive heat loss tests indicate that the heat loss throughout the test facility is negligible, especially in the unheated region which is the focus of the current study. Area-averaged temperature profiles which are discussed later, further highlights this point. In contrast, the group-2 void fraction

profile shows an off-wall peaking. Group-2 void fraction is generated due to coalescence and expansion of group-1 bubbles. The figures also show that group-2 bubbles are generated even at low (less than 10%) void fraction. The interfacial area concentration is mostly dominated by the presence of group-1 bubbles even when the group-2 void fraction is higher because group-1 bubbles have a much greater surface area per unit volume relative to group-2 bubbles. For all three conditions, the inner-wall-peaked void fraction profile from the upstream boiling is not seen by the second measurement port. Additionally, downstream of port-1, the group-2 bubbles have a core-peaked void fraction profile which is similar to adiabatic air-water flows where the larger bubbles tend to move toward the center of the channel (Ozar et al., 2013). This lateral migration of the two-phase distribution is beneficial for a benchmark of interfacial forces in a multi-dimensional simulation. Finally, the local gas velocity of group-2 bubbles is higher than group-1 bubbles.

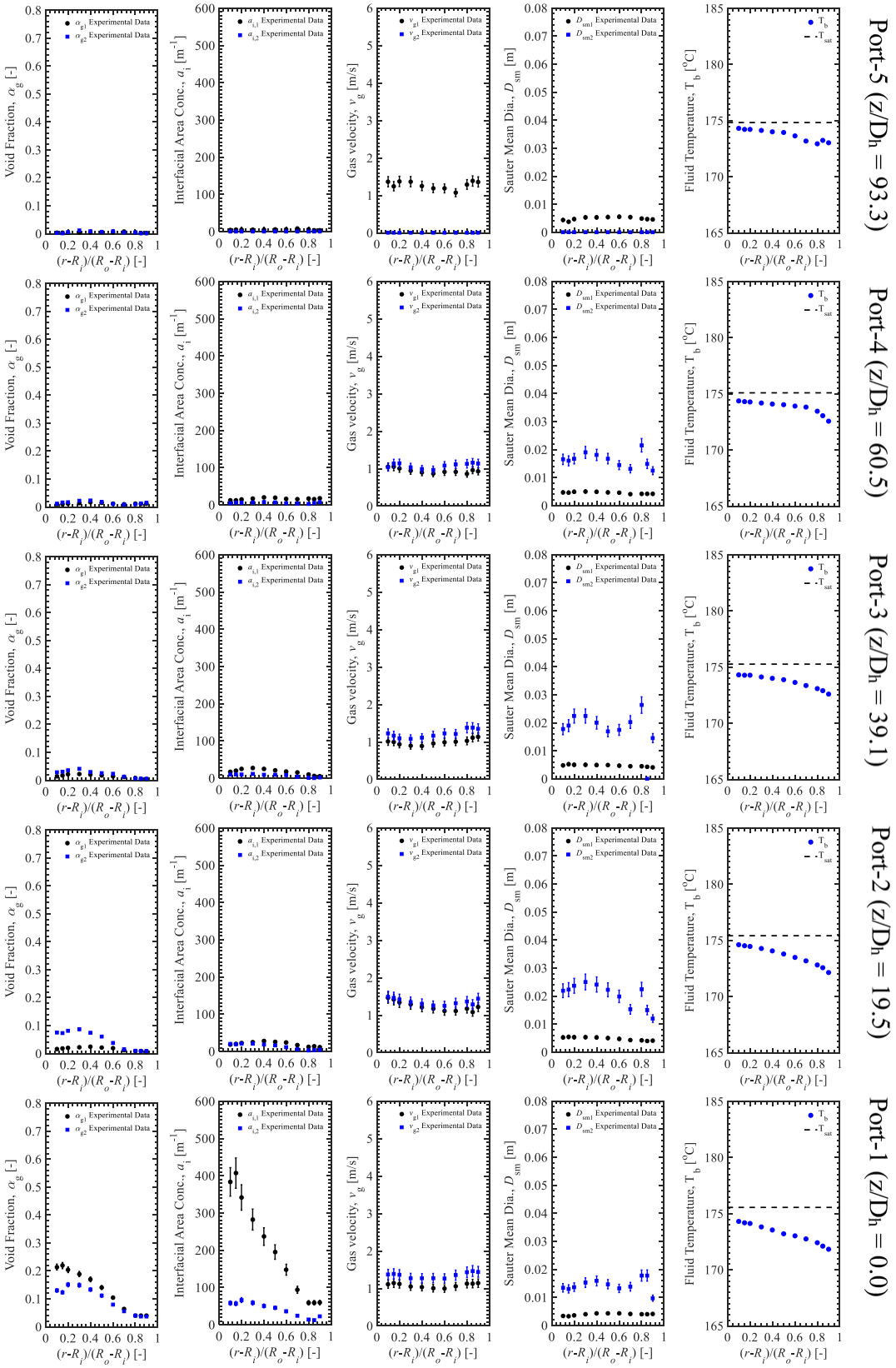

Figure 3.4 Local measurements for: P_{P1} = 904 kPa, G_{TS} = 693 kg/m^2-s, $\langle \Delta T_{sub,P1} \rangle$ = 2.5 °C, $\langle \alpha_{t,P1} \rangle$ = 18.8%.

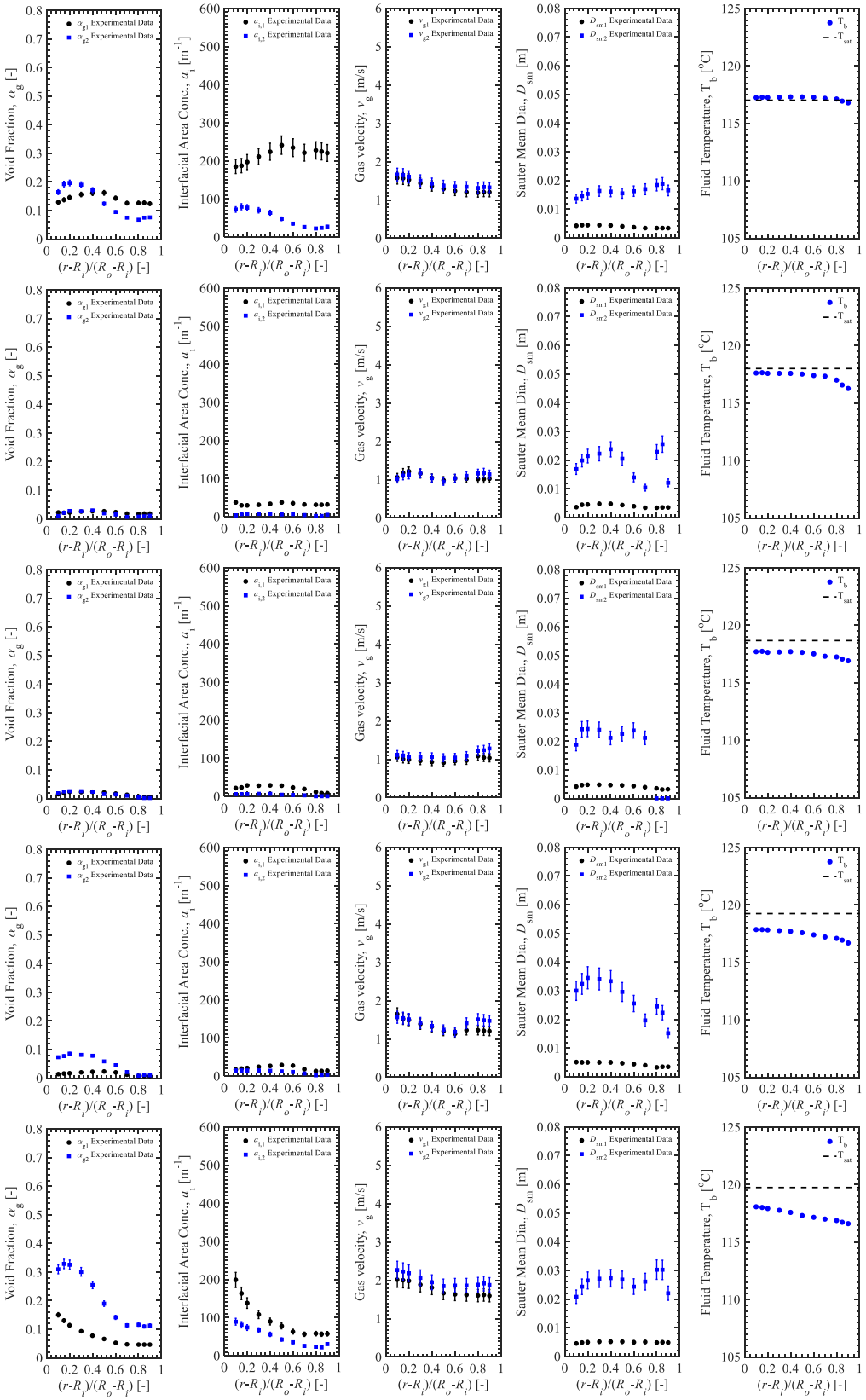

Figure 3.5 Local measurements for: P_{P1} = 197 kPa, G_{TS} = 938 kg/m^2-s, $<\Delta T_{sub,P1}>$ = 2.4 ^{o}C, $<\alpha_{t,P1}>$ = 23.8%.

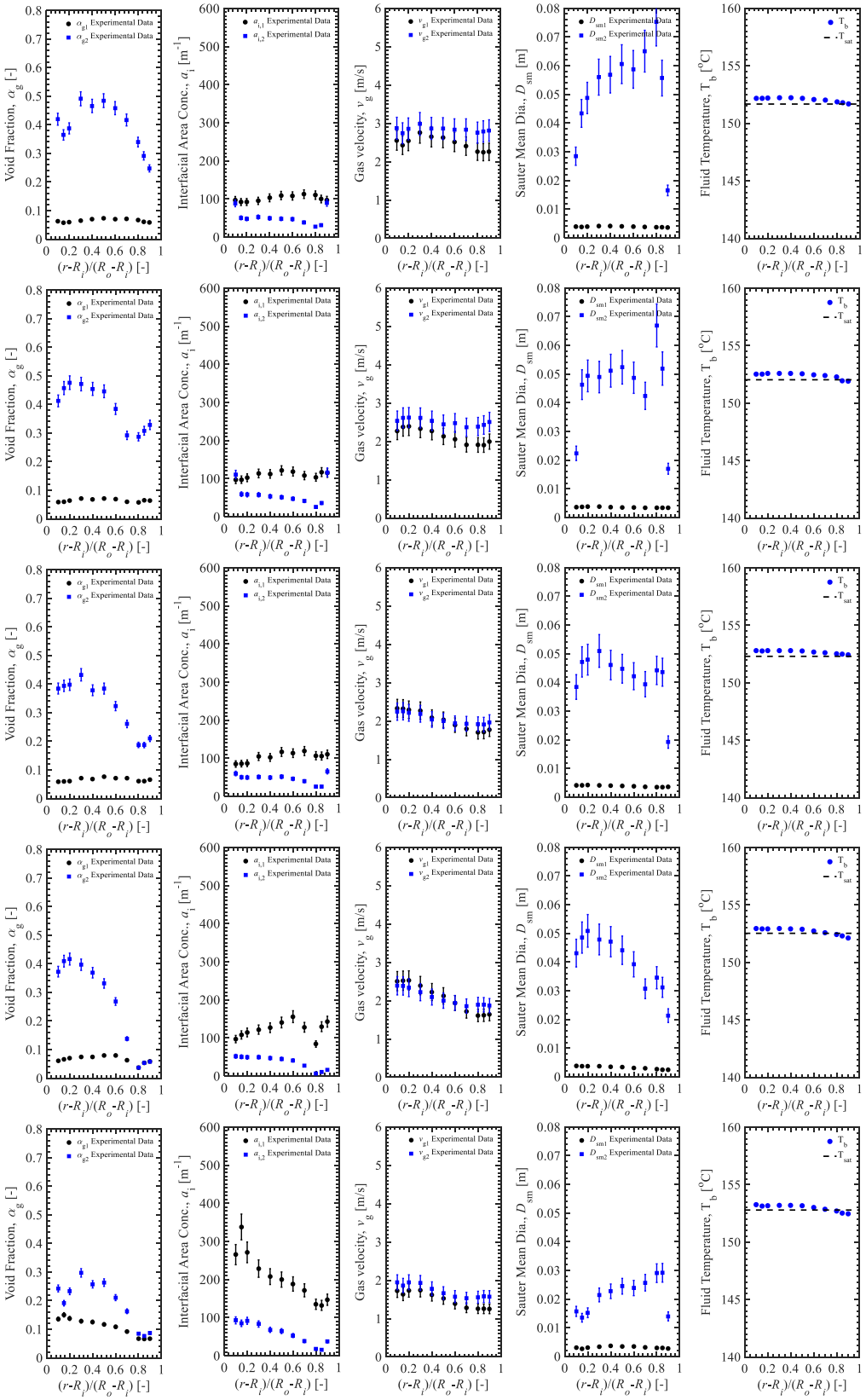

Figure 3.6 Local measurements for: P_{P1} = 513 kPa, G_{TS} = 1195 kg/m^2-s, $\langle \Delta T_{sub,P1} \rangle$ = -0.14 ^{o}C, $\langle \alpha_{t,P1} \rangle$ = 26.6%.

Focusing on observations particular to Figure 3.4, it can be seen that the local subcooling drives the rapid condensation of void fraction, resulting in a negligible group-1 void fraction by port-2. Due to the elevated system pressure of this condition however, the saturation temperature does not change substantially across the flow length. The group-2 void fraction does not rapidly condense as compared to group-1 void fraction because of the lower interfacial area concentration. The remaining group-1 void fraction is produced through the condensation of group-2 bubbles. This highlights the importance of this dataset to study two-group condensation models, particularly to validate group Nusselt number correlations and inter-group mass transfer coefficients which is a limitation to modeling gas-dispersed condensing flow (Kumar and Brooks, 2018). The local interfacial area concentration profile being dominated by group-1 bubbles, shows a very sharp drop from port-1 to port-2, in comparison to the corresponding reduction in total void fraction. Lastly, the slight increase of group-1 Sauter mean diameter is due to group-2 bubbles becoming group-1.

The condition shown in Figure 3.5 is a subcooled inlet flow condition, similar to Figure 2, and therefore similar two-phase characteristics are observed, particularly across ports 1 to 3. However, the system pressure is lower which results in a larger decrease of saturation temperature along the flow channel, as observed in the local temperature plots. At low pressure, small temperature differences can lead to a large change in void fraction over a short distance, be it subcooling which rapidly decreases the void from ports 1 to 3 or superheat which results in flashing flow conditions from ports 4 to 5 leading to a large void production. Given that these temperature differences are the driving force for phase-change, this presents a substantial challenge for modeling. Interestingly, due to the temperature profile across the flow area at port 4 which is superheated for most of the flow channel but subcooled near the outer wall, a bubble near the inner wall will undergo flashing while condensing near the outer-wall. This phenomenon is difficult to capture in a one-dimensional description of the flow and would require an averaging covariance between the temperature difference and interfacial area concentration in the mass generation term (Dandekar and Brooks, 2016). Flashing results in a relatively uniform group-1 void fraction profile across the flow channel, as observed in ports 4 to 5.

A saturated condition at an elevated pressure is shown in Figure 3.6. Unlike the previous two conditions, the bulk liquid temperature is saturated at port-1. Due to decreasing saturation temperature, void fraction increases from ports 1 to 5 due to flashing. The rate of increase in the local void fraction is large from ports 1 to 4 before plateauing from ports 4 to 5. The group-1 void fraction is relatively uniform across all five ports for reasons discussed earlier. The group-1 void fraction and interfacial area concentration decrease from port-1 to port-2 because of inter-group mass transfer to group-2 and remain constant across the remaining ports because of a balance of

production and inter-group mass transfer. At ports 4 and 5, the group-2 interfacial area concentration shows a wall-peaking profile. This is because of the near-wall contribution of vertical interfaces in slug bubbles to the interfacial area concentration. An opposite trend is observed in the Sauter mean diameter profile in ports 4-5. The magnitude of the Sauter mean diameter also indicates the presence of slug bubbles with large chord lengths. Lastly, the gas velocities accelerate from ports 1-5 due to large vapor generation.

3.4. Parametric Study of Area-Averaged Two-Phase Parameters

A parametric study of the independent flow parameters (system pressure, inlet mass flux, and port-1 subcooling) is conducted to study their effect on the two-phase flow characteristics, particularly to highlight the sensitivity of two-phase flow to minor changes in the flow parameters. A one-dimensional flow description is provided by area area-averaging and void-weighted averaging of the local two-phase parameters. The black circles in Figures 3.7-3.12 (Kumar et al., 2019) represent group-1 values, the blue squares represent group-2 values, and red diamond markers represent the total (1-group) values.

Figure 3.7 shows the area-averaged axial measurements for three subcooled inlet conditions which span system pressures ranging from low to elevated, with the inlet mass flux, port-1 subcooling and port-1 total area-averaged void fraction held approximately constant. For all three cases, the area-averaged group void fractions condense quickly from port-1 to port-2 because of the bulk liquid subcooling. However, at a low system pressure, the flow starts to flash in the downstream ports because of a (linearly) decreasing saturation temperature along the flow channel. As mentioned previously, a small change in the difference between the saturation temperature and the bulk liquid temperature can lead to a significant generation of void fraction. The total area-averaged void fraction produced at the end of the flow channel through flashing is approximately equal to that produced by the upstream boiling section, as shown by Figure 3.7(a). For all three conditions, the area-averaged temperature (shown in black markers) and the centerline temperature (shown in red diamonds) are approximately constant throughout the flow channel, demonstrating the test facility is well insulated. The area-averaged interfacial area concentration sharply drops from port-1 to port-2 following the decrease in group-1 void fraction. A rapid increase in interfacial area concentration is seen at port-5 of Figure 3.7(a) following the void fraction profile. Lastly, the group-2 Sauter mean diameter axial profiles for all three conditions show a slight increase due to inter-group transfer, followed by a steady decrease due to condensation.

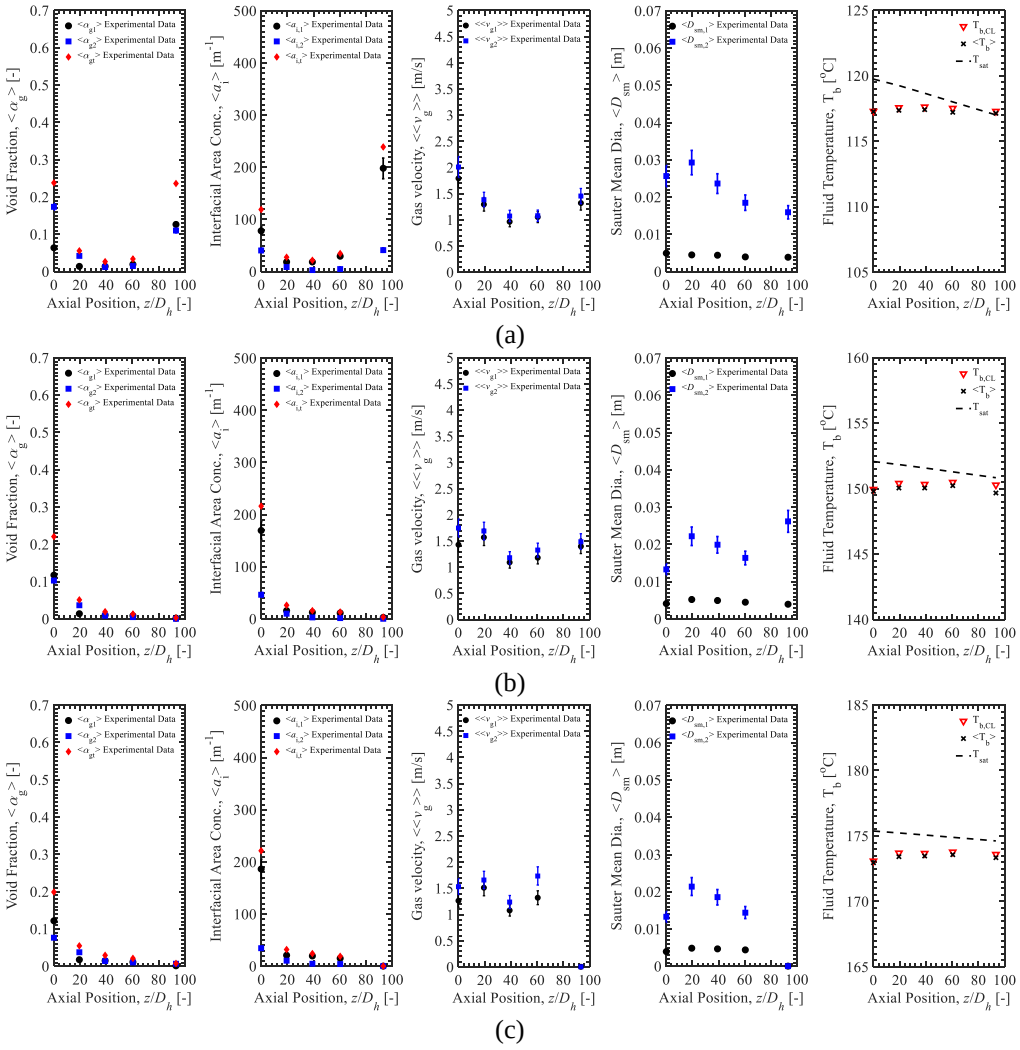

Figure 3.7 Axial measurements for system pressure comparison for subcooled inlet: (a) P_{P1}=197 kPa, G_{TS}=938 kg/m^2-s, $\langle\Delta T_{sub,P1}\rangle$=2.5 ºC, $\langle\alpha_{t,P1}\rangle$ = 23.8%, (b) P_{P1}=503 kPa, G_{TS}=929 kg/m^2-s, $\langle\Delta T_{sub,P1}\rangle$=2.3 ºC, $\langle\alpha_{t,P1}\rangle$ = 22.1%, (c) P_{P1}=900 kPa, G_{TS}=897 kg/m^2-s, $\langle\Delta T_{sub,P1}\rangle$=2.4 ºC, $\langle\alpha_{t,P1}\rangle$ = 19.9%.

Similarly, Figure 3.8 shows the area-averaged axial measurements for four saturated inlet conditions of varying system pressures with inlet mass flux and port-1 total area-averaged void fraction, held approximately constant. The total area-averaged void faction significantly increases along the test section for the low-pressure condition due to flashing, in comparison to the elevated pressure conditions which exhibit a small increase to a steady void fraction profile, typical of saturated boiling. It is critical that constitutive models for flashing flow account for this pressure effect for accurate predictions of two-phase parameters. The total void fraction decreases from ports 1 to 2 in the elevated pressure conditions because of slight subcooling in the outer-wall region. The trends in interfacial area concentration, Sauter mean diameter and gas velocities for all four conditions, follow from the discussion of the local plots.

The variation of inlet mass flux for three different mass fluxes for a subcooled inlet is shown in Figure 3.9. For a constant inlet subcooling and total area-averaged inlet void fraction, it can be observed that the void fraction decreases more rapidly along the test section when the inlet mass flux is lower. This is because at a lower mass flux the bubble has a longer residence time and will condense within a shorter distance for the same condensation rate. The rate of decrease in interfacial area concentration along the flow channel for the three conditions is following from the decrease in void fraction. A parametric variation of inlet mass flux for a saturated inlet is shown in Figure 3.10, for three different mass fluxes. It is interesting that no discernable mass flux effect is observed for the range of conditions shown. One possible explanation could be that the mass flux effect is only observed for subcooled inlet flows which flash along the test section, particularly at low-pressure, low-flow conditions.

Figure 3.11 and Figure 3.12 show the axial measurements for different inlet subcoolings at a low and elevated system pressure for constant inlet mass flux and total area-averaged void fraction. For a smaller inlet subcooling, the decrease in void fraction along the flow channel is less because of a lower condensation rate. At low system pressure, flashing occurs for the condition shown in Figure 3.11(a) because of a decrease in the saturation temperature along the flow channel and a higher exit temperature as a consequence of a lower inlet subcooling, leading to a sharp rise in port-5 void fraction and interfacial area concentration. At elevated system pressure in Figure 3.12, the saturation temperature decrease is less than the low-pressure conditions, reducing the likelihood of flashing.

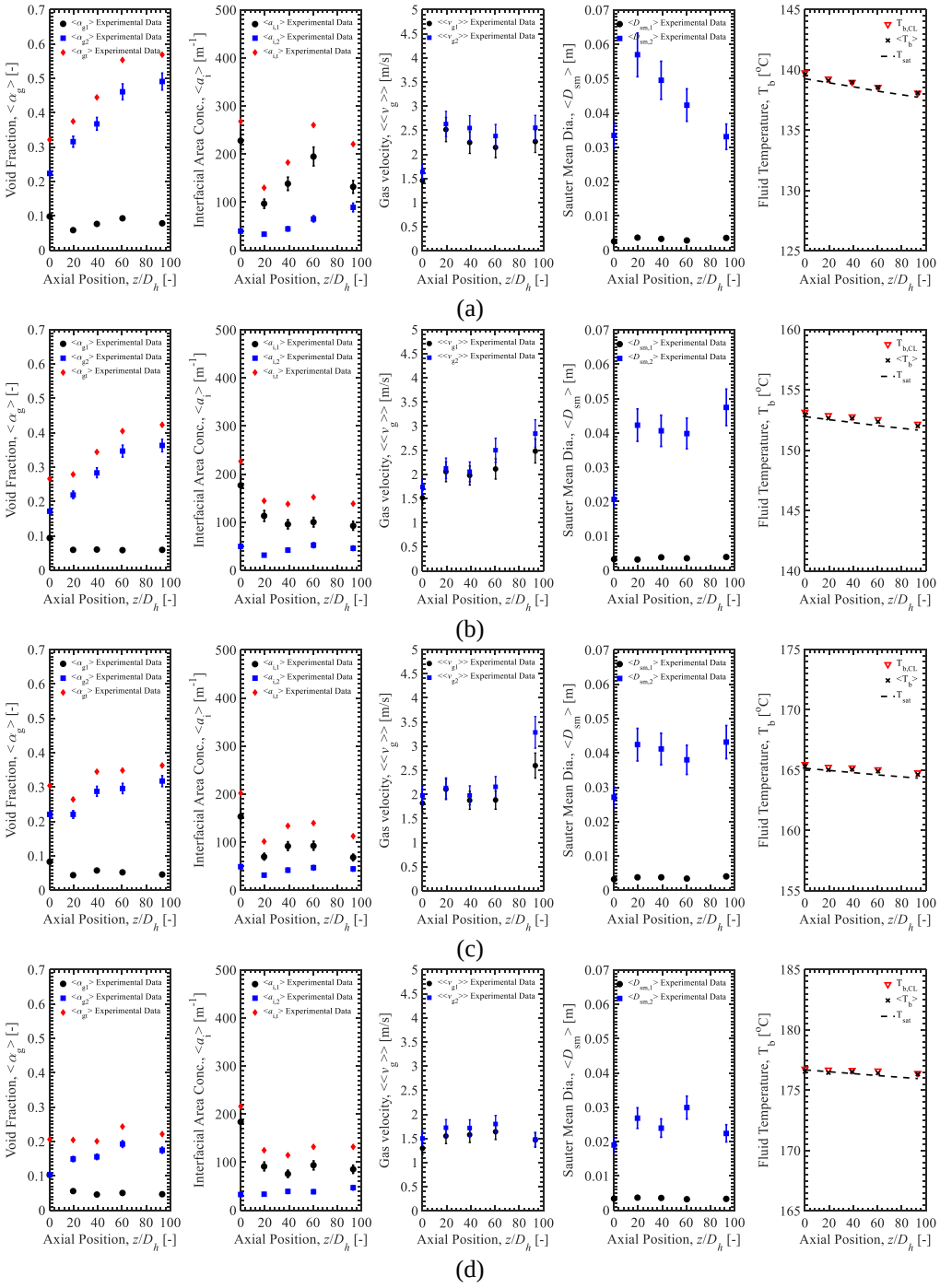

Figure 3.8 Axial measurements for system pressure comparison for saturated inlet: (a) P_{P1}=354 kPa, G_{TS}=1165 kg/m^2-s, $<\alpha_{t,P1}>$ = 32.2%, (b) P_{P1}=513 kPa, G_{TS}=1195 kg/m^2-s, $<\alpha_{t,P1}>$ = 26.6%, (c) P_{P1}=704 kPa, G_{TS}=1134 kg/m^2-s, $<\alpha_{t,P1}>$ = 30.4%, (d) P_{P1}=929 kPa, G_{TS}=1185 kg/m^2-s, $<\alpha_{t,P1}>$ = 20.6%.

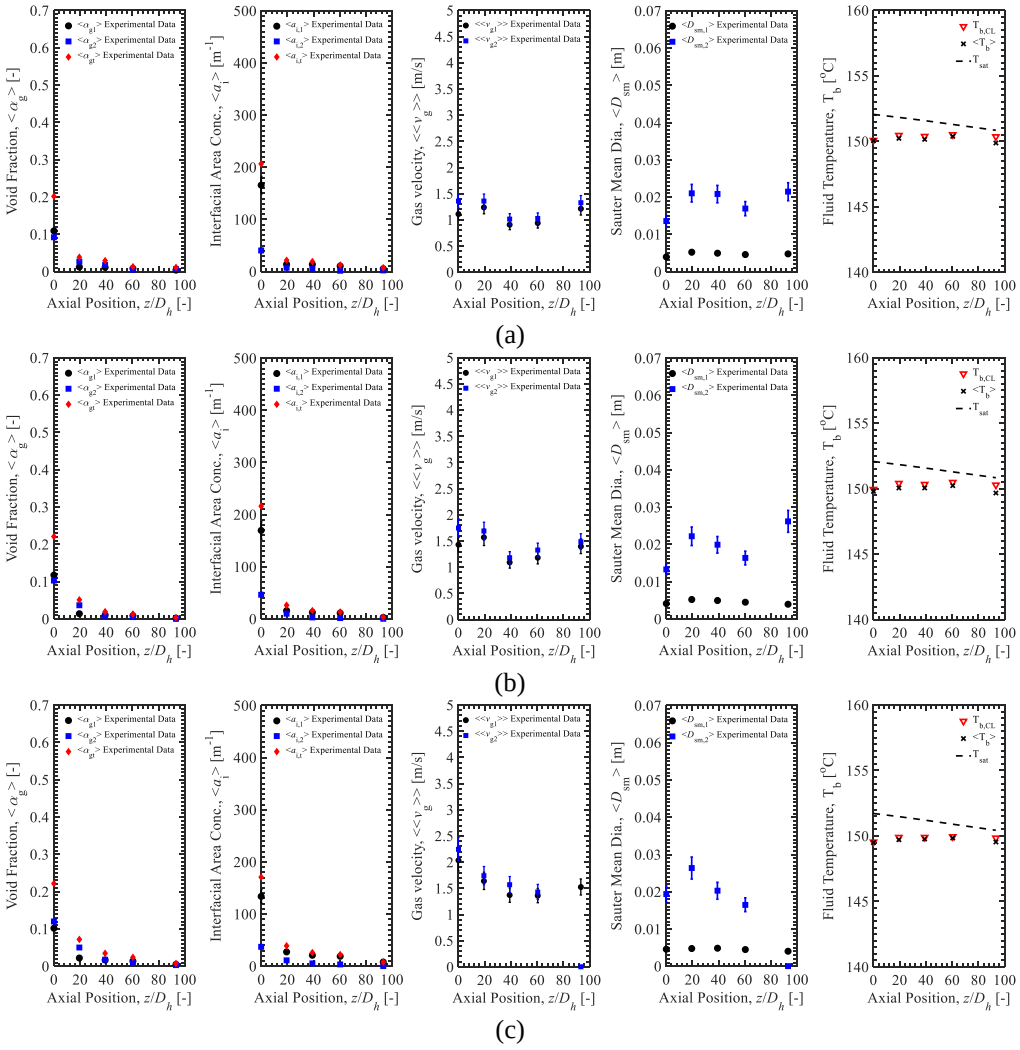

Figure 3.9 Axial measurements for mass flux comparison for subcooled inlet: (a) P_{P1}=503 kPa, G_{TS}=702 kg/m^2-s, $\langle\Delta T_{sub,P1}\rangle$=2.0 ^{o}C, $\langle\alpha_{t,P1}\rangle$ = 20.2%, (b) P_{P1}=503 kPa, G_{TS}=929 kg/m^2-s, $\langle\Delta T_{sub,P1}\rangle$=2.3 ^{o}C, $\langle\alpha_{t,P1}\rangle$ = 22.1%, (c) P_{P1}=498 kPa, G_{TS}=1158 kg/m^2-s, $\langle\Delta T_{sub,P1}\rangle$=2.2 ^{o}C, $\langle\alpha_{t,P1}\rangle$ = 22.2%.

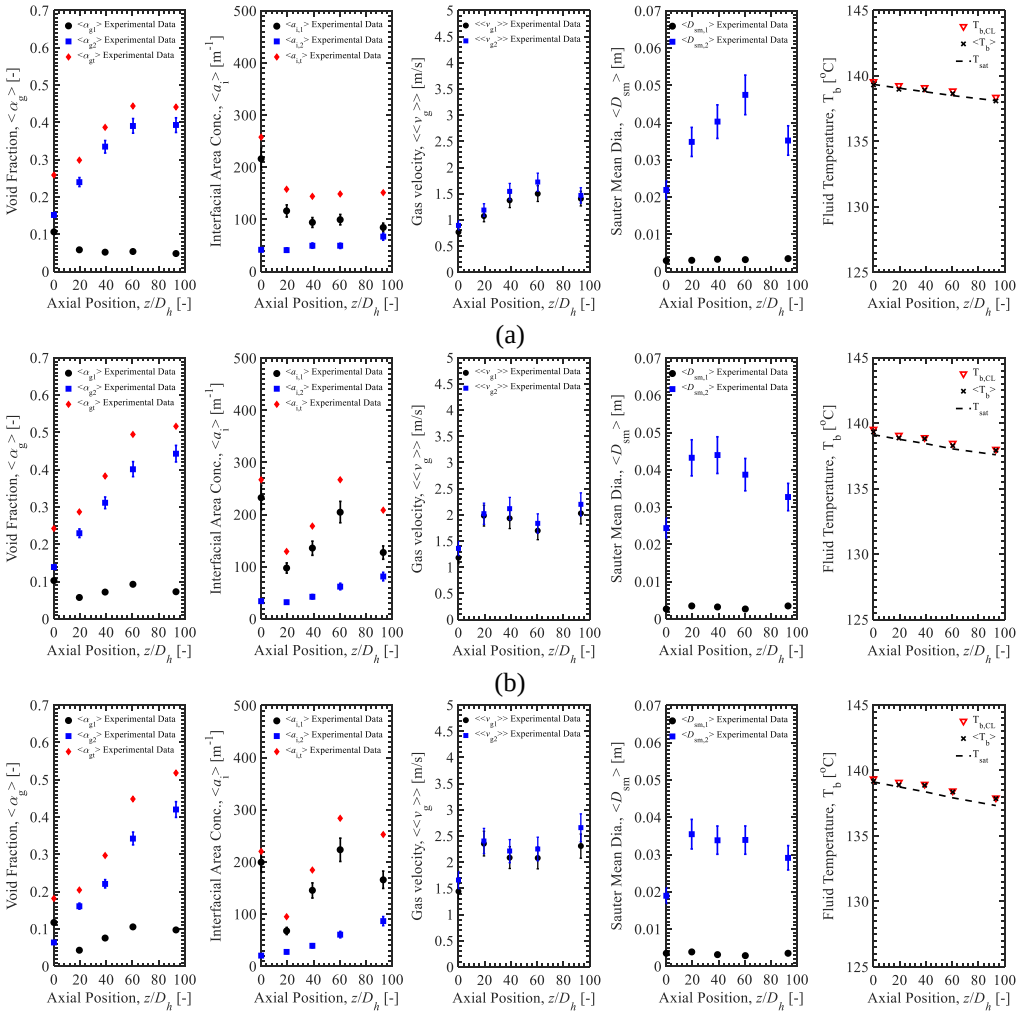

Figure 3.10 Axial measurements for mass flux comparison for saturated inlet: (a) P_{P1}=355 kPa, G_{TS}=652 kg/m^2-s, $\langle\alpha_{t,P1}\rangle$ = 25.9%, (b) P_{P1}=353 kPa, G_{TS}=1177 kg/m^2-s, $\langle\alpha_{t,P1}\rangle$ = 17.4%, (c) P_{P1}=353 kPa, G_{TS}=1421 kg/m^2-s, $\langle\alpha_{t,P1}\rangle$ = 18.2%.

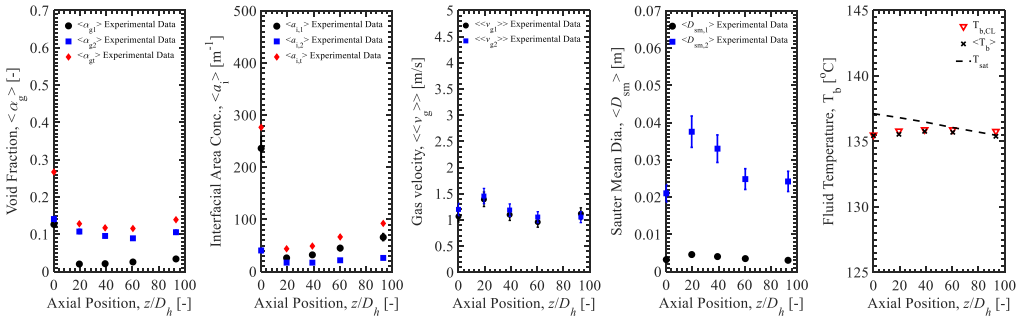

(a)

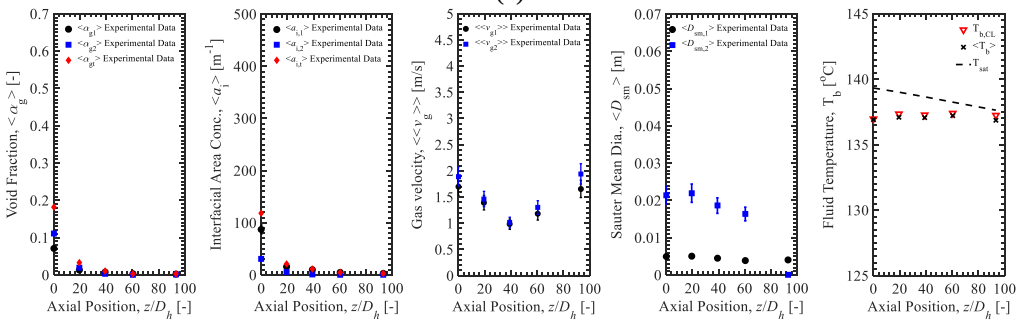

(b)

Figure 3.11 Axial measurements for inlet subcooling comparison for low system pressures: (a) P_{P1}=333 kPa, G_{TS}=948 kg/m^2-s, $<\Delta T_{sub,P1}>$=1.7 ^{o}C, $<\alpha_{t,P1}>$ = 26.7%, (b) P_{P1}=355 kPa, G_{TS}=927 kg/m^2-s, $<\Delta T_{sub,P1}>$=2.4 ^{o}C, $<\alpha_{t,P1}>$ = 18.2%.

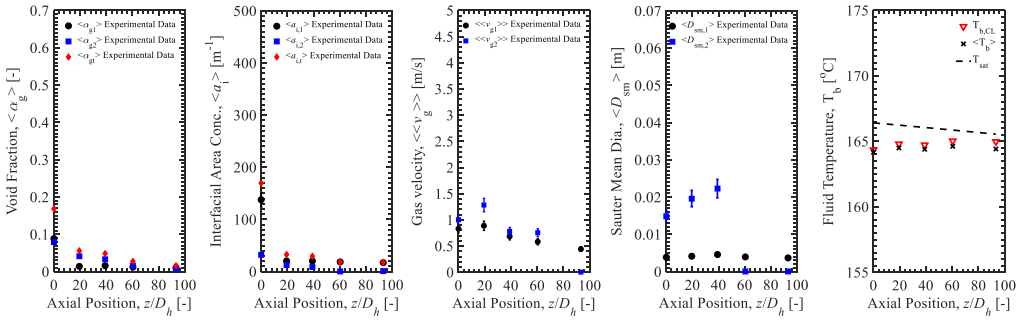

(a)

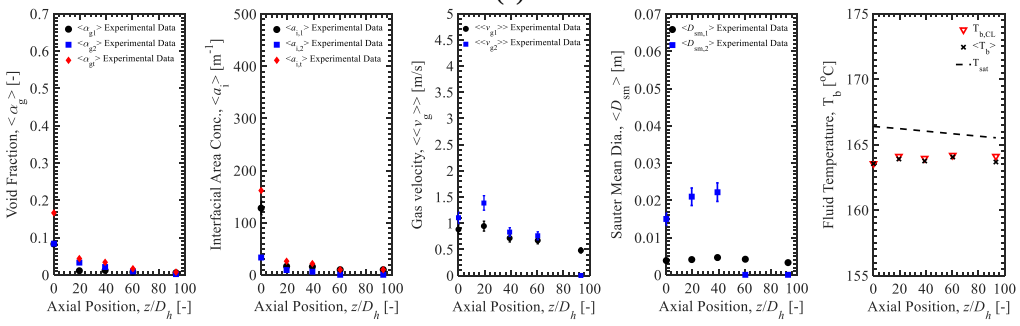

(b)

Figure 3.12 Axial measurements for inlet subcooling comparison for elevated system pressures: (a) P_{P1}=726 kPa, G_{TS}=493 kg m^{-2}s^{-1}, $\langle\Delta T_{sub,P1}\rangle$=2.2 ºC, $\langle\alpha_{t,P1}\rangle$ = 16.8%, (b) P_{P1}=726 kPa, G_{TS}=500 kg m^{-2}s^{-1}, $\langle\Delta T_{sub,P1}\rangle$=2.9 ºC, $\langle\alpha_{t,P1}\rangle$ = 16.6%.

3.5. Conclusions

Forced convection experiments of steam-water flow are carried out in a vertical annulus with a long unheated section and experimental data focusing on condensing, flashing, and saturated flow is presented. With the focus of this database being on adiabatic steam-water flow, five instrumentation ports are located in the unheated section of the test section which provide local measurements of void fraction, interfacial area concentration, gas velocity, Sauter mean diameter, using four-sensor conductivity probes apart from pressure and local liquid temperature. Local experimental data is presented for three representative conditions from the experimental database. The radial and axial profiles provide high-resolution information on the evolving two-phase flow structure in an adiabatic test section for different inlet boundary conditions. The change in local phase distribution can be used to validate local modeling of interfacial mass and momentum transfer in multidimensional simulation tools. A parametric analysis of the system parameters is also conducted using area-averaged data to study their impact on the two-phase measurements. It is observed that a small subcooling can cause rapid condensation, and similarly small superheat can cause flashing, both leading to a substantial change in void fraction. This significant dependence on a small temperature difference creates a challenge for modeling and uncertainty propagation. In conclusion, this adiabatic steam-water dataset serves to isolate the condensing and flashing phase-change phenomena and is designed to be used for validation of system codes and computational fluid dynamics codes.

CHAPTER 4. ONE-GROUP CONDENSATION MODELING

In this chapter, the condensation model of Park et al. (2007) is analyzed for the one-group IATE and validated using three available experimental datasets for condensing flows. First, the validation is performed for a decoupled calculation of IATE which assumes input of void fraction, pressure, phase velocity and liquid subcooling. The significance of the decoupled solution is to isolate the source and sink terms as well as to provide a simple model to be easily adopted into a current two-fluid model solver. As a logical extension, the condensation modeling is then analyzed in the context of a coupled simulation of IATE and void fraction transport, and the need for a two-group coupled model is highlighted. Finally, the sensitivity of important parameters is investigated to understand the condensation model and the impact on the predictions of both the interfacial area concentration and void fraction.

4.1. Benchmark of Existing IAC Correlations/Models

Figure 4.1 (a) and (b) show the ratio of simulated to experimental interfacial area concentration as a function of experimental void fraction, calculated using the interfacial area concentration correlations (listed in Table A.1) for the three experimental datasets along with the zero solid line and ±30% dashed lines. In the first approach (Figure 4.1(a)) the experimental void fraction is used for all four correlations in the calculation of interfacial area concentration, and in the second approach, the one-dimensional void transport equation is solved using the constitutive modeling summarized in Table C.1 with the interfacial area concentration correlations providing local interfacial area concentration. Three observations can be made regarding the results. First, all the four interfacial area concentration correlations have large absolute mean relative errors (according to Eq (4.1)) in the prediction of interfacial area concentration, tabulated in Table 4.2. Second, the void transport equation improves the prediction accuracy of interfacial area concentration for most of the interfacial area concentration correlations compared to the first approach. However, the void fraction prediction (not shown) is poor when deploying the void transport equation using the interfacial area concentration correlations as the interfacial area concentration prediction affects the downstream prediction of void fraction. The third observation is that, although the predictions of interfacial area concentration improve at higher void fraction, the relative mean errors are considerably large except for the correlation of Zeitoun et al. (1994). for the dataset of Zeitoun (1994) (not shown) as the interfacial area concentration correlation of Zeitoun et al. (1994) was obtained from the dataset. In summary, a more rigorous approach, such as IATE, is recommended in the prediction of interfacial area concentration.

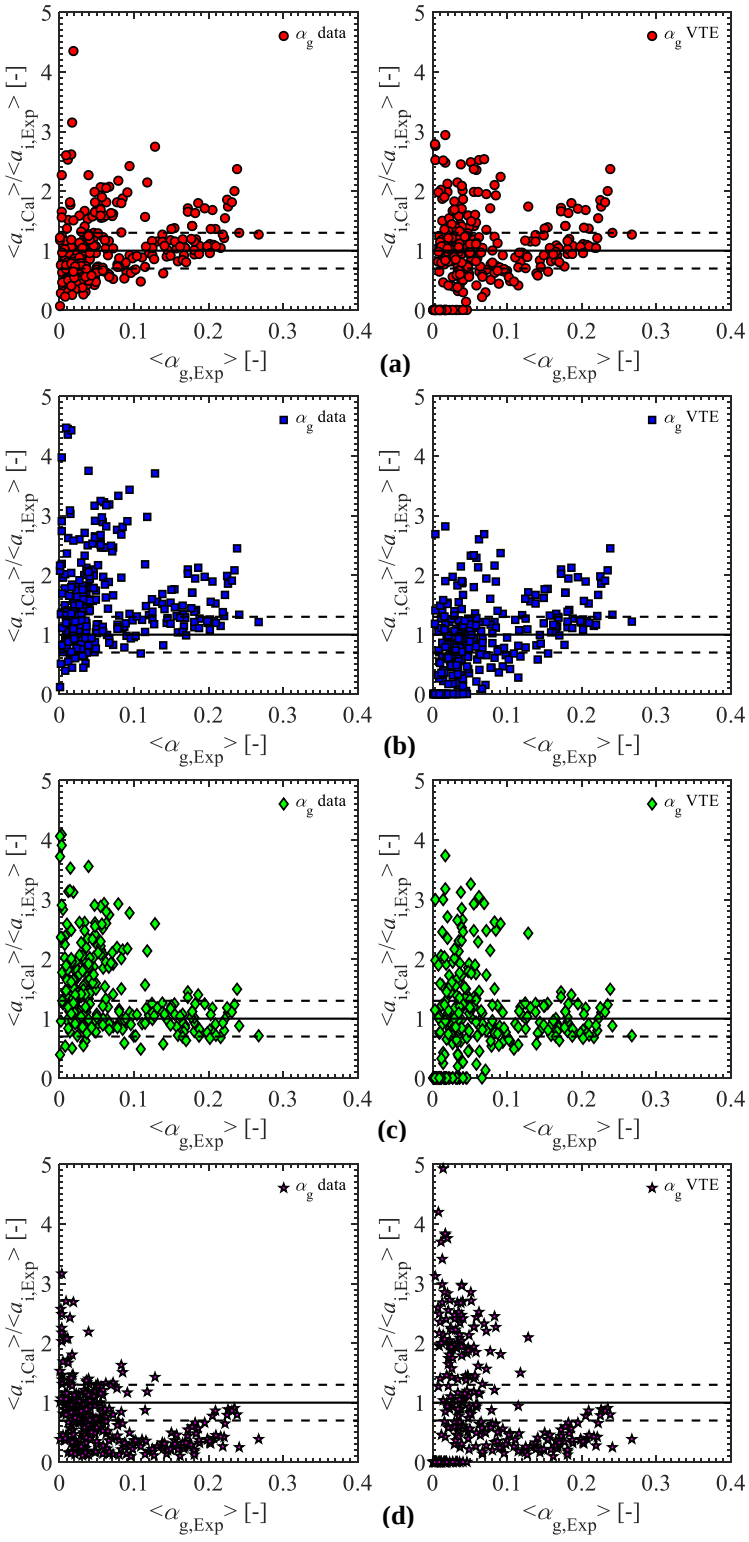

Figure 4.1 Comparison of predicted to experimental interfacial area concentration vs. experimental void fraction using void fraction data and void transport equation with experimental data of Zeitoun (1994), Ozar et al. (2013) and Kumar et al. (2019) for the following IAC correlations: (a) RELAP 5/MOD3.3, (b) TRACE V5.0, (c) Zeitoun et al. (1994), (d) Dejesus and Kawaji (1990).

$$\varepsilon_{a_i} \equiv \frac{1}{n}\sum_{j=1}^{n}\left|\frac{a_{i,Cal} - a_{i,Exp}}{a_{i,Exp}}\right|_j , \tag{4.1}$$

Table 4.1 Summary of the mean errors for IAC correlations using experimental void fraction and the void transport equation with experimental data of Zeitoun (1994), Ozar et al. (2013) and Kumar et al. (2019).

Interfacial area concentration correlation	Figure	$\varepsilon_{ai,\alpha data}$ [%]	$\varepsilon_{ai,\alpha VTE}$ [%]
RELAP 5/MOD3.3	4.1(a)	40.0	51.0
TRACE V5.0	4.1(b)	71.9	53.0
Zeitoun et al. (1994)	4.1(c)	69.6	59.9
Dejesus and Kawaji (1990)	4.1(d)	48.6	84.6

4.2. Decoupled One-group Model

The decoupled model represents a complete isolation of the IATE from the phase conservation equations. This is achieved by providing void fraction, bulk liquid temperature and pressure based on the experimental data to validate IATE. Additionally, since data is not available for the void-weighted gas velocity, «v_g», in the data of Zeitoun (1994), it is calculated using the drift flux model, summarized in Table C.1. It must be noted that the experimental data for the void-weighted gas velocity closely matches the predictions of the drift flux model, and, therefore, the drift flux model is used for all three datasets for consistency. The IATE is given in compact form in terms of sources/sinks of interfacial area concentration in Table C.1. The area-averaged condensation model of Park et al. (2007) is also summarized in Table C.1. Both the experimental test sections were discretized in the simulation domain using a mesh size of 1 mm which was determined using a mesh sensitivity analysis. The mesh sensitivity was conducted by varying the mesh size by two orders of magnitude from 1 cm to 0.1 mm for case Z-1. It was determined that 1 mm is the converged (optimum) mesh size as there was a negligible change in the solution for any further reduction in mesh size. The area-averaged IATE was discretized using a simple first-order forward-difference scheme by evaluating the sources and sinks at node i to obtain values of area-averaged interfacial area concentration, ‹a_i›, at node i+1.

Figure 4.2 shows the results of the decoupled model predictions for the data of Zeitoun (1994), Ozar et al. (2013) and Kumar et al. (2019). The cases using Zeitoun (1994) data are marked using the case number appended to ‘Z’, ‘O’ is appended to the cases using the conditions of Ozar et al. (2013), summarized in Table B.1, and ‘K’ is appended to the cases using Kumar et al. (2019) data, summarized in Table B.2. The results for the select nine cases (three from each dataset) are

plotted as the change in interfacial area concentration, Δa_i, versus the nondimensional axial distance, z/D_h, where D_h is the hydraulic diameter. The reason for plotting the results in terms of the difference between the interfacial area concentration obtained at a given location and the first measurement location is because the IATE does not calculate the interfacial area concentration but only the change from a given inlet condition. The uncertainty reported in the interfacial area concentration data is based on the recommended error reported for the respective datasets.

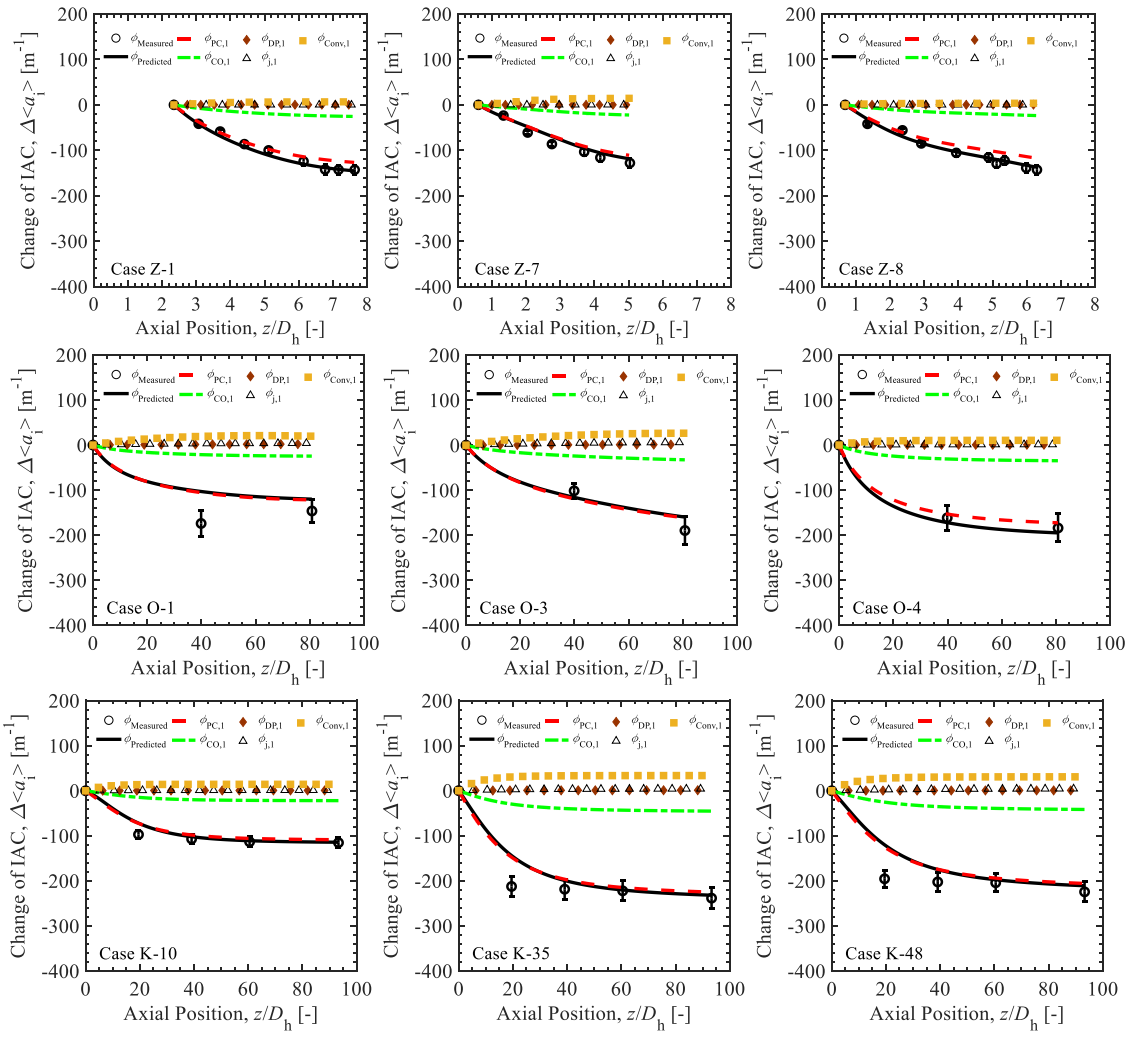

Figure 4.2 Comparison of simulated interfacial area concentration source/sink terms with select cases of Zeitoun (1994), Ozar et al. (2013) and Kumar et al. (2019) using the decoupled model.

To arrive at these results, closure of the condensation modeling of Park et al. (2007) required a dimensionless boundary diameter, β_{bc}, of 0.4 which is consistent with the recommendation of Park et al. (2007). Furthermore, the bubble Reynolds number, Re_b, used in the condensation Nusselt

number correlation of Zeitoun (1994) is based on the boundary diameter instead of the Sauter mean diameter.

The Zeitoun (1994) conditions, considered by the original validation of Park et al. (2007) (i.e. Z-6, Z-7, and Z-8), result in a 10.7% error, which is similar to the 13.2% error shown by Park et al. (2007) validation. Here, the error in prediction, ε, is calculated as the mean absolute relative error, given by,

$$\varepsilon_{\Delta a_i} \equiv \frac{1}{n}\sum_{j=1}^{n}\left|\frac{\Delta a_{i,Cal} - \Delta a_{i,Exp}}{\Delta a_{i,Exp}}\right|_j , \tag{4.2}$$

where n is the number of interfacial area concentration measurements downstream of the first measurement location. The method of predicting or specifying the gas velocity is not provided in the Park et al. (2007) benchmark, and, therefore, a direct comparison is difficult.

It is observed that the predicted change in interfacial area concentration closely matches the experimental data for the cases of Zeitoun (1994), and relatively good prediction is obtained for the cases of Ozar et al. (2013) and Kumar et al. (2019). The relative error in the database is found to be 12.1% when considering all sixty conditions (cases Z-1 to Z-8, O-1 to O-4 and K-1 to K-48). The good prediction against the Zeitoun (1994) data is expected as the Nusselt number suggested for the condensation model of Park et al. (2007) is that of Zeitoun (1994) which was developed based on these conditions. However, the extension of this modeling of Park et al. (2007) and Zeitoun (1994) to the conditions of Ozar et al. (2013) and Kumar et al. (2019) represents a significant extension in pressure and mass flux applicability. It must be noted that the resolution of the experimental data of Kumar et al. (2019) is high in comparison to the dataset of Ozar et al. (2013), and the IATE closely predicts the development of the interfacial area concentration profile as it sharply decreases from Ports 1-3 because of the inlet subcooling.

Contrary to the assumption of constant gas velocity by Park et al. (2007), the convection term, representing the effect of changing gas velocity defined by Eq. (1.31), is shown to be nonzero in the cases of Zeitoun (1994) and even significant for the high-mass-flux conditions of Kumar et al. (2019). This convection term represents the only significant source of interfacial area concentration within the condensing flow. The interaction mechanisms, consistent with other IATE validations in phase-change flows (Brooks et al., 2014; Brooks and Hibiki, 2016), are shown to be negligible. Even the high-mass-flux cases of Kumar et al. (2019) result in very small turbulent impact. The lack of influence from bubble interaction can be attributed to the relatively low void fraction which reduces the probability of interaction and the relative dominance in the phase-change

mechanisms. Expansion due to pressure change is insignificant in the Zeitoun (1994) conditions due to the small axial domain of the simulation and is negligible even at the low-pressure conditions of Kumar et al. (2019) because of the relative dominance of phase-change mechanisms. It must be emphasized that expansion due to pressure change plays an important role in flashing flow which is not modeled in the current simulation. Consistent with the findings of Park et al. (2007), the thermally controlled condensation sink term dominates the change in interfacial area concentration with a minor contribution by the inertially controlled condensation sink term.

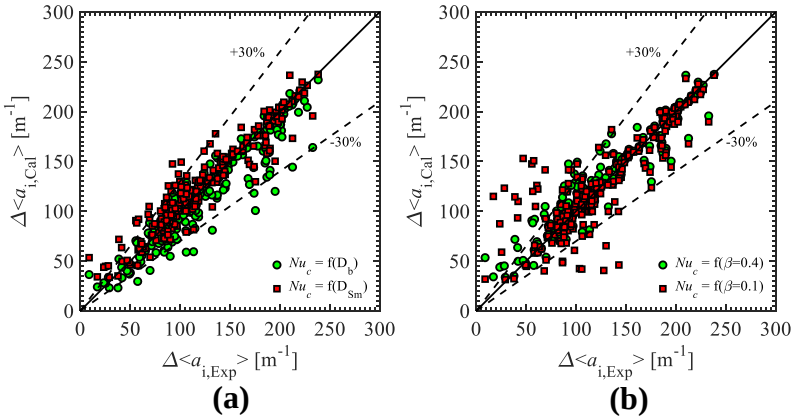

Figure 4.3: Comparison of simulated interfacial area concentration source/sink terms with experimental data of Zeitoun (1994), Ozar et al. (2013) and Kumar et al. (2019) for the decoupled model based on (a) D_{bc} vs. D_{Sm} (b) D_{Sm} (β_{bc} sensitivity)

In Figure 4.3, all the simulation data points are plotted in the plane of computed change in interfacial area concentration versus experimental change in interfacial area concentration along with the lines of zero and ±30% errors. As stated, the best prediction of the IATE, shown in Figure 4.2, requires the use of the diameter at the boundary of condensation regimes, D_{bc}, in the Reynolds number dependence of the condensation Nusselt number, which is summarized by Figure 4.3(a). It must be mentioned that the Nusselt number correlations are formulated on the bubble diameter which would be better represented by the Sauter mean diameter than the boundary diameter. Furthermore, in the modeling of Park et al. (2007), this Nusselt number dependence is required to model the thermally controlled condensation regime which by definition has a bubble diameter greater than the boundary diameter. Even though the predictions of Figure 4.3(a) show only a marginal improvement by employing the boundary diameter as against the Sauter mean diameter (mean error of 12.1% vs. 13.7%) in the condensation Nusselt number correlation, attempts to replicate the results of the IATE benchmark of Park et al. (2007) based on the Sauter mean diameter require unphysically large gas velocity values compared with the drift flux model used in this study.

Also, this overprediction in condensation cannot be compensated by the adjustable variable β_{bc} by Park et al. (2007) as shown in Figure 4.3(b) as the prediction with Sauter mean diameter is insensitive to the dimensionless boundary diameter, β_{bc}. This overprediction of condensation when using Nusselt number based on the Sauter mean diameter is consistent with the finding in subcooled boiling. In the subcooled boiling benchmark of Brooks and Hibiki (2016), an assumption of the bubble layer subcooling was imposed because of the overwhelming condensation sink term. Preliminary studies of subcooled boiling IATE show an improvement with the condensation Nusselt number based on the boundary diameter instead of the Sauter mean diameter. Although contrary to the recommendation of the original work, it is recommended here that the condensation Nusselt number correlation based on the boundary diameter is employed in the condensation model of Park et al. (2007).

The overwhelmingly dominant thermally controlled condensation mechanism indicates that the change in interfacial area concentration is predominantly due to the reduction in bubble size through condensation at the bubble interface. This mechanism is predicted by the continuity equation and artificially considered by the decoupled calculation using the void fraction data, partially represented by the first term on the right-hand side of Eq. (1.28). Therefore, even large changes to the inertially controlled condensation model will only translate to small changes in the model prediction. Similar conclusions can be extended to the analysis of Ma et al. (2015) who performed a decoupled validation. To resolve this issue along with analysis of the diameter dependence in the condensation Nusselt number, a thorough validation of the condensation model is required. The solution procedure proposed in the next section couples the void transport equation to predict the area-averaged void fraction, demonstrating a more complete prediction of uncertainty from condensation modeling.

4.3. Coupled One-group Model

The coupled void transport - IATE modeling approach, termed the ‘coupled’ model, does not require the experimental void fraction as an input unlike the decoupled model. The change in void fraction is predicted using the void transport equation, and, therefore, the thermally controlled condensation component can be calculated which is shown to be a dominant contribution to the IATE. Both the IATE and the void transport equation are simultaneously solved since the void fraction transport equation is dependent on interfacial area concentration and vice versa for the IATE. The void transport equation, given in Eq. (1.30), is expressed in compact form in terms of volume source/sink terms, which are summarized in Table C.1. All the details pertaining to

simulating the experimental data for the cases Z-1 to Z-8, O-1 to O-4 and K-1 to K-48 are the same as those of the decoupled calculation except that the void fraction data is used for comparison purposes only. A first-order forward-difference scheme is used to discretize the area-averaged void transport equation and the area-averaged IATE (Table C.1). Both the equations are solved for area-averaged void fraction, $\langle \alpha_g \rangle$, and interfacial area concentration, $\langle a_i \rangle$, at node i+1 by evaluating the sources and sinks at node i. The predictions of changes in void fraction and interfacial area concentration for nine select cases (Z-1, Z-7, Z-8, O-1, O-3, O-4, K-10, K-35, and K-48) are shown in Figure 4.4 and Figure 4.5, respectively.

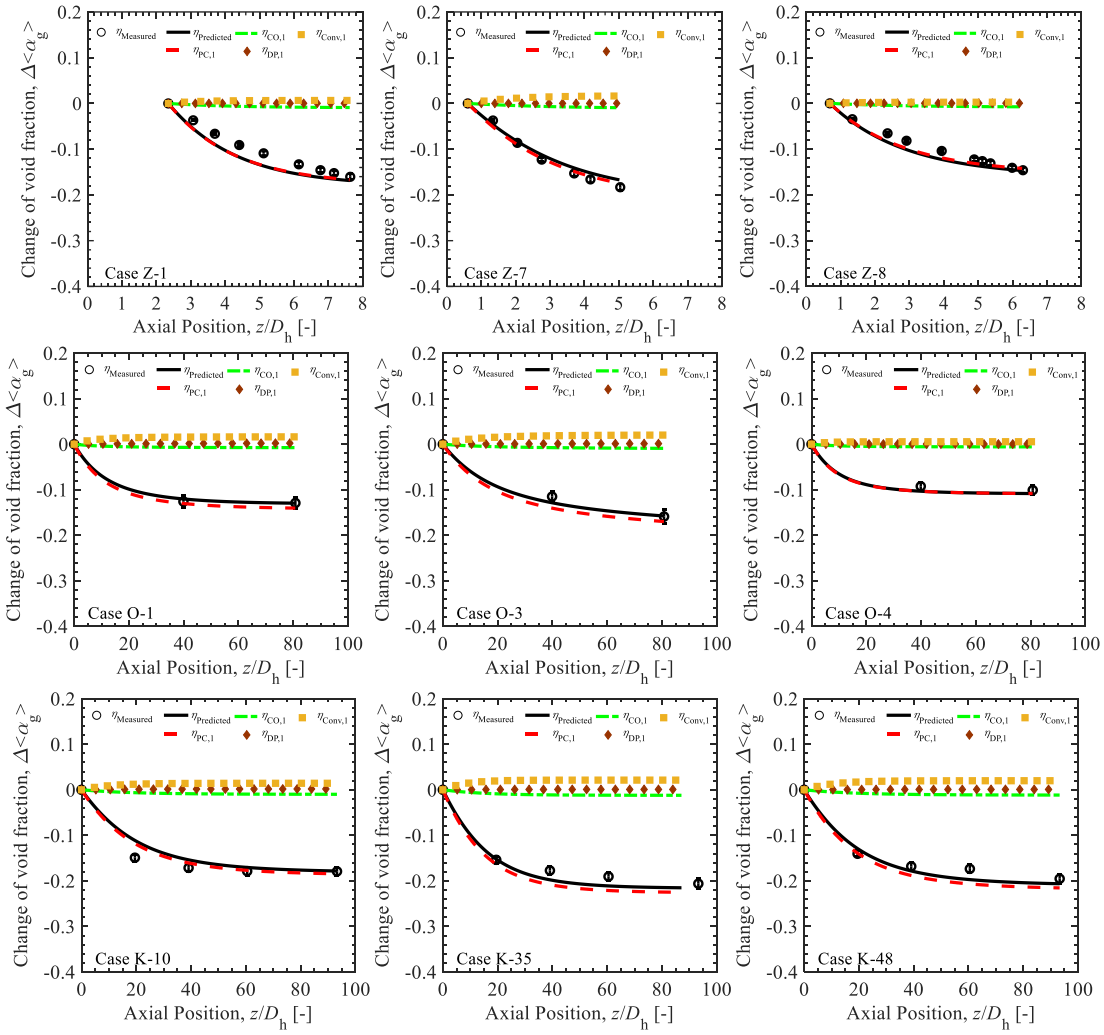

Figure 4.4 Comparison of simulated void fraction source/sink terms with select cases of Zeitoun (1994), Ozar et al. (2013) and Kumar et al. (2019) using the coupled model.

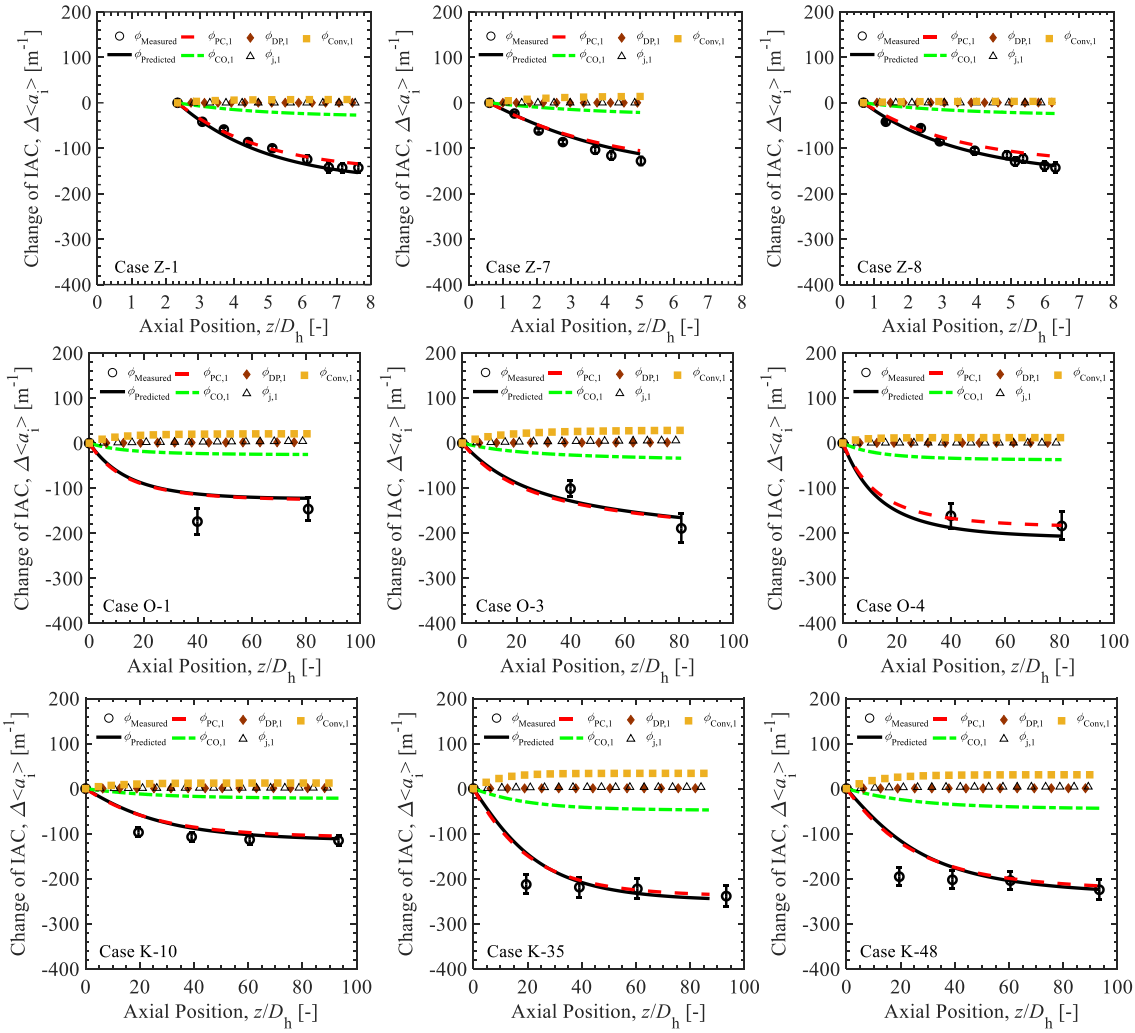

Figure 4.5 Comparison of simulated interfacial area concentration source/sink terms with select cases of Zeitoun (1994), Ozar et al. (2013) and Kumar et al. (2019) using the coupled model.

The parameters used in these simulations are as follows: the dimensionless boundary diameter is fixed at 0.4, the condensation Nusselt number correlation of Zeitoun (1994) is based on the boundary diameter, the void-weighted gas velocity is obtained from the drift flux model with a C_∞ value of 1.1, and the void-weighted drift velocity correlation corresponds to the distorted bubbly flow regime. As shown in Figure 4.4, the effect from the pressure change volume source term of the void transport equation is negligible for the same reason as in the decoupled IATE solution. The volume source from convection is the only positive contribution which is at times significant in magnitude. The relative magnitude of the volume source and sink terms highlight the dominance of the thermally controlled condensation in predicting void fraction in condensing flow. The inertially controlled condensation term is a very minor sink term. Due to the small bubble diameter definition of the inertially controlled condensation region, the collapse of these bubbles results in

a small change in void fraction. The associated interfacial area concentration prediction in the coupled solution, shown in Figure 4.5, shows a larger contribution from the inertially controlled condensation sink term than in the case of void transport. Although the collapse of a small bubble does not translate to a significant loss in volume, it does impact the bubble number density and, therefore, the interfacial area concentration. This concept is important to highlight and that is why phase-change mechanisms that result in change in bubble number density (i.e. wall nucleation and inertially controlled condensation) are given their own source term in the IATE while phase change that does not result in number density change can be grouped into the contribution from volume change. Again, as expected, the pressure change term in the IATE is nearly zero for all cases, and the contribution of convection provides a small source of interfacial area concentration change due to deceleration of the gas phase. The thermally controlled condensation sink term is again the dominant contributor to change in interfacial area concentration.

The complete impact of the condensation modeling is provided by the coupled calculation, and the importance of evaluating the model with a coupled calculation is highlighted by the comparison of Figure 4.5 to Figure 4.2. A comparison of the IATE prediction between the decoupled simulation, Figure 4.2, and the coupled simulation, Figure 4.5, shows the deception in judging the condensation modeling from the decoupled solution alone. The comparison shows that prediction in void fraction drives the prediction accuracy in the IATE for condensing flows. It is expected that the prediction accuracy of the IATE with the decoupled model, which uses the experimental void fraction, would be better than the coupled model in which the void fraction is predicted by the void transport equation. Since the prediction of void fraction has uncertainties associated with it from the net vapor generation model, this will propagate to the IATE. For the same reason, the net vapor generation term could lead to an increase in the uncertainty of the IATE if it is a dominant source/sink of interfacial area concentration. Therefore, due to the strong dependence of the net vapor generation modeling in the prediction of both the void fraction and interfacial area concentration, the coupled model is recommended for benchmarking the IATE modeling in phase-change flows.

In Figure 4.6, all the simulation data points are plotted in the plane of computed change in void fraction versus experimental change in void fraction and in the plane of computed change in interfacial area concentration versus experimental change in interfacial area concentration. Across all measurements downstream of the inlet condition, the error in void fraction prediction is 19.0% and the error in interfacial area concentration prediction is 16.6% using the boundary diameter in the Nusselt number correlation. The simulated versus experimental predictions for all conditions are shown in Figure 4.6. The corresponding mean errors for the forty-eight cases of Kumar et al.

(2019) are 17.6% and 14.2% for the void fraction and interfacial area concentration, respectively. Similarly, the corresponding errors using the Sauter mean diameter in the Nusselt number correlation for the complete database are 29.8% and 22.7% for the void fraction and interfacial area concentration, respectively.

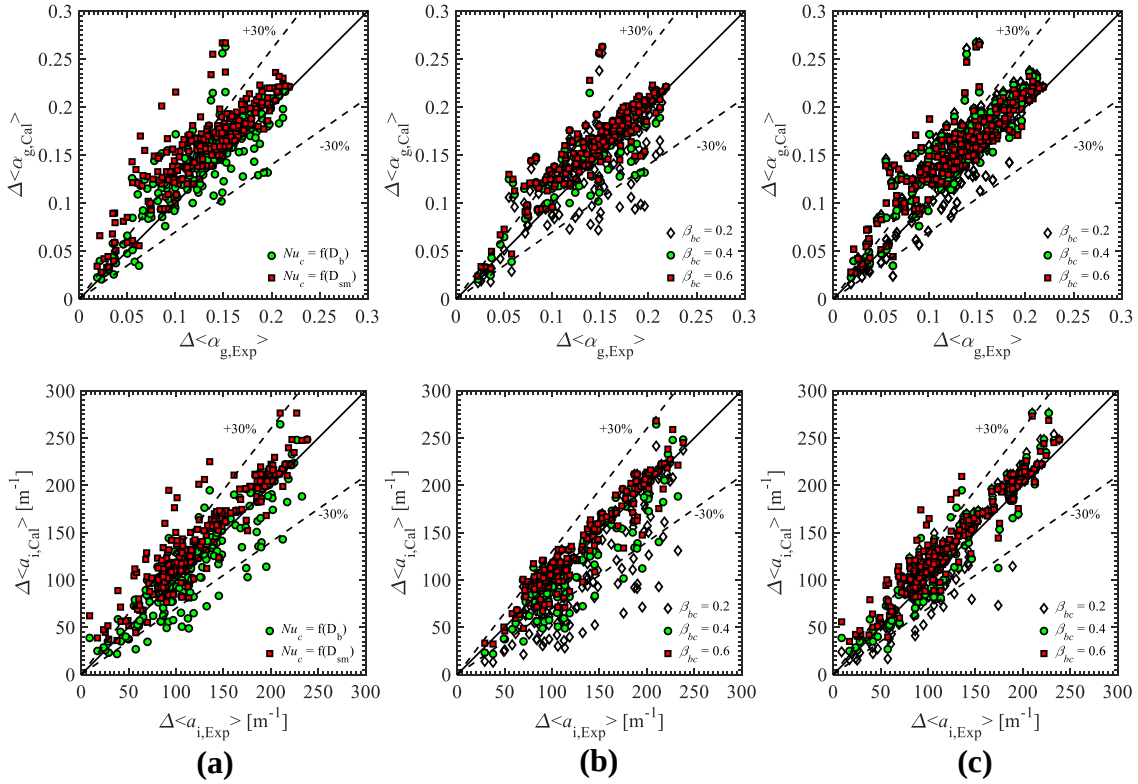

Figure 4.6 Comparison of simulated change in void fraction (top) and interfacial area concentration (bottom) with experimental data of Zeitoun (1994), Ozar et al. (2013) and Kumar et al. (2019) based on (a) D_{bc} vs. D_{Sm} (β_{bc} = 0.4) (b) D_{bc} (β_{bc} sensitivity) (c) D_{Sm} (β_{bc} sensitivity) using the coupled model.

Four observations are apparent from coupling the void fraction transport equation and the IATE from Figure 4.6. First, the overall error in the prediction of the change in void fraction is comparable to the change in interfacial area concentration. However, for some cases the void transport equation has larger error due to greater sensitivity from the Γ_g model. Again, it is worth noting the relative success of the condensation modeling at higher pressure and higher mass flux than originally considered in the model benchmark. Second, the sensitivity of the diameter used in the condensation Nusselt number correlation is greater in the coupled calculation, shown in Figure 4.6(a), than in the decoupled calculation, shown in Figure 4.3(a). The error from the void fraction prediction using the Sauter mean diameter in the condensation Nusselt number propagates to the

IATE, thus deteriorating the interfacial area concentration predictions. Significant overprediction in condensation is caused by using the Sauter mean diameter in the condensation Nusselt number. Third, as shown in Figure 4.6(b), the dimensionless boundary diameter sensitivity using the boundary diameter in the Nusselt correlation confirmed the optimum dimensionless boundary diameter, β_{bc}, of 0.4 (within the range of conditions tested) recommended by Park et al. (2007) using a much more limited set of conditions. Fourth, the condensation model with the condensation Nusselt number correlation based on the Sauter mean diameter is insensitive to the dimensionless boundary diameter as shown in Figure 4.6(c). In fact, decreasing the value degrades the void fraction and interfacial area concentration predictions which is opposite to the decoupled simulation predictions shown in Figure 4.3(b) where a marginal improvement is observed with a smaller dimensionless boundary diameter. The higher condensation rates with a smaller dimensionless boundary diameter are due to an increase in the probability of thermally controlled condensation which is a significant sink term in the IATE. At higher dimensionless boundary diameters, the probability of inertially controlled condensation increases, thereby balancing the decreased thermally controlled condensation and making the total condensation rate insensitive to the dimensionless boundary diameter. It should be emphasized that the model is sensitive to the β_{bc} value if the Nusselt number correlation is based on the boundary bubble diameter. A β_{bc} value of 0.3-0.4 predicts accurate condensation rates for the cases tested in this study. Therefore, the proper closure of the condensation model requires a moderate dimensionless boundary diameter with the condensation Nusselt number correlation based on the boundary diameter.

Figure 4.7 shows the change in void fraction and interfacial area concentration for the poor prediction of case K-12. The change in void fraction is considerably overpredicted in the case of K-12. The cause of this larger condensation term cannot be seen with this 1-group approach. Kumar et al. (2019) provides group-1 (i.e. spherical and distorted bubbles) and group-2 (i.e. cap, slug and churn-turbulent bubbles) void fraction data directly through conductivity probe measurements. When considering these bubble groups, there is a clear distinction between a two-group condition, such as case K-12 which contains ~14.1% group-2 void fraction at the inlet of the condensing region and case K-35 which is driven by condensation of group-1 bubbles and contains ~7.8% group-2 void fraction at the inlet (see Table B.2). Interfacial area concentration transport of group-1 and group-2 bubbles can vary significantly due to different bubble size, shape and velocity (Ishii and Kim, 2004) as discussed in Chapter 1. Large group-2 bubbles have small interfacial area concentration for a given void fraction, thus decreasing the condensation rate as compared to group-1 bubbles. This is not captured using a one-group approach where the combined interfacial area concentration of group-1 and group-2 bubbles results in a larger condensation rate than expected

leading to an overprediction in the change in void fraction. The change in interfacial area concentration is predicted correctly for case K-12 largely because it is driven by group-1 bubbles. It is expected that, in a fully coupled simulation where, in addition to the IATE and void transport equation, the momentum equation for the two phases along with the liquid continuity equation are all simultaneously solved, an error in the prediction of void fraction would impact the interfacial area concentration through the gas velocity.

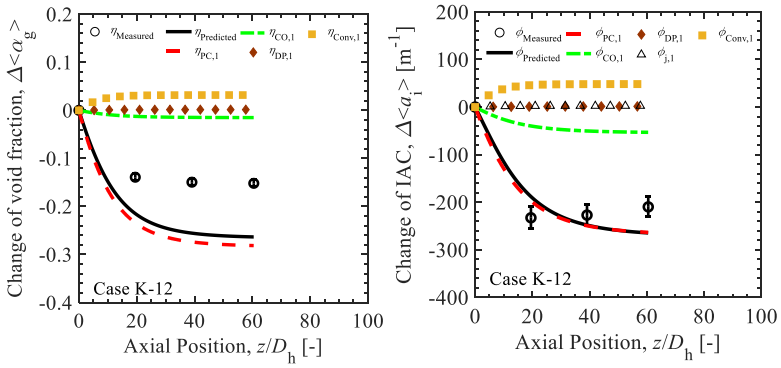

(a) **(b)**

Figure 4.7 Comparison of simulated change in (a) interfacial area concentration and (b) void fraction with the experimental condition 'K-12' using the coupled model.

Using the data of Kumar et al. (2019), a two-group condition is defined as one which has a greater than ~40% proportion of group-2 void fraction over the total void fraction at the inlet of the condensing region, defined as the 'cutoff ratio'. Figure 4.8 shows the change in simulated versus experimental void fraction and the change in predicted versus experimental interfacial area concentration for the data of Kumar et al. (2019) for two cutoff ratios. An overprediction in void fraction is clearly observed for the conditions with a higher inlet cutoff ratio. The mean errors with different inlet cutoff ratios are tabulated in Table 4.2, and it is observed that the mean error gets worse with higher cutoff ratios and beyond a cutoff ratio of ~40%, the error using a one-group approach significantly increases. It must be noted that the prediction accuracy of the one-group IATE model for case K-10 is good (shown in Figures 4.4 - 4.5) even though its inlet group-2 void fraction ratio is 0.61. A second differentiator of a two-group condition is high relative group-two void fraction throughout the condensing region, which is satisfied by case K-12 with a ~11% port-2 group-2 void fraction versus ~ 2% group-2 void fraction at port-2 for case K-10. In essence, case K-12 requires a two-group modeling effort to accurately predict the void fraction and interfacial area concentration. Bubble groups, defined by the distorted bubble limit, are not provided for the data of Zeitoun (1994). However, based on the reported inlet Sauter mean diameters, a two-group approach could improve the simulation of void fraction and interfacial area concentration in the

cases where the condensation rate is overpredicted. It must be noted that the two-group model is more complex so the benefit of adopting a two-group approach would be realized only for higher void fraction regimes as the prediction accuracy of the one-group approach might be acceptable for low-to-moderate void fraction flow regimes.

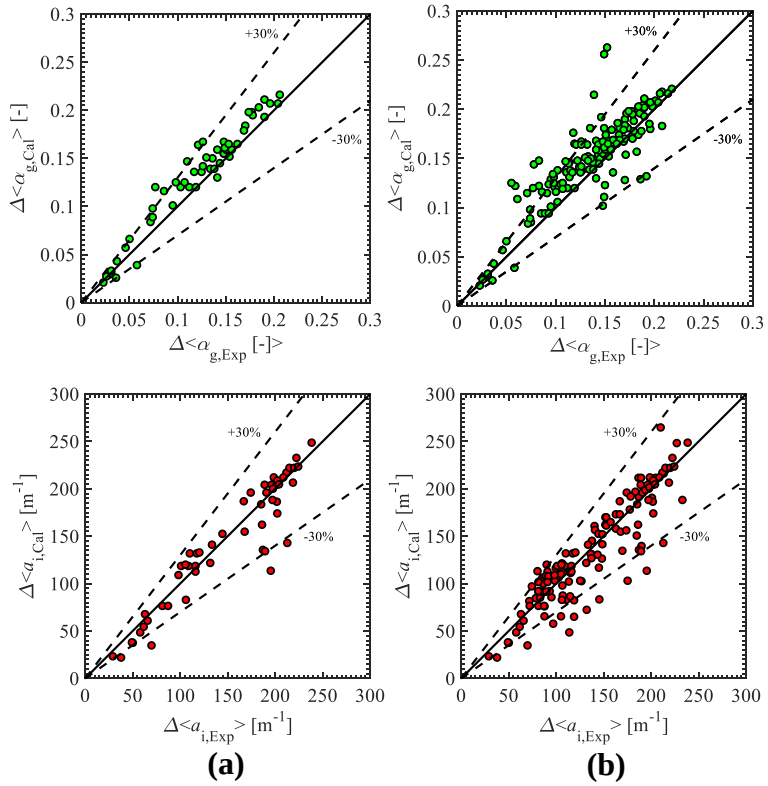

Figure 4.8 Comparison of simulated change in void fraction (top) and interfacial area concentration (bottom) with experimental data of Kumar et al. (2019) based on group-2 void fraction to total void fraction of (a) ~0.4 (b) ~0.6 using the coupled model.

Table 4.2 Summary of the mean errors for change in interfacial area concentration and change in void fraction with experimental data of Kumar et al. (2019) for varying group-2 void fraction ratio cutoffs.

$\alpha_{g,2}/\alpha_{g,t}$ **at inlet**	$\varepsilon_{\Delta\alpha}$ **[%]**	$\varepsilon_{\Delta ai}$ **[%]**
<= ~0.2	12.1	8.7
<= ~ 0.3	12.2	11.8
<= ~ 0.4	**13.2**	**11.5**
<= ~ 0.6	18.6	13.2

4.4. Sensitivity of Current One-group Model

The sensitivity of other condensation Nusselt number correlations, Nu_c, is examined in Figure 4.9 for all sixty conditions with the diameter dependence given as the boundary diameter and the Sauter mean diameter. The mean errors for the complete dataset with all the Nusselt number correlations based on the boundary diameter and the Sauter mean diameter are given in Table 4.3.

Two observations can be made from the results. First, the majority of the condensation Nusselt number correlations tested do not perform well except the Nusselt number correlation of Zeitoun (1994). Second, these correlations either show an improvement or worsen with the diameter dependence of D_{bc} versus D_{Sm}, and, therefore, no clear conclusion can be drawn. One reason for the poor performance of the majority of the Nusselt number correlations could be because these correlations were formulated for flow conditions at high Jacob numbers, and the data of Ozar et al. (2013) and Kumar et al. (2019) were taken at low Jacob numbers. However, it is observed that the majority of these correlations do not do well even for the data of Zeitoun et al. (1994) (not shown) which were taken at high Jacob numbers. It is also interesting to note that the condensation Nusselt number correlation of Zeitoun (1994) based on the boundary diameter has a good prediction accuracy across Jacob numbers and one reason could be its functional dependence on the Jacob number.

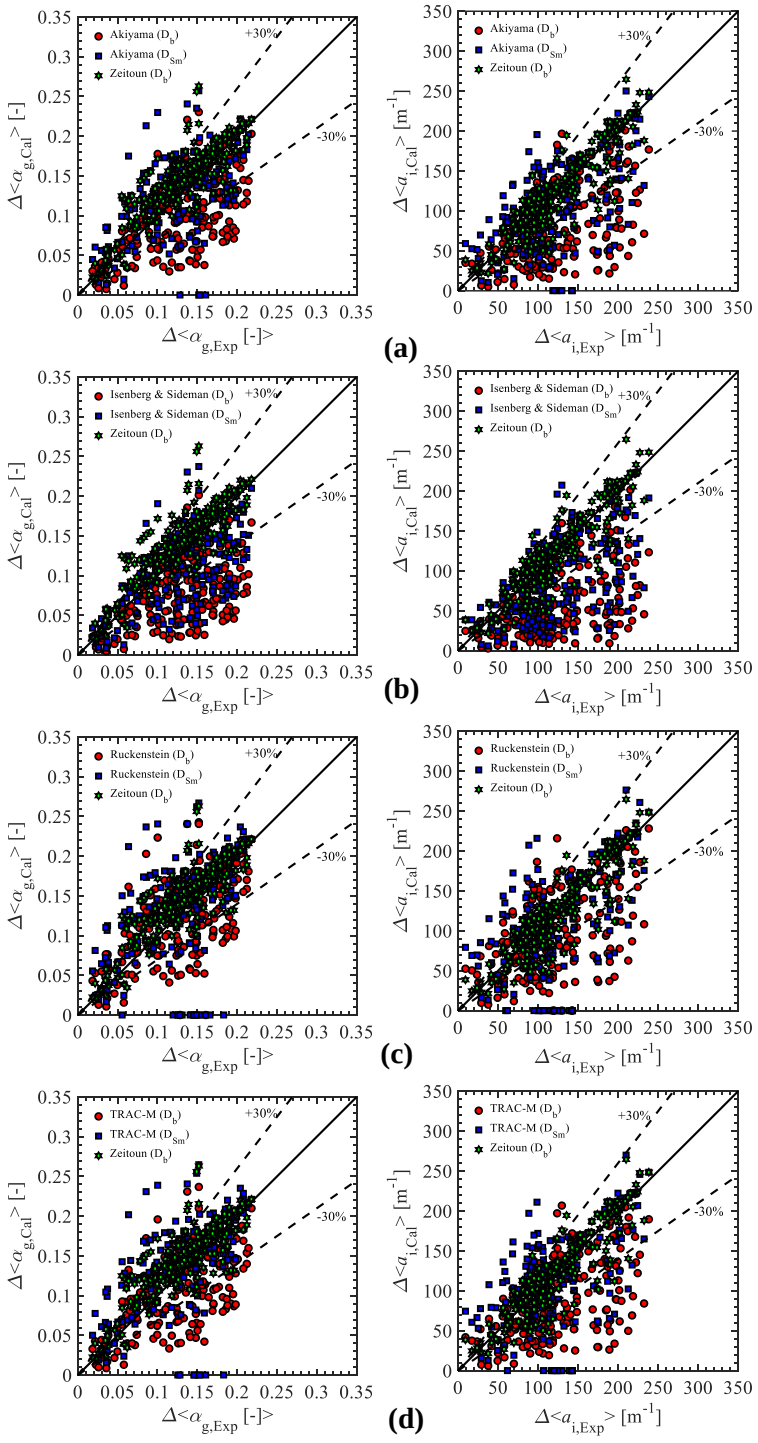

Figure 4.9 Comparison of condensation Nusselt number correlations sensitivity: (a) Akiyama (1973), (b) Isenberg & Sideman (1970), (c) Ruckenstein (1959), and (d) TRAC-M (2000) with Zeitoun (1994) using the coupled model for void fraction and interfacial area concentration source/sink terms with experimental data of Zeitoun (1994), Ozar et al. (2013) and Kumar et al. (2019).

Table 4.3 Summary of the mean errors for change in interfacial area concentration and change in void fraction with experimental data of Zeitoun (1994), Ozar et al. (2013) and Kumar et al. (2019) for various Nusselt number correlations with the Nusselt number based on D_{bc} and D_{Sm}.

Nusselt Number Correlation	D_{bc}		D_{Sm}	
	$\varepsilon_{\Delta\alpha}$ [%]	$\varepsilon_{\Delta ai}$ [%]	$\varepsilon_{\Delta\alpha}$ [%]	$\varepsilon_{\Delta ai}$ [%]
Akiyama (1973)	28.3	36.9	54.1	34.3
Isenberg and Sideman (1970)	34.8	47.3	28.7	36.0
Ruckenstein (1959)	29.8	36.2	36.6	40.3
TRAC-M/F90 (2000)	28.2	35.1	32.4	36.9

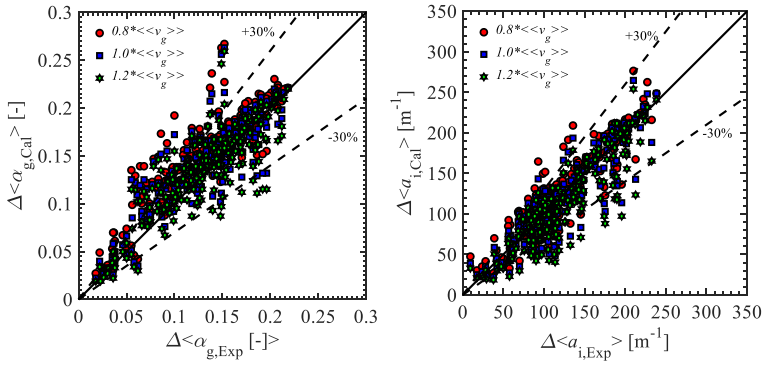

Figure 4.10 Comparison of void-weighted gas velocity sensitivity using the coupled model for (a) void fraction and (b) interfacial area concentration with experimental data of Zeitoun (1994), Ozar et al. (2013) and Kumar et al. (2019).

Lastly, the sensitivity analysis of the void-weighted gas velocity, «v_g», is carried out by changing its value at each node by ±20%, which is roughly the prediction accuracy of the drift flux model for void-weighted gas velocity under these cases (Brooks et al., 2012a; Brooks et al., 2012b) and twice the uncertainty of the experimental gas velocity of Kumar et al. (2019). The results of the sensitivity analysis with the local void-weighted gas velocity, «v_g», are shown in Figure 4.10 for the complete dataset for the change in void fraction and interfacial area concentration. These figures are important from the standpoint of benchmarking the IATE in general as one of the major assumptions in its validation process is that the gas velocity is given accurately. These figures show the impact of that assumption for the current study. Even though the source term due to convection has a small contribution towards changes in void fraction and interfacial area concentration for the default model, even a ±20% variation in the local void-weighted gas velocity is found to impact the overall results substantially, especially the void fraction whose mean error increases to 23% from the base value of 19% for a 20% decrease in the gas velocity because of the coupling of void fraction and interfacial area concentration. Gas and liquid momentum equations of the two-fluid model are necessary for a complete coupled solution. In the two-fluid model momentum equations,

the interfacial drag is primarily responsible for coupling the two phases (Brooks et al., 2012c). The drag force is proportional to the interfacial area concentration and to the square of the relative velocity, and, therefore, this sensitivity in gas velocity highlights the importance of accurate drag modeling.

4.5. Conclusions

A comprehensive benchmarking of the IATE has been performed for condensing flows and validated with three experimental datasets across a range of subcooling, pressure and mass flux. The IATE model for condensing flows is dominated by the condensation sink terms with negligible contributions from the interaction mechanisms. The condensation sink terms are divided into two different mechanisms, namely thermally controlled condensation which leads to a reduction in bubble volume at constant bubble number density and inertially controlled condensation which decreases the bubble number density through condensation-driven bubble collapse. The decoupled IATE is validated in this study with all sixty conditions extending the range of pressure and mass flux of previous benchmarks. Two findings which are consistent with the previous decoupled IATE benchmarks can be summarized as follows: a) thermally controlled condensation mechanism is the dominant sink term in change of interfacial area concentration with a minor contribution from the inertially controlled condensation sink term, and b) interaction mechanisms do not impact the change in interfacial area concentration. However, the impact of the convection source term, previously neglected, is significant at high mass flux and should not be ignored. Furthermore, it is also established that, in order to replicate the current IATE approach, the condensation Nusselt number correlation of Zeitoun (1994) should be based on the boundary diameter, D_{bc}, with a dimensionless boundary diameter, β_{bc}, of 0.4. This requirement stems from the Nusselt number correlation of Zeitoun (1994) being based on the local Sauter mean diameter, D_{sm}, whereas, in the IATE condensation modeling, the Nusselt number correlation is applied with an average Sauter mean diameter. A thorough application of the Nusselt number correlation by Zeitoun (1994) would require knowing the bubble size distribution.

In order to conduct a complete validation of the condensation modeling, simulations with coupled IATE and void transport equation were performed. The relative magnitudes of the source/sink terms of IATE remain unchanged from the decoupled calculation. In the void transport equation, the thermally controlled condensation sink term is overwhelmingly dominant. Overall, the coupled model gives corresponding mean errors of 19.0% and 16.6% in comparison to the experimental data of change in void fraction and change in interfacial area concentration,

respectively, for the complete dataset of sixty conditions. By coupling the IATE and the void transport equation, it is observed that the sensitivity of the diameter used in the Nusselt number correlation is higher than the decoupled model because the error in the void fraction prediction propagates to the IATE. A two-group approach is recommended for a ratio of group-2 void fraction to total void fraction greater than 0.4 (cutoff ratio) to improve the accuracy of the IATE and void transport modeling for conditions with large bubbles.

The sensitivity of the one-group model to condensation Nusselt number and void-weighted gas velocity is performed. Analysis of different condensation Nusselt number correlations shows that most of the correlations give poor predictions for the range of conditions tested apart from the condensation Nusselt number correlation of Zeitoun (1994). Lastly, the importance of accurate void-weighted gas velocity cannot be overstated as it weights the contribution of all mechanisms to change in void fraction and interfacial area concentration. The significant sensitivity to gas velocity highlights the need for an accurate interfacial drag force when applied within the solution of the two-fluid model.

CHAPTER 5. TWO-GROUP CONDENSATION MODELING

One of the major limitations of the one-group IATE model identified in Chapter 4, is its applicability only to bubbly flows. Therefore, as a next step, the two-group two-fluid IATE model is used to analyze gas-dispersed condensing slug flows. Past work on the inter-group mass transfer model, required for closure of the dispersed-phase conservation equations and interfacial area transport equations, has only considered the condition of expansion of group-1 bubbles to group-2 bubbles with inter-group transfer from group-2 to group-1 only through group-2 breakup. However, in condensing flows, the condensation of group-2 bubbles provide a significant source of mass and interfacial area to group-1 bubbles. Therefore, the inter-group mass transfer model is revisited in this work to derive a more general form suitable to any heat transfer and pressure change condition.

The objectives of this chapter are two-fold: first, to review the current formulation of the two-group two-fluid IATE model and rederive the equations especially the inter-group mass transfer term as its applicable for group-1 to group-2 mass transfer only and second, to expand this framework to incorporate inter-group mass transfer from group-2 to group-1 which is critical for condensing flows. A general formulation of the two-group two-fluid model is derived, and the resulting model requires a second inter-group transfer coefficient. A model is developed for the newly proposed group-2 inter-group mass transfer coefficient. The steady-state area-averaged coupled system of IATE and void transport equations is validated against the two-group condensing data taken in the test facility with the new approach to inter-group mass transfer. The proposed formulation predicts the group void fraction and interfacial area concentration with better accuracy in comparison to the one-group model with modifications to the group-2 Nusselt number correlation.

5.1. Evaluation of the Current Two-group Two-fluid Model

The IATE, as discussed in past chapters, accounts for changes in number density at constant gas volume (interaction mechanisms), changes in number density due to creation/destruction of gas volume (phase change mechanisms) and changes in gas volume at constant number density (gas expansion/contraction mechanisms). In the case of the two-group IATE, the inter-group transfer is an additional term accounting for the change in bubble group identity. Since the bubble group is based on bubble size with the boundary taken to be the maximum distorted bubble size, a bubble can change its group affiliation through interaction mechanisms, phase change mechanisms, and pressure change. Significant attention has been given to the modeling and validation of interaction mechanisms in both the one-group and two-group

formulations (Ishii and Kim, 2004). However, the studies addressing IATE in phase change flows are few, and only Ozar and colleagues (Ozar et al., 2013; Brooks et al., 2014) consider two-group IATE in conditions with phase change in their simulation of boiling flow. Furthermore, in every two-group IATE study to date, the flow field has resulted in expansion of group-1 bubbles to group-2 bubbles through pressure or phase change. Two-phase flows with inter-group transfer from group-2 to group-1 (through condensation or bubble contraction) have not been attempted, and a review of current modeling shows that this direction in inter-group mass transfer has not been considered. The current form of the two-group IATE and inter-group mass transfer is summarized in Table 5.1.

Table 5.1 Summary of existing two-group IATE modeling

Model and contributing work	**Equations**
Two-group IATE Based on: Ishii and Kim (2004) Sun et al. (2004a) Ozar (2009)	$\frac{\partial a_{i,1}}{\partial t}+\nabla\cdot\left(a_{i,1}\boldsymbol{v}_{i1}\right)=\begin{cases}\left\{\frac{2}{3}-\chi\left(\frac{D_c}{D_{Sm,1}}\right)^2\right\}\left(\frac{a_{i,1}}{\alpha_{g1}}\right)\left\{\frac{\Gamma_{g1}-\eta_{ph,1}\rho_g-\Delta\dot{m}_{12}}{\rho_g}-\frac{\alpha_{g1}}{\rho_g}\frac{D\rho_g}{dt}\right\}\\ +\sum_j\phi_{j,1}+\phi_{ph,1}\end{cases}$ $\frac{\partial a_{i,2}}{\partial t}+\nabla\cdot\left(a_{i,2}\boldsymbol{v}_{i2}\right)=\begin{cases}\kappa\left(\frac{a_{i,2}}{\alpha_{g2}}\right)\left\{\frac{\Gamma_{g2}-\eta_{ph,2}\rho_g+\Delta\dot{m}_{12}}{\rho_g}-\frac{\alpha_{g2}}{\rho_g}\frac{D\rho_g}{dt}\right\}+\\ \chi\left(\frac{D_c}{D_{Sm,1}}\right)^2\left(\frac{a_{i,1}}{\alpha_{g1}}\right)\left\{\frac{\Gamma_{g1}-\eta_{ph,1}\rho_g-\Delta\dot{m}_{12}}{\rho_g}-\frac{\alpha_{g1}}{\rho_g}\frac{D\rho_g}{Dt}\right\}+\sum_j\phi_{j,2}+\phi_{ph,2}\end{cases}$
Inter-group mass transfer Based on: Ishii and Kim (2004) Sun et al. (2004b)	$\frac{\Delta\dot{m}_{12}}{\rho_g}=\sum_j\eta_{j,12}+\chi\left(\frac{D_c}{D_{Sm,1}}\right)^3\left\{\frac{\partial\alpha_{g1}}{\partial t}+\nabla\cdot\left(\alpha_{g1}v_{g1}\right)-\eta_{ph,1}\right\}$ *Where,* $\chi=0.00444\left(\frac{\langle D_{Sm,1}\rangle}{D_c}\right)^{0.36}\langle\alpha_{g1}\rangle^{-1.35}$, $D_c=1.7W_G^{1/3}\left(\frac{\sigma}{g\Delta\rho}\right)^{1/3}$

To highlight the shortcomings of the current model, the results of the validation using the current model are presented in Figures 5.1-5.3. The figures show the comparison of the prediction with the experimental data in the simulation domain which is non-dimensionalized with the hydraulic diameter (D_h = 19.05 mm). The group-1 experimental data is plotted with solid black circles while the group-2 data is plotted using solid blue squares with the error bars denoting experimental uncertainty reported in Chapter 3. Void fraction and interfacial area concentration predictions are plotted as absolute values and in terms of the relative change with respect to the inlet boundary condition. The validation for the three cases employs the condensation Nusselt

number correlation of Zeitoun (1994) for group-1 and the Dittus-Boelter correlation for group-2. These correlations are chosen based on the calculated group-1 and group-2 bubble Reynolds numbers falling within the range of bubble Reynolds number applicability of the respective models.

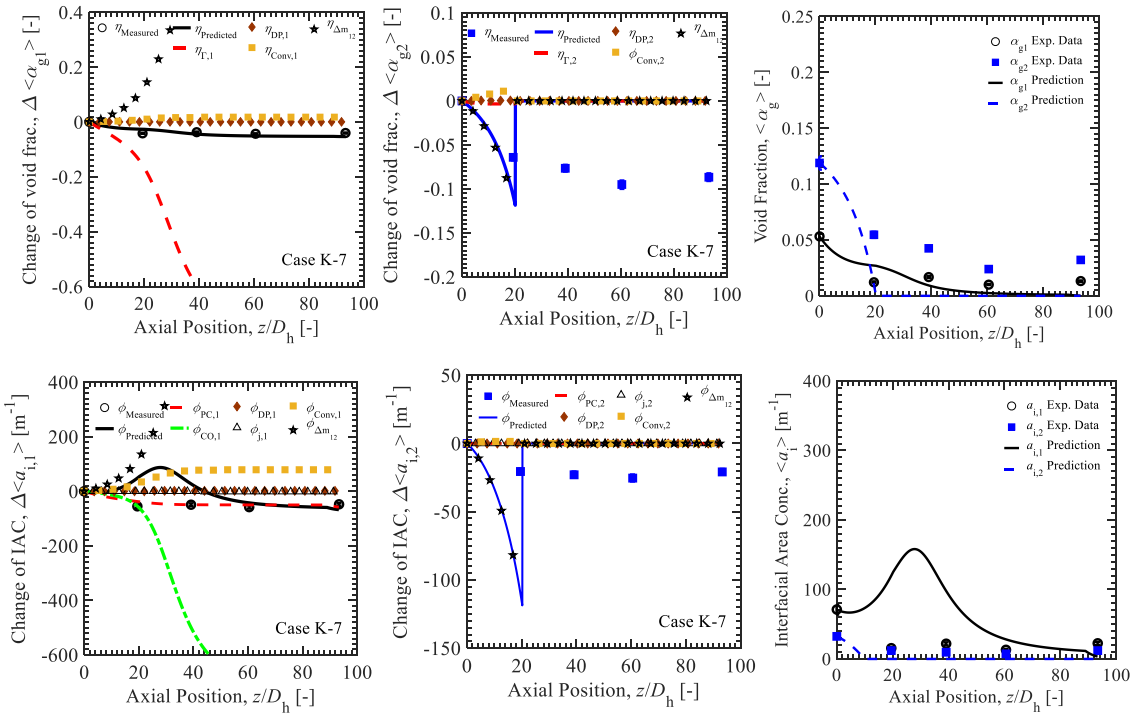

Figure 5.1: Validation of current two-group IATE formulation coupled with void transport equations for Case K-7.

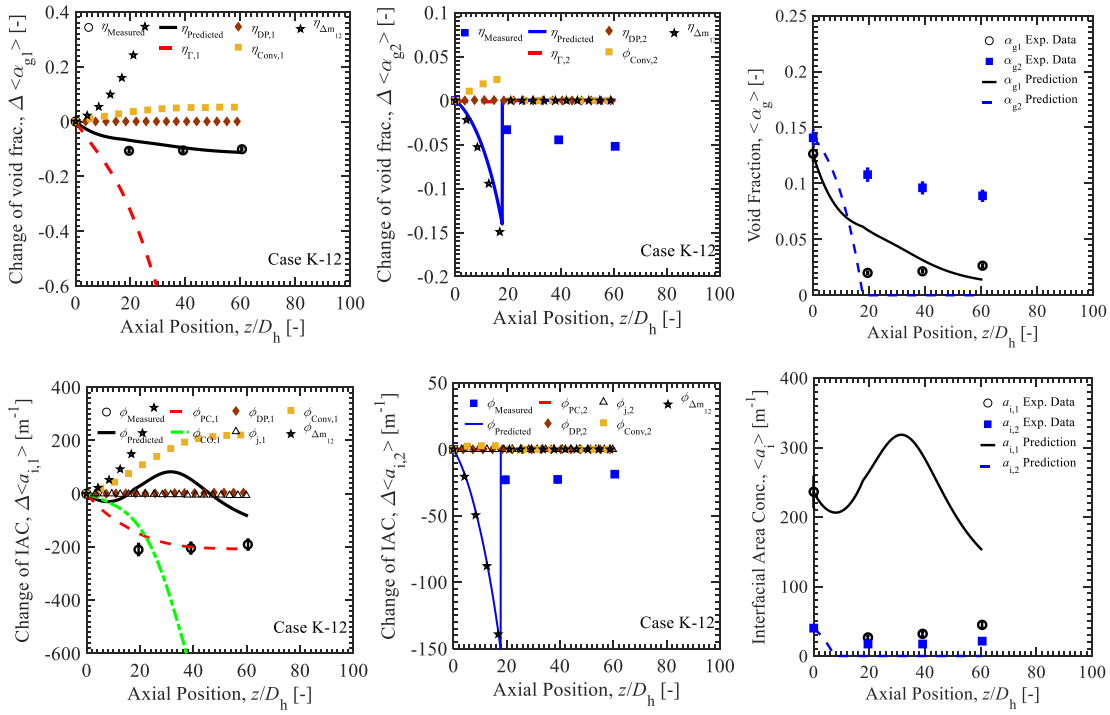

Figure 5.2: Validation of current two-group IATE formulation coupled with void transport equations for Case K-12.

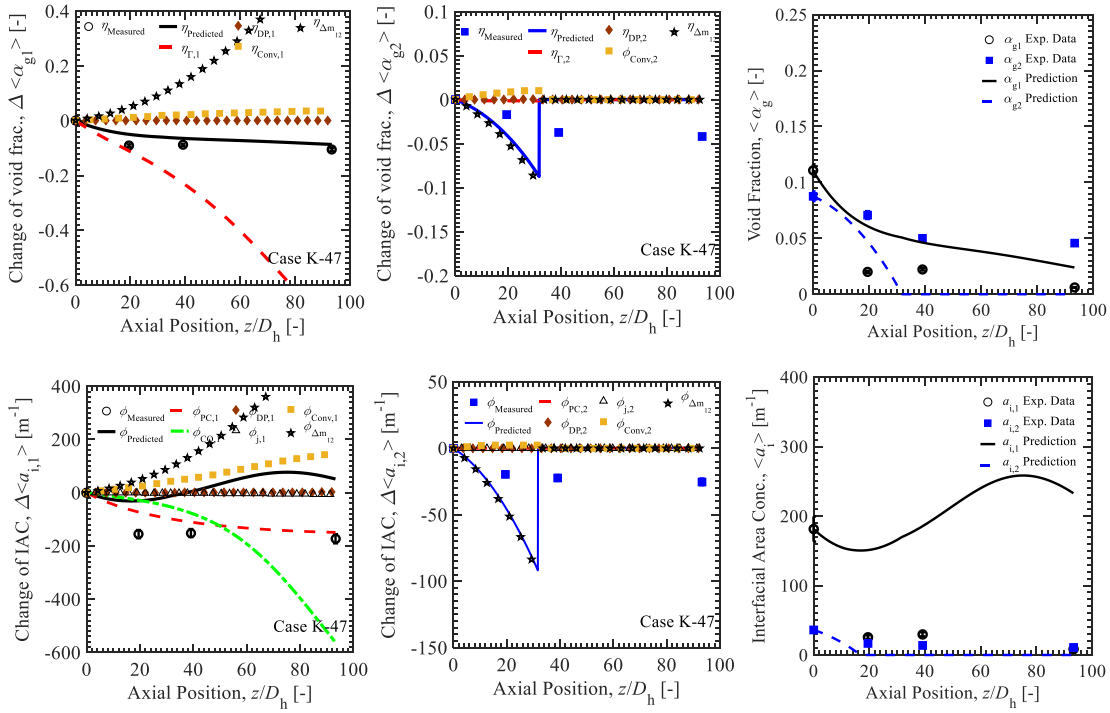

Figure 5.3: Validation of current two-group IATE formulation coupled with void transport equations for Case K-47.

The first important observation from Figures 5.1-5.3 is that the group-2 interfacial area concentration rapidly decreases. A second observation is that the predicted trend in the group-1 interfacial area concentration is largely opposite to data. A third observation is that the trend in void fraction data is correctly predicted for the bubble groups. Expanding on the first observation, the reason for rapid decrease in the group-2 interfacial area concentration is an incorrect physical process, namely the inter-group mass transfer term is driven by the condensation of group-1 bubbles. Therefore, the inter-group mass transfer term is a large sink term for group-2 interfacial area concentration causing it to rapidly decrease to zero, transforming it a one-group simulation at the downstream ports. A further consequence of the incorrectly defined inter-group mass transfer term is that it acts as a large source term for group-1 interfacial area concentration. Therefore, the change in group-1 interfacial area concentration is dependent on the relative magnitudes of the inter-group mass transfer source term and the heat transfer condensation sink term which explains the second observation. Coming to the third observation, the change in void fraction is correctly predicted for both the bubble groups despite an incorrectly modeled inter-group mass term. For group-1, the heat transfer condensation sink term is overpredicted and therefore greater than the inter-group mass transfer source term, leading to a good prediction whereas, for group-2, the inter-group mass transfer is the overwhelming dominant sink term which dictates the good prediction in the group-2 void fraction. Lastly, the expansion of group-1 to group-2 is negligible due to the high system pressure, which results in an insignificant change in gas density along the flow length. Similarly, the marginal impact of interactions mechanisms is consistent with the observations for the one-group condensing cases which were addressed in Chapter 4.

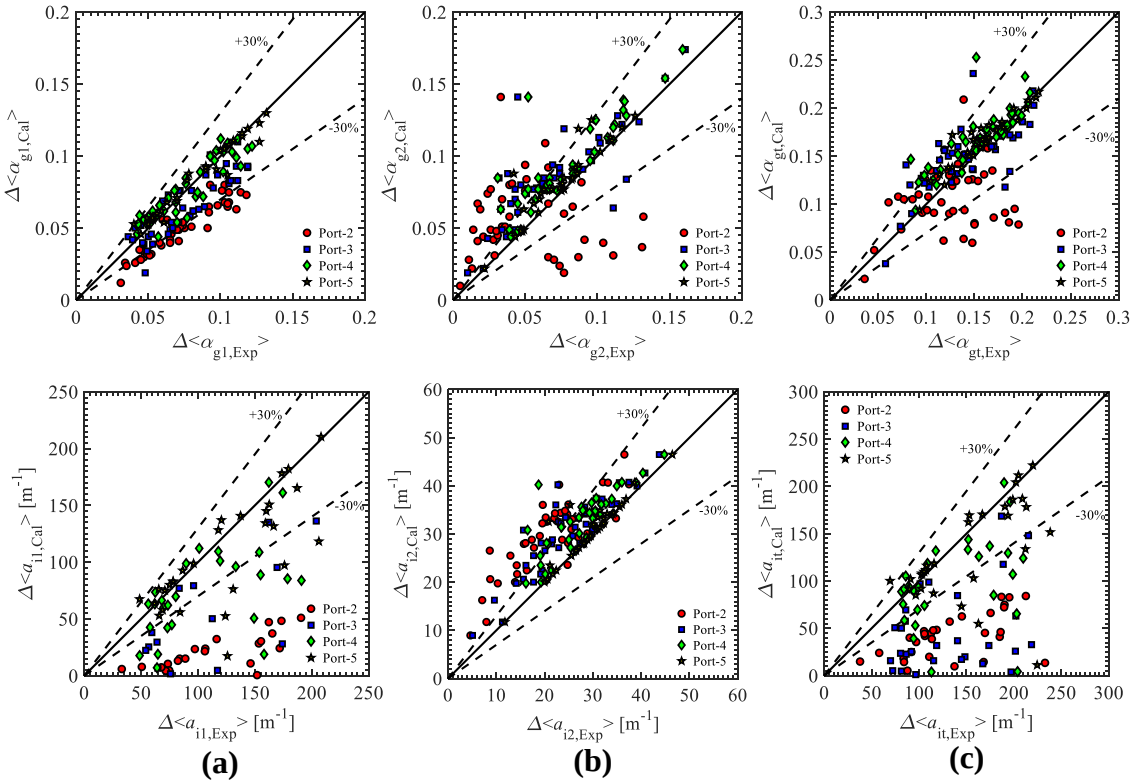

Figure 5.4 Comparison of simulated change in group void fraction (top) and group interfacial area concentration (bottom) with experimental data of Kumar et al. (2019) for (a) group-1 (b) group-2 (c) total, based on the current coupled two-group model.

The comparison of simulated change in group and total void fraction and interfacial area concentration versus experimental data of Kumar et al. (2019) (forty-five conditions) is shown in Figure 5.4. The overall summary confirms the earlier observations of under-prediction in the change in group-1 interfacial area concentration because of its opposite trend to experimental data, especially from Ports 1 to 2. The better prediction in group-2 interfacial area concentration beyond Port-2 is because of a rapid decrease in simulated group-2 interfacial area concentration to a zero value downstream of Port-2, for nearly all conditions. Void fraction predictions are better for reasons just highlighted. In a fully coupled simulation where the momentum and continuity equations are solved alongside IATE, the poor prediction in IATE would impact the gas velocity and thereby worsen the void fraction prediction. Therefore, the two-group formulation is modified for condensing flows starting from the fundamental equations.

5.2. Inter-group Mass Transfer Modeling

5.2.1. Current Inter-group Mass Transfer Modeling

To rederive the existing formulation (Table 5.1), the fundamental approach of the

Boltzmann transport equation is invoked which describes the particle transport using an integral-differential equation of the particle distribution function (Ishii and Kim, 2004). The void transport equation is obtained from the Boltzmann transport equation by multiplying it with the particle volume and integrating the resulting equation between the minimum and maximum particle volumes. For the two-group void transport equations, the limits of integration for group-1 are between the minimum bubble volume and the critical bubble volume, V_c, defined as the maximum distorted bubble limit (Ishii and Zuber, 1979), while, for group-2, the limits of integration are between the critical bubble volume and the maximum slug/cap bubble in the system, as shown by a simplified bubble distribution in Figure 5.5.

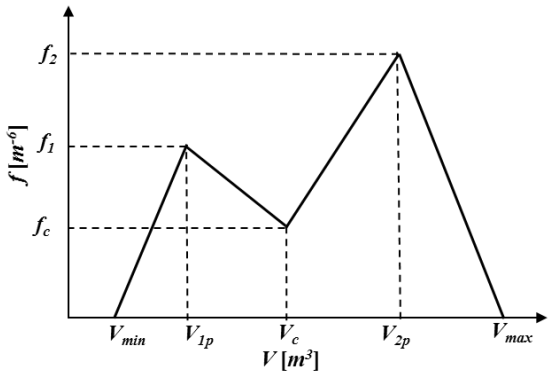

Figure 5.5: Linear approximation on the profile of fluid particle distribution function (Ishii and Kim, 2004).

The void transport equation along with the continuity equation for group-1 are used to derive the expression for the inter-group mass transfer. The void transport equation for group-1 is given as,

$$\frac{\partial \alpha_{g1}}{\partial t} + \nabla \cdot \left(\alpha_{g1} \boldsymbol{v}_{g1} \right) + \int_{V_{\min}}^{V_c} V \frac{\partial}{\partial V} \left(f \dot{V} \right) dV = \int_{V_{\min}}^{V_c} \left[\sum_j S_j + S_{ph} \right] V dV, \tag{5.1}$$

where,

$$\alpha_{g1} = \int_{V_{\min}}^{V_c} f V dV, \tag{5.2}$$

and α_g is the void fraction, V is the particle volume, the dot denotes time derivative, f is the particle distribution function, S_j is the particle source per unit mixture volume due to the j^{th} interaction

between bubbles, S_{ph} is the particle source per unit mixture volume due to phase change mechanisms, and v_g is the void-weighted gas velocity, defined as,

$$\boldsymbol{v}_{g1}\left(\boldsymbol{x},t\right)=\frac{\int_{V_{\min}}^{V_{\max}} f\left(V,\boldsymbol{x},t\right)V\boldsymbol{v}\left(V,\boldsymbol{x},t\right)dV}{\int_{V_{\min}}^{V_{\max}} f\left(V,\boldsymbol{x},t\right)VdV}. \tag{5.3}$$

The third term on the left-hand side of Eq. (5.1) accounts for the rate of change in particle volume of existing group-1 bubbles due to volume change. The rate of change in particle volume is obtained from the fundamental definition of void fraction as,

$$\frac{\dot{V}_1}{V_1}=\frac{\dot{\alpha}_{g1}-V_1\dot{n}_{b1}}{\alpha_{g1}}, \tag{5.4}$$

where n_{bn} is the bubble number density where the subscript n denotes the bubble group number. The group-1 continuity equation can also be used to obtain the rate of change in particle volume. The group-1 continuity equation is given as,

$$\frac{\partial\rho_g\alpha_{g1}}{\partial t}+\nabla\cdot\left(\rho_g\alpha_{g1}\boldsymbol{v}_{g1}\right)=\Gamma_{g1}-\Delta\dot{m}_{12}, \tag{5.5}$$

where Γ_g is the mass generation rate per unit mixture volume, $\Delta\dot{m}_{12}$ is the inter-group mass transfer rate from group-1 to group-2 per unit mixture volume and ρ_g is the gas density. Eq. (5.4) can be manipulated in the following manner,

$$\frac{1}{\alpha_{g1}}\left\{\frac{\partial\alpha_{g1}}{\partial t}+\nabla\cdot\left(\alpha_{g1}\boldsymbol{v}_{g1}\right)-\eta_{ph,1}+\Delta\dot{m}_{12}\right\}=\frac{1}{\alpha_{g1}}\left\{\frac{\Gamma_{g1}-\eta_{ph,1}\rho_g}{\rho_g}-\frac{\alpha_{g1}}{\rho_g}\frac{D\rho_g}{Dt}\right\}, \tag{5.6}$$

where,

$$\eta_{ph,1}=\int_{V_{\min}}^{V_c} S_{ph}VdV, \tag{5.7}$$

and η_{ph} is the volume source rate per unit mixture volume due to phase change mechanisms like wall nucleation which change the number density. Comparing Eqs. (5.3) and (5.5), it is observed that the rate of change of particle volume becomes,

$$\frac{\dot{V}_1}{V_1} = \frac{1}{\alpha_{g1}} \left\{ \frac{\Gamma_{g1} - \eta_{ph,1}\rho_g}{\rho_g} - \frac{\alpha_{g1}}{\rho_g} \frac{D\rho_g}{Dt} \right\}. \tag{5.8}$$

It is important to note that the volume source term ($\dot{V}/V$) is the change in gas volume at a constant number density (Eq. (5.4)). The inter-group mass transfer term decreases both the volume and number density of group-1 bubbles. Therefore, the volume source term should not include any contribution from the inter-group mass transfer term unlike the approach adopted in previous two-group IATE formulations (Ishii and Kim, 2004). Assuming the volume source term is not a function of volume (Ishii and Kim, 2004), the third term on the left-hand side of Eq. (5.1) through integration by parts as,

$$\int_{V_{\min}}^{V_c} V \frac{\partial f\dot{V}}{\partial V} dV = \frac{\dot{V}}{V} VfV \Big|_{V_{\min}}^{V_c} - \int_{V_{\min}}^{V_c} f\dot{V} dV = \left(\frac{\dot{V}}{V}\right)_c V_c f_c V_c - \left(\frac{\dot{V}}{V}\right)_1 \alpha_{g1}, \tag{5.9}$$

where f_c is the bubble distribution function at the critical bubble volume. Expressions for the properties at the critical volume must be provided. The critical volume source term is approximated as the group-1 volume source term (Ishii and Kim, 2004), considering expansion of group-1 bubbles driving the inter-group mass transfer to group-2 bubbles,

$$\left(\frac{\dot{V}}{V}\right)_c = \left(\frac{\dot{V}}{V}\right)_1. \tag{5.10}$$

The inter-group mass transfer coefficient is introduced to specify the ratio of critical bubble number density to the group-1 bubble number density,

$$\chi \equiv \frac{f_c V_c}{n_{b1}}, \tag{5.11}$$

and χ is the inter-group mass transfer coefficient. Substituting Eqs. (5.9), (5.10), and (5.11) in Eq. (5.1), it becomes,

$$\frac{\partial \alpha_{g1}}{\partial t} + \nabla \cdot \left(\alpha_{g1} \mathbf{v}_{g1} \right) - \eta_{ph,1} - \int_{V_{\min}}^{V_c} \sum_j S_j V dV = \begin{Bmatrix} \left(1 - \chi \left(\frac{D_c}{D_{Sm,1}} \right)^3 \right) \\ \left\{ \frac{\Gamma_{g1} - \eta_{ph,1} \rho_g}{\rho_g} - \frac{\alpha_{g1}}{\rho_g} \frac{D \rho_g}{Dt} \right\} \end{Bmatrix}. \tag{5.12}$$

where D_{Sm} is the Sauter mean diameter and D_c is the critical bubble diameter (Ishii and Zuber, 1979). Rearranging Eq. (5.12) and multiplying both sides with the gas density and comparing with Eq. (5.5), the inter-group mass transfer is given as,

$$\Delta \dot{m}_{12} = \rho_g \left\{ \sum_j \eta_{j,12} + \chi \left(\frac{D_c}{D_{Sm,1}} \right)^3 \left\{ \frac{\Gamma_{g1} - \eta_{ph,1} \rho_g}{\rho_g} - \frac{\alpha_{g1}}{\rho_g} \frac{D \rho_g}{Dt} \right\} \right\}, \tag{5.13}$$

where,

$$\sum_j \eta_{j,12} = \int_{V_{\min}}^{V_c} \sum_j S_j V dV, \tag{5.14}$$

and $\eta_{j,12}$ is the net volume transfer rate from group-1 bubbles to group-2 bubbles due to the j^{th} interaction between the two bubble groups. The inter-group mass term can also be expressed in an implicit form using Eq. (5.6) in terms of the change in void fraction by the following expression,

$$\Delta \dot{m}_{12} = \frac{\rho_g \left\{ \sum_j \eta_{j,12} + \chi \left(\frac{D_c}{D_{Sm,1}} \right)^3 \left\{ \frac{\partial \alpha_{g1}}{\partial t} + \nabla \cdot \left(\alpha_{g1} v_{g1} \right) - \eta_{ph,1} \right\} \right\}}{\left\{ 1 - \chi \left(\frac{D_c}{D_{Sm,1}} \right)^3 \right\}}. \tag{5.15}$$

Therefore, compared to the current inter-group mass transfer model, given in Table 5.1, the expressions converge only if,

$$\chi \left(\frac{D_c}{D_{Sm,1}} \right)^3 \ll 1. \tag{5.16}$$

This was also recently discussed by Worosz (2015). The ratio of the critical diameter to the Sauter mean diameter is always greater than one; however, the inter-group transfer coefficient can be small

as shown by the only current correlation summarized in Table 5.1. The explicit form, Eq. (5.13), is recommended due to the clear stability issues in Eq. (5.15) when this factor approaches unity.

The two-group IATE is derived using a similar approach to the void transport equation in Eq. (5.1) from the fundamental Boltzmann transport equation, by multiplying throughout with the surface area of particles of volume V, $A_i(V)$, and integrating the equation between the respective limits for the two bubble groups (Ishii and Kim, 2004). The group-1 IATE is obtained by integrating between the limits of V_c and V_{min}, given as,

$$\frac{\partial a_{i,1}}{\partial t}+\nabla\cdot\left(a_{i,1}\boldsymbol{v}_{g1}\right)+\int_{V_{\min}}^{V_c}A_i\frac{\partial f\dot{V}}{\partial V}dV=\int_{V_{\min}}^{V_c}\sum_j R_j A_i dV+\int_{V_{\min}}^{V_c}R_{ph}A_i dV, \tag{5.17}$$

where,

$$a_{i,1}=\int_{V_{\min}}^{V_c}fA_i dV, \tag{5.18}$$

$$\phi_{ph,1}=\int_{V_{\min}}^{V_c}S_{ph}A_i dV, \tag{5.19}$$

$$\phi_{j,1}=\int_{V_{\min}}^{V_c}\sum_j S_j A_i dV, \tag{5.20}$$

$$\boldsymbol{v}_{i1}\left(\boldsymbol{x},t\right)=\frac{\int_{V_{\min}}^{V_c}f\left(V,\boldsymbol{x},t\right)A_i\left(V\right)\boldsymbol{v}\left(V,\boldsymbol{x},t\right)dV}{\int_{V_{\min}}^{V_c}f\left(V,\boldsymbol{x},t\right)A_i\left(V\right)dV}, \tag{5.21}$$

and ϕ_j is the interfacial area source term due to the j^{th} inter-group and/or intra-group bubble interaction mechanism, ϕ_{ph} is the interfacial area sink term due to sources/sinks, and v_i is the interfacial velocity. The third term on the left-hand side of Eq. (5.17) represents the change in interfacial area concentration due to volume change. Adopting a similar approach to Eq. (5.9), with the assumptions in Eqs. (5.10) and (5.11), and integrating by parts, the volume change term in Eq. (5.17) can be expressed as,

$$\int_{V_{\min}}^{V_c}A_i\frac{\partial f\dot{V}}{\partial V}dV=\left(\frac{\dot{V}}{V}\right)_1\left\{\left(\frac{D_c}{D_{Sm,1}}\right)^2\chi a_{i,1}-\frac{2}{3}a_{i,1}\right\}. \tag{5.22}$$

The 2/3 factor in Eq. (5.22) comes from a spherical bubble assumption for group-1 bubbles and denotes the change in particle surface area with respect to the particle volume (Ishii and Kim, 2004). For group-2 bubbles, the approach of Ozar (2009) is used to evaluate Eq. (5.22) by introducing the group-2 shape coefficient, κ in place of the two-thirds factor which is defined as,

$$\kappa = \frac{V dA_i}{A_i dV}, \tag{5.23}$$

where V and A_i are the volume and surface area of a slug bubble in a confined channel. Substituting Eqs. (5.8) and (5.22) in Eq. (5.17), the final expression for the group-1 IATE is obtained as,

$$\frac{\partial a_{i,1}}{\partial t} + \nabla \cdot \left(a_{i,1} \boldsymbol{v}_{i1} \right) = \begin{cases} \left\{ \frac{2}{3} - \chi \left(\frac{D_c}{D_{Sm,1}} \right)^2 \right\} \left(\frac{a_{i,1}}{\alpha_{g1}} \right) \left\{ \frac{\Gamma_{g1} - \eta_{ph,1} \rho_g}{\rho_g} - \frac{\alpha_{g1}}{\rho_g} \frac{D\rho_g}{Dt} \right\} \\ + \sum_j \phi_{j,1} + \phi_{ph,1} \end{cases}. \tag{5.24}$$

The derivation of the group-2 IATE is similar to the group-1 IATE and the final expression for the group-2 IATE is given as,

$$\frac{\partial a_{i,2}}{\partial t} + \nabla \cdot \left(a_{i,2} \boldsymbol{v}_{i2} \right) = \begin{cases} \kappa \left(\frac{a_{i,2}}{\alpha_{g2}} \right) \left\{ \frac{\Gamma_{g2} - \eta_{ph,2} \rho_g}{\rho_g} - \frac{\alpha_{g2}}{\rho_g} \frac{D\rho_g}{dt} \right\} + \\ \chi \left(\frac{D_c}{D_{Sm,1}} \right)^2 \left(\frac{a_{i,1}}{\alpha_{g1}} \right) \left\{ \frac{\Gamma_{g1} - \eta_{ph,1} \rho_g}{\rho_g} - \frac{\alpha_{g1}}{\rho_g} \frac{D\rho_g}{Dt} \right\} + \sum_j \phi_{j,2} \end{cases}. \tag{5.25}$$

A critical point to note is that unlike the current formulation of the IATE (shown in Table 5.1), the inter-group transfer term is an implicit source/sink term in the IATE expressions given in Eqs. (5.24) and (5.25) because of the corrected definition of the volume source term (Eq. (5.8)).

5.2.2. New Generalized Form of Inter-group Mass Transfer

The inter-group mass transfer term as defined in Eq. (5.13), as well as the current form listed in Table 5.1, is only applicable for vertical boiling flows with inter-group mass transfer due to volume expansion allowed only from group-1 bubbles to group-2 bubbles. It is clear from the

functional form that, in condensing flows and compressing flows, the condensation and compressibility of group-1 creates more group-1 mass. Although the mass transfer direction is correct (i.e. a negative mass transfer from group-1 to group-2), the process is obviously non-physical: group-1 condensation cannot also create more group-1 mass from inter-group transfer. In reality, the creation of group-1 mass through inter-group transfer in condensing and compressing flow is due to group-2 undergoing these processes. The net effect of condensation and compressibility of group-2 bubbles will create group-1 mass through inter-group transfer. This direction of mass transfer is clearly not considered in the current inter-group transfer modeling. The current formulation does allow for mass transfer from either of the two groups due to interaction mechanisms but not volume change. It may have been assumed that group-2 bubbles will not form until the bulk reaches saturation, but available data in Figure 5.6 shows significant group-2 void fraction even while subcooled. Furthermore, channels with large flow area relative to the bubble group boundary can from group-2 bubbles within the bubble layer thickness in subcooled boiling.

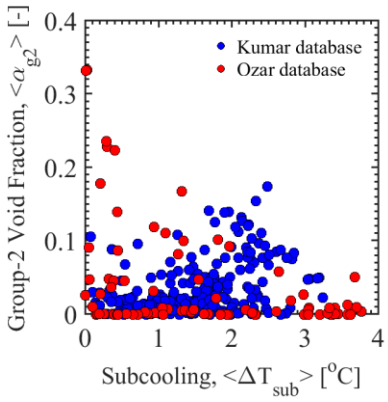

Figure 5.6 Summary of measured group-2 void fraction as a function of subcooling in the database of Kumar et al. (2019) and Ozar et al. (2013).

Therefore, to account for bidirectional inter-group mass transfer due to volume change through pressure change or phase change, it is proposed that the volume source term at the boundary in Eq. (5.10) be given as follows,

$$\left(\frac{\dot{V}}{V}\right)_c = \boldsymbol{max}\left\{0,\left(\frac{\dot{V}}{V}\right)_1\right\} + \boldsymbol{min}\left\{0,\left(\frac{\dot{V}}{V}\right)_2\right\}, \tag{5.26}$$

where *max* is the maximum function and *min* is the minimum function. This formulation is justified using the following arguments. It is important to remember that the direction of mass transfer from

group-1 to group-2 is opposite to the mass transfer from group-2 to group-1. Therefore, the volume source term contribution of group-1 bubbles is bounded in the positive domain and the volume source contribution of group-2 bubbles in the negative domain. Physically, it means that inter-group mass transfer from group-1 to group-2 is due to the net effect of volume change due to boiling/evaporation and expansion through pressure change, and inter-group mass transfer from group-2 to group-1 is the net effect of volume contraction through condensation and expansion through pressure change. This can be better understood from Figure 5.7(a) and Figure 5.7(b) which show the schematic of the two-group volume source term distributions for vertical boiling flows and condensing flows respectively.

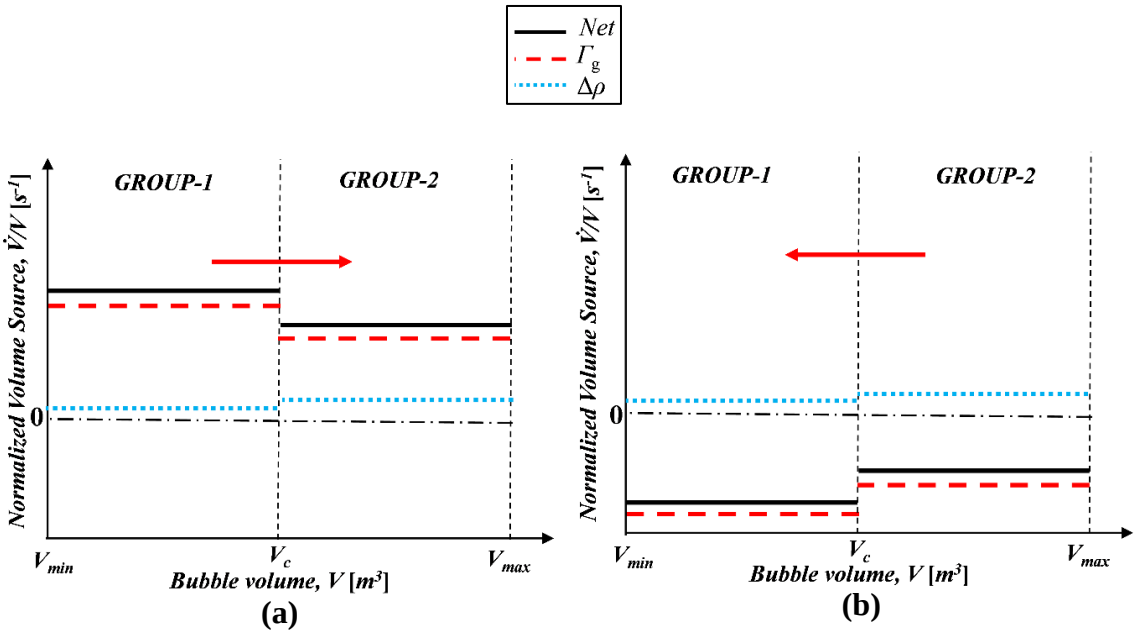

Figure 5.7: Generalized example of the two-group volume source distribution for vertical (a) boiling flows (b) condensing flows. Arrow indicates direction of net inter-group mass transfer.

A key observation from both the figures is that the volume source term is not a function of volume and is piecewise continuous within a given bubble group (Ishii and Kim, 2004). It must be noted that a multi-bubble group model with *n* bubble groups would have a total of *n*-1 discontinuities between bubble groups with a higher resolution than a two-group model. For vertical boiling flows (Figure 5.7(a)), the inter-group mass transfer is dominated by the expansion of group-1 to group-2 bubbles and is given by the first term on the R.H.S. of Eq. (5.26). Similarly, in vertical condensing flows, the inter-group mass transfer term is dominated by the condensation of group-2 to group-1 bubbles, given by the second term in the R.H.S of Eq. (5.26). It must be kept in mind that, for vertical condensing flows at nearly constant pressure, the pressure change term

only has a small positive contribution. However, in upward flows with a steep pressure gradient, the magnitude of the pressure change term could be significant. Introducing χ_1 as the inter-group mass transfer coefficient for mass transfer from group-1 to group-2, and χ_2 as the inter-group mass transfer coefficient for mass transfer from group-2 to group-1, defined as,

$$\chi_1 \equiv \frac{f_c V_c}{n_{b1}} \quad \& \quad \chi_2 \equiv \frac{f_c V_c}{n_{b2}}. \tag{5.27}$$

Using Eqs. (5.26) and (5.27) without the subscript signs, the first term in the right-hand side of Eq. (5.9) becomes,

$$\left(\frac{\dot{V}}{V}\right)_c V_c f_c V_c = \left\{ \boldsymbol{max}\left\{0, \left(\frac{\dot{V}}{V}\right)_1\right\} \alpha_{g1}\chi_1 \left(\frac{D_c}{D_{Sm,1}}\right)^3 + \boldsymbol{min}\left\{0, \left(\frac{\dot{V}}{V}\right)_2\right\} \alpha_{g2}\chi_2 \left(\frac{D_c}{D_{Sm,2}}\right)^3 \right\}, \tag{5.28}$$

With the new definition of the volume source at the boundary, the void transport equation is modified to arrive at the new inter-group mass transfer formulation. Substituting Eqs. (5.9), (5.28) in Eq. (5.1), it becomes,

$$\begin{aligned} &\frac{\partial \alpha_{g1}}{\partial t} + \nabla \cdot \left(\alpha_{g1} \boldsymbol{v}_{g1}\right) - \eta_{ph,1} - \int_{V_{\min}}^{V_c} \sum_j S_j V dV = \alpha_{g1} \frac{1}{V_1} \frac{dV_1}{dt} - \\ &\left\{ \boldsymbol{max}\left\{0, \left(\frac{\dot{V}}{V}\right)_1\right\} \left(\frac{D_c}{D_{Sm,1}}\right)^3 \frac{\alpha_{g1}\chi_1}{V_1} \frac{dV_1}{dt} + \boldsymbol{min}\left\{0, \left(\frac{\dot{V}}{V}\right)_2\right\} \left(\frac{D_c}{D_{Sm,2}}\right)^3 \frac{\alpha_{g2}\chi_2}{V_2} \frac{dV_2}{dt} \right\}. \end{aligned} \tag{5.29}$$

The definition of the volume source term for group-1 bubbles given in Eq. (5.29) is simplified in terms of different inter-group mass transfer contributions as,

$$\frac{1}{V_1} \frac{dV_1}{dt} = \frac{1}{\rho_g \alpha_{g1}} \left(\dot{m}_{\Gamma,1} + \dot{m}_{\mathrm{DP},1}\right), \tag{5.30}$$

where,

$$\dot{m}_{\Gamma,1} = \Gamma_{g1} - \eta_{ph,1}\rho_g \text{ and } \dot{m}_{\mathrm{DP},1} = -\alpha_{g1} \frac{D\rho_g}{Dt}. \tag{5.31}$$

According to Eq. (5.26), the inter-group mass transfer terms due to group-1 must be positive. Therefore, the volume change term is active only for a net positive contribution of the mass transfer

terms due to evaporation and pressure change. The group-1 void transport equation in Eq. (5.29) requires an expression for the group-2 volume source term because of the definition of the critical volume source term in Eq. (5.26). The volume source term for group-2 bubbles can be obtained by using the group-2 void transport equation. Therefore, analogous to Eq. (5.29), the group-2 void transport equation can be written as,

$$\begin{aligned}&\frac{\partial \alpha_{g2}}{\partial t}+\nabla\cdot\left(\alpha_{g2}\boldsymbol{v}_{g2}\right)-\int_{V_c}^{V_{max}}\sum_j S_j V dV=\alpha_{g2}\frac{1}{V_2}\frac{dV_2}{dt}\\&+\left\{\boldsymbol{max}\left\{0,\left(\frac{\dot{V}}{V}\right)_1\right\}\left(\frac{D_c}{D_{Sm,1}}\right)^3\frac{\alpha_{g1}\chi_1}{V_1}\frac{dV_1}{dt}+\boldsymbol{min}\left\{0,\left(\frac{\dot{V}}{V}\right)_2\right\}\left(\frac{D_c}{D_{Sm,2}}\right)^3\frac{\alpha_{g2}\chi_2}{V_2}\frac{dV_2}{dt}\right\}.\end{aligned} \tag{5.32}$$

where the limits of integration are taken from V_c to V_{max} and $\eta_{ph,2}$ is ignored as, unlike group-1, phase change mechanisms do not create or destroy group-2 bubbles directly. Therefore, the group-2 volume source comes out to be,

$$\frac{1}{V_2}\frac{dV_2}{dt}=\frac{1}{\rho_g\alpha_{g2}}\left(\dot{m}_{\Gamma,2}+\dot{m}_{\mathrm{DP},2}\right), \tag{5.33}$$

where,

$$\dot{m}_{\Gamma,1}=\Gamma_{g1}-\eta_{ph,1}\rho_g \text{ and } \dot{m}_{\mathrm{DP},1}=-\alpha_{g1}\frac{D\rho_g}{Dt}. \tag{5.34}$$

According to Eq. (5.26), the inter-group mass transfer terms due to group-2 should be negative. Therefore, the volume change term due to group-2 is active only for a net negative contribution of the mass transfer terms due to condensation and pressure change. Substituting the volume sources from Eq. (5.30) and Eq. (5.33) into Eq. (5.29), the group-1 void transport equation becomes,

$$\frac{\partial \alpha_{g1}}{\partial t}+\nabla\cdot\left(\alpha_{g1}\boldsymbol{v}_{g1}\right)-\eta_{ph,1}-\int_{V_{\min}}^{V_c}\sum_j S_j V dV=\begin{cases}\left\{\dfrac{\Gamma_{g1}-\eta_{ph,1}\rho_g}{\rho_g}-\dfrac{\alpha_{g1}}{\rho_g}\dfrac{D\rho_g}{Dt}\right\}\\-\chi_1\left(\dfrac{D_c}{D_{Sm,1}}\right)^3\boldsymbol{max}\left\{0,\dfrac{1}{\rho_g}\left(\dot{m}_{\Gamma,1}+\dot{m}_{\mathrm{DP},1}\right)\right\}\\+\chi_2\left(\dfrac{D_c}{D_{Sm,2}}\right)^3\boldsymbol{min}\left\{0,\dfrac{1}{\rho_g}\left(\dot{m}_{\Gamma,2}+\dot{m}_{\mathrm{DP},2}\right)\right\}\end{cases} \tag{5.35}$$

Rearranging Eq. (5.35) and multiplying both sides with the gas density, adopting a similar approach used in the previous subsection and comparing with Eq. (5.5) to obtain the general inter-group mass transfer term as,

$$\therefore \Delta\dot{m}_{12} = \rho_g \left\{ \sum_j \eta_{j,12} + \left\{ \begin{array}{l} \chi_1 \left(\frac{D_c}{D_{Sm,1}} \right)^3 \boldsymbol{max} \left\{ 0, \frac{\Gamma_{g1} - \eta_{ph,1}\rho_g}{\rho_g} - \frac{\alpha_{g1}}{\rho_g} \frac{D\rho_g}{Dt} \right\} \\ + \chi_2 \left(\frac{D_c}{D_{Sm,2}} \right)^3 \boldsymbol{min} \left\{ 0, \frac{\Gamma_{g2}}{\rho_g} - \frac{\alpha_{g2}}{\rho_g} \frac{D\rho_g}{Dt} \right\} \end{array} \right\} \right\}. \tag{5.36}$$

Finally, the two-group IATE is derived for phase change flows using the new definition of the boundary volume source as a sum of group-1 and group-2 mass transfers. Therefore, the volume source term in Eq. (5.22) becomes,

$$\int_{V_{\min}}^{V_c} A_i \frac{\partial f \dot{V}}{\partial V} dV = \left\{ \begin{array}{l} \boldsymbol{max} \left\{ 0, \left(\frac{\dot{V}}{V} \right)_1 \right\} \chi_1 a_{i,1} \left(\frac{D_c}{D_{Sm,1}} \right)^2 + \\ \boldsymbol{min} \left\{ 0, \left(\frac{\dot{V}}{V} \right)_2 \right\} \left(\frac{D_c}{D_{Sm,2}} \right)^2 \chi_2 a_{i,2} - \frac{2}{3} \left(\frac{\dot{V}}{V} \right)_1 \end{array} \right. . \tag{5.37}$$

Substituting Eqs. (5.30), (5.33), (5.34) and (5.35) in Eq. (5.31), the following expressions are obtained for the group-1 and group-2 IATEs,

$$\frac{\partial a_{i,1}}{\partial t} + \nabla \cdot \left(a_{i,1} \boldsymbol{v}_{i1} \right) = \left\{ \begin{array}{l} \frac{2}{3} \left(\frac{a_{i,1}}{\alpha_{g1}} \right) \left\{ \frac{\Gamma_{g1} - \eta_{ph,1}\rho_g}{\rho_g} - \frac{\alpha_{g1}}{\rho_g} \frac{D\rho_g}{Dt} \right\} \\ - \chi_1 \left(\frac{D_c}{D_{Sm,1}} \right)^2 \left(\frac{a_{i,1}}{\alpha_{g1}} \right) \boldsymbol{max} \left\{ 0, \frac{\Gamma_{g1} - \eta_{ph,1}\rho_g}{\rho_g} - \frac{\alpha_{g1}}{\rho_g} \frac{D\rho_g}{Dt} \right\} \\ - \chi_2 \left(\frac{D_c}{D_{Sm,2}} \right)^2 \left(\frac{a_{i,2}}{\alpha_{g2}} \right) \boldsymbol{min} \left\{ 0, \frac{\Gamma_{g2} - \eta_{ph,2}\rho_g}{\rho_g} - \frac{\alpha_{g2}}{\rho_g} \frac{D\rho_g}{Dt} \right\} \\ + \sum_j \phi_{j,1} + \phi_{ph,1} \end{array} \right. , \tag{5.38}$$

$$\frac{\partial a_{i,2}}{\partial t}+\nabla\cdot\left(a_{i,2}\boldsymbol{v}_{i2}\right)=\begin{cases}\kappa\left(\dfrac{a_{i,2}}{\alpha_{g2}}\right)\left\{\dfrac{\Gamma_{g2}-\eta_{ph,2}\rho_g}{\rho_g}-\dfrac{\alpha_{g2}}{\rho_g}\dfrac{D\rho_g}{Dt}\right\}\\ +\chi_1\left(\dfrac{D_c}{D_{Sm,1}}\right)^2\left(\dfrac{a_{i,1}}{\alpha_{g1}}\right)\boldsymbol{max}\left\{0,\dfrac{\Gamma_{g1}-\eta_{ph,1}\rho_g}{\rho_g}-\dfrac{\alpha_{g1}}{\rho_g}\dfrac{D\rho_g}{Dt}\right\}\\ +\chi_2\left(\dfrac{D_c}{D_{Sm,2}}\right)^2\left(\dfrac{a_{i,2}}{\alpha_{g2}}\right)\boldsymbol{min}\left\{0,\dfrac{\Gamma_{g2}-\eta_{ph,2}\rho_g}{\rho_g}-\dfrac{\alpha_{g2}}{\rho_g}\dfrac{D\rho_g}{Dt}\right\}\\ +\sum_j\phi_{j,2}+\phi_{ph,2}\end{cases}. \tag{5.39}$$

It should be noted that, for most applications, phase change effects do not create or destroy group-2 bubbles directly and, therefore, $\eta_{ph,2}$ can be neglected (Ishii and Kim, 2004).

5.2.3. Inter-group Mass Transfer Coefficients

A simple linear approximation of the fluid particle distribution can be used (Figure 5.5) similar to previous analysis (Ishii and Kim, 2004) to get general expressions for the inter-group transfer coefficients (Eq. (5.26)), given by,

$$\begin{aligned} n_{b1}&=\frac{1}{2}f_1\left(V_c-V_{\min}\right)+\frac{1}{2}f_c\left(V_c-V_{1p}\right),\\ \therefore\ \chi_1&=\left(\frac{2}{1-\xi}-\frac{V_c}{n_{b1}\left(1-\xi_1\right)}f_1\right),V_{\min}<<V_c\end{aligned} \tag{5.40}$$

$$\begin{aligned} n_{b2}&=\frac{1}{2}f_2\left(V_{\max}-V_c\right)+\frac{1}{2}f_c\left(V_{2p}-V_c\right),\\ \therefore\ \chi_2&=\left(\frac{2}{\xi_2-1}-\frac{\left(V_{\max}-V_c\right)}{n_{b2}\left(\xi_2-1\right)}f_2\right)\end{aligned} \tag{5.41}$$

where,

$$\xi_1=\frac{V_{1p}}{V_c}, \tag{5.42}$$

$$\xi_2=\frac{V_{2p}}{V_c}, \tag{5.43}$$

and ξ_m is the ratio of the maximum bubble volume in group-m to the critical bubble volume. To estimate the bounds for the inter-group transfer coefficients from Eq. (5.40) and (5.41), three

limiting fluid particle distributions are chosen (Figure 3.2), following the approach of Ishii and Kim (2004).

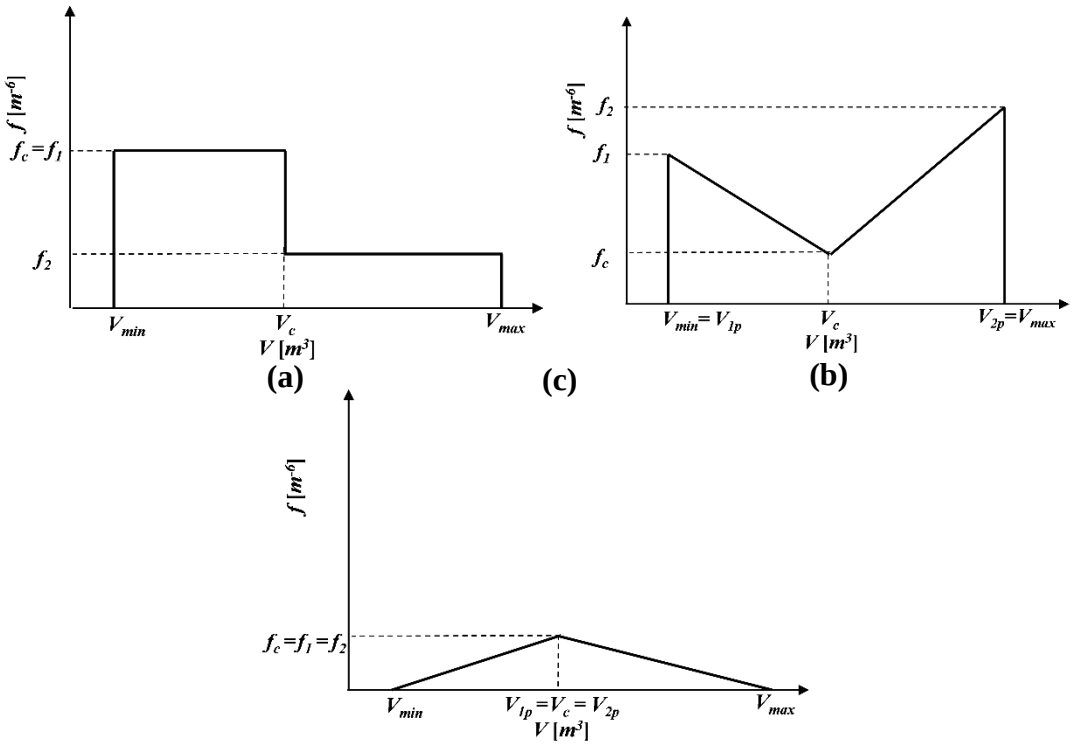

Figure 5.8: Limiting conditions for fluid particle distribution (a) Case 1 (b) Case 2 (c) Case 3 (Ishii and Kim, 2004).

The expressions for the inter-group transfer coefficients for the three cases are given as,

$$\begin{aligned}&\text{Case 1: } f = f_c = \text{constant},\ f = f_2 = \text{constant},\\ &n_{b1} = f_c\left(V_c - V_{\min}\right), n_{b2} = f_2 V_c\left(\xi_2 - 1\right),\\ &\therefore \chi_1 = 1,\ \chi_2 = \frac{1}{\xi_2 - 1}\left(\frac{f_c}{f_2}\right),\end{aligned} \tag{5.44}$$

$$\begin{aligned}&\text{Case 2: } V_{1p} = V_{\min}, V_{2p} = V_{\max}\\ &n_{b1} = \frac{1}{2}\left(f_2 + f_c\right)\left(V_c - V_{\min}\right), n_{b2} = \frac{1}{2}\left(f_2 + f_c\right)\left(V_{\max} - V_c\right),\\ &\therefore \chi_1 = \left(2 - \frac{V_c f_1}{n_{b1}}\right),\ \chi_2 = \left(2 - \frac{f_2 V_c\left(\xi_2 - 1\right)}{n_{b2}}\right),\end{aligned} \tag{5.45}$$

$$\text{Case 3: } f_1 = f_2 = f_c,\ V_{1p} = V_{2p} = V_c$$
$$n_{b1} = \frac{1}{2} f_c \left(V_c - V_{\min}\right), n_{b2} = \frac{1}{2} f_c \left(V_{\max} - V_c\right), \tag{5.46}$$
$$\therefore \chi_1 = 2,\ \chi_2 = \frac{2}{\xi_2 - 1}.$$

From Eqs. (5.44), (5.45) and (5.46), it can be easily deduced that the bounds for group-1 to group-2 transfer coefficient, χ_1 are between zero and two as obtained previously (Ishii and Kim, 2004). On the other hand, the bounds for group-2 to group-1 transfer coefficient, χ_2 are dependent on the ratio of the maximum cap/slug bubble volume to the critical bubble volume, ξ_2. Considering Case 3, if ξ_2 is allowed to approach one, it is seen that the value of χ_2 can become very large. ξ_2 approaches one when the group-2 Sauter mean diameter approaches the critical diameter like in a condensing flow. A similar conclusion can be drawn from Eq. (5.27) when the group-2 number density becomes very small resulting in large χ_2 values.

The closure of the inter-group transfer coefficients is critical for the application of the two-group IATE model in phase change flows as the inter-group transfer coefficient signifies the proportion of mass transfer between the two groups due to expansion and compressibility. Assuming the validity of the χ_1 correlation for phase change flows, the group-2 to group-1 transfer coefficient can be expressed in terms of the group-1 to group-2 transfer coefficient as,

$$\chi_2 = \frac{f_c V_c}{n_{b2}} = \chi_1 \frac{n_{b1}}{n_{b2}}. \tag{5.47}$$

It must be emphasized that the implicit assumption in Eq. (5.47) is that the fluid particle distribution is continuous across the boundary, such as in Figure 5.5. An accurate description of the fluid particle distribution is challenging for any two-phase flow and is dependent on the flow regime, but there is no reason that the bubble size distribution should be discontinuous at the critical volume for gas-dispersed two-phase flows. The group-1 to group-2 transfer coefficient can be expressed as a function of the following parameters,

$$\chi_1 = \frac{f_c V_c}{n_{b1}} = f\left(D_c, D_{Sm,1}, \alpha_{g1}\right), \tag{5.48}$$

Sun et al. (2004b) estimated χ_1 by determining the bubble number frequency distribution of spherical group-1 bubbles correlated to the bubble chord length using conductivity probe

measurements taken in atmospheric air-water flows under varying flow rates. The final correlation reviewed in Table 5.1 is a function of two first-order geometrical parameters: the Sauter mean diameter and void fraction. Conductivity probe measurements of boiling data taken in the current annulus facility with the measurement ports located in the heated region were used to propose a new χ_1 correlation by my colleagues (Zhu et al., 2019 - Listed in Table C.2), fit to the Nukiyama-Tanasawa bubble size distribution function. The newly proposed correlation for χ_1 is an improvement over the correlation of Sun et al. (2004b) as it is benchmarked with phase-change data and, additionally, the form of the new correlation ensures that the inter-group mass transfer coefficients asymptotically go to zero as χ_1 and/or group-2 number density tend to zero, as shown in Figure 5.9 for Case K-8.

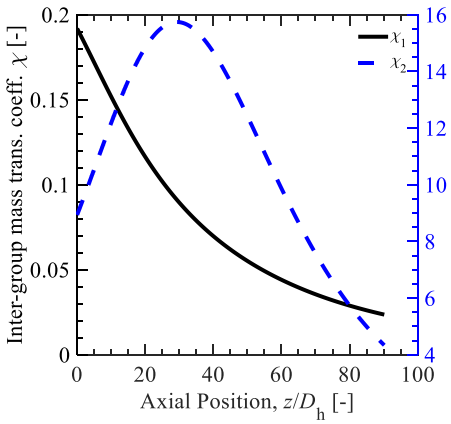

Figure 5.9 Proposed two-group IATE formulation showing inter-group mass transfer coefficients for Case K-8.

The final form of the proposed two-group model for void transport, inter-group mass transfer and interfacial area transport are summarized as,

$$\frac{\partial \alpha_{g1}}{\partial t} + \nabla \cdot \left(\alpha_{g1} \boldsymbol{v}_{g1} \right) = \left\{ \frac{\Gamma_{g1} - \Delta \dot{m}_{12}}{\rho_g} - \frac{\alpha_{g1}}{\rho_g} \frac{D\rho_g}{Dt} \right\}, \tag{5.49}$$

$$\frac{\partial \alpha_{g2}}{\partial t} + \nabla \cdot \left(\alpha_{g1} \boldsymbol{v}_{g2} \right) = \left\{ \frac{\Gamma_{g2} + \Delta \dot{m}_{12}}{\rho_g} - \frac{\alpha_{g2}}{\rho_g} \frac{D\rho_g}{Dt} \right\}, \tag{5.50}$$

$$\Delta\dot{m}_{12} = \rho_g \left\{ \sum_j \eta_{j,12} + \left\{ \begin{array}{l} \chi_1 \left(\frac{D_c}{D_{Sm,1}} \right)^3 \textbf{\textit{max}} \left\{ 0, \frac{\Gamma_{g1} - \eta_{ph,1}\rho_g}{\rho_g} - \frac{\alpha_{g1}}{\rho_g} \frac{D\rho_g}{Dt} \right\} + \\ \chi_2 \left(\frac{D_c}{D_{Sm,2}} \right)^3 \textbf{\textit{min}} \left\{ 0, \frac{\Gamma_{g2} - \eta_{ph,2}\rho_g}{\rho_g} - \frac{\alpha_{g2}}{\rho_g} \frac{D\rho_g}{Dt} \right\} \end{array} \right\}, \tag{5.36}$$

$$\frac{\partial a_{i,1}}{\partial t} + \nabla \cdot \left(a_{i,1} \boldsymbol{v}_{i1} \right) = \left\{ \begin{array}{l} \frac{2}{3} \left(\frac{a_{i,1}}{\alpha_{g1}} \right) \left\{ \frac{\Gamma_{g1} - \eta_{ph,1}\rho_g}{\rho_g} - \frac{\alpha_{g1}}{\rho_g} \frac{D\rho_g}{Dt} \right\} \\ -\chi_1 \left(\frac{D_c}{D_{Sm,1}} \right)^2 \left(\frac{a_{i,1}}{\alpha_{g1}} \right) \textbf{\textit{max}} \left\{ 0, \frac{\Gamma_{g1} - \eta_{ph,1}\rho_g}{\rho_g} - \frac{\alpha_{g1}}{\rho_g} \frac{D\rho_g}{Dt} \right\} \\ -\chi_2 \left(\frac{D_c}{D_{Sm,2}} \right)^2 \left(\frac{a_{i,2}}{\alpha_{g2}} \right) \textbf{\textit{min}} \left\{ 0, \frac{\Gamma_{g2} - \eta_{ph,2}\rho_g}{\rho_g} - \frac{\alpha_{g2}}{\rho_g} \frac{D\rho_g}{Dt} \right\} \\ + \sum_j \phi_{j,1} + \phi_{ph,1} \end{array} \right., \tag{5.38}$$

$$\frac{\partial a_{i,2}}{\partial t} + \nabla \cdot \left(a_{i,2} \boldsymbol{v}_{i2} \right) = \left\{ \begin{array}{l} \kappa \left(\frac{a_{i,2}}{\alpha_{g2}} \right) \left\{ \frac{\Gamma_{g2} - \eta_{ph,2}\rho_g}{\rho_g} - \frac{\alpha_{g2}}{\rho_g} \frac{D\rho_g}{Dt} \right\} \\ +\chi_1 \left(\frac{D_c}{D_{Sm,1}} \right)^2 \left(\frac{a_{i,1}}{\alpha_{g1}} \right) \textbf{\textit{max}} \left\{ 0, \frac{\Gamma_{g1} - \eta_{ph,1}\rho_g}{\rho_g} - \frac{\alpha_{g1}}{\rho_g} \frac{D\rho_g}{Dt} \right\} \\ +\chi_2 \left(\frac{D_c}{D_{Sm,2}} \right)^2 \left(\frac{a_{i,2}}{\alpha_{g2}} \right) \textbf{\textit{min}} \left\{ 0, \frac{\Gamma_{g2} - \eta_{ph,2}\rho_g}{\rho_g} - \frac{\alpha_{g2}}{\rho_g} \frac{D\rho_g}{Dt} \right\} \\ + \sum_j \phi_{j,2} + \phi_{ph,2} \end{array} \right. . \tag{5.39}$$

5.2.4. Modification to the Group-2 Nusselt Number Correlation

The condensation model proposed by Park et al. (2007), discussed in Chapter 2, is used in the current analysis. Additionally, for the present analysis, the one-group condensation model of Park et al. (2007) is extended to two groups considering thermally controlled condensation for both the bubble groups while inertially controlled condensation is applied only for group-1 bubbles. The bubble Reynolds number in the condensation Nusselt number correlations are based on the boundary diameter (β_{bc}=0.4) for group-1 and Sauter mean diameter for group-2. For condensing flows, the net vapor generation for group-1 and group-2 are given as,

$$\Gamma_{g1} = \rho_g \eta_{CO,1} + \rho_g \eta_{PC,1}, \tag{5.51}$$

and

$$\Gamma_{g2} = \rho_g \eta_{PC,2}. \tag{5.52}$$

Here it is acknowledged that the boundary between bubble groups is larger than the boundary between the inertially controlled and thermally controlled condensation therefore, group-2 cannot undergo inertially controlled condensation, resulting in $\eta_{ph,2}$ and $\eta_{CO,2}$ being zero. Using the Nusselt number correlations of Zeitoun and Dittus-Boelter for group-1 and group-2 respectively, it was observed that the condensation of group-2 bubbles was severely underpredicted. Sensitivity analysis on parameters like the boundary conditions, inter-group mass transfer coefficients, gas velocity, etc. did not sufficiently improve the results. It was observed that the lack of group-2 interfacial area concentration relative to the void fraction resulted in an under-prediction of group-2 condensation. It was proposed to use a more appropriate heat transfer length scale in order to increase the condensation rate for group-2 bubbles. For group-1 bubbles, the Sauter mean diameter is a representative length scale, but for group-2 cap/slug bubbles, the Sauter mean diameter can have a large magnitude and therefore dampen the condensation rate. For interfacial heat transfer of group-2 bubbles, codes like RELAP5 (reviewed in Fullmer et al. (2016)) and TRACE employ a length scale which is a function of the pipe hydraulic diameter. Based on a similar approach, it is proposed that the thickness of the liquid film, L_c, is an appropriate length scale for heat transfer of group-2 bubbles. Since the liquid film thickness is often much smaller than the Sauter mean diameter, the heat transfer coefficient is correspondingly much higher, similar to thin film evaporation. Furthermore, Kosky (1968) and Garimella et al. (2016) investigated the approach of using the liquid film thickness as an appropriate length scale for heat transfer of group-2 bubbles, ignoring the contribution of the cap end of the Taylor bubble, and obtained good results in comparison to experimental data. The condensation volume sink term due to thermally controlled condensation, $\eta_{PC,2}$, is rederived in the following manner. The energy balance around a condensing group-2 bubble is given by,

$$\dot{m}_g h_{fg} = h_c A_{b2} \left(T_{sat} - T_f \right). \tag{5.53}$$

The left-hand side of Eq. (5.53) can be expanded as the following,

$$-\rho_g \frac{dV_{b2}}{dt} h_{fg} = h_{c2} A_{b2} \left(T_{sat} - T_f \right). \tag{5.54}$$

The right-hand side of Eq. (5.54) can be rewritten as,

$$\frac{dV_{b2}}{dt} = -\frac{h_{c2}}{k_f} A_{b2}.Ja.\alpha_t. \tag{5.55}$$

Eq. (5.53) can be substituted into the definition of the volume change term due to thermally controlled condensation, given in Eq. (2.5), to obtain the following,

$$\eta_{PC,2} = n_{b2} \frac{dV_{b2}}{dt} = -n_{b2} \cdot \frac{h_{c2}}{k_f} A_{b2} \cdot Ja.\alpha_t, \tag{5.56}$$

where,

$$h_{c2} = k_f \frac{Nu_{c2}}{L_c}. \tag{5.57}$$

By performing a sensitivity analysis of the coupled two-group IATE model (described in the next section) for the database of Kumar et al. (2019), it was observed that the group-2 condensation heat transfer is sensitive to the heat transfer length scale. Table 5.2 shows the summary of the mean errors in total simulated change in void fraction and interfacial area concentration for a range of heat transfer length scale, L_c. The group-2 condensation sink terms are significantly under-predicted using the default choice of Sauter mean diameter as the heat transfer length scale, and improved results are obtained by basing L_c on the channel gap width, W_G. For a smaller L_c based on the channel gap width, the condensation is over predicted whereas, for larger length scales, L_c starts to approach the group-2 Sauter mean diameter. From the current analysis, it is determined that a liquid film thickness of 25% of the channel gap width (liquid fills ~ 50% of the gap width) is an optimum length scale for heat transfer of group-2 bubbles. Therefore, the liquid film thickness for the current analysis is defined (Eq. (5.56)) as the minimum of the Sauter mean diameter and 25% of the gap width. It must be noted that the chosen group-2 heat transfer length scale is close to the mean length scale predicted by the correlation employed in RELAP5/MOD3.3 for the database of Kumar et al. (2019).

$$L_c = \min\left(0.25G, D_{Sm,2}\right). \tag{5.58}$$

Table 5.2 Summary of mean errors in simulated change in void fraction and interfacial area concentration in comparison with experimental data of Kumar et al. (2019) for varying L_c.

$\mathbf{L_c}$	$\boldsymbol{\varepsilon_{\Delta\alpha,t}}$ **[%]**	$\boldsymbol{\varepsilon_{\Delta ai,t}}$ **[%]**
$D_{Sm,g2}$	30.8	18.9
$0.10W_G$	24.9	18.5
$0.20W_G$	15.7	13.3
$0.25W_G$	**16.2**	**13.2**
$0.35W_G$	18.6	15.4
$0.5(1-\sqrt{\alpha_{gt}})W_G$	18.7	13.9

5.3. Results and Discussion of Proposed Model

Forty-five two-group condensing flow conditions from the database of Kumar et al. (2019) (from a total of forty-eight conditions) are considered for the two-group validation study, listed in Table B.2. The validation of the two-group IATE is performed for a one-dimensional description of the flow, necessitating the area-averaged set of equations. Due to the strong interdependence of the IATE and mass conservation equations in condensing flows, the validation is performed for a coupled calculation of the void transport equations and IATE of both the bubble groups. The final set of equations for the proposed two-group IATE model are given by Eqs. (5.49), (5.50), (5.36), (5.38), (5.39). The final proposed governing equations and their closure are summarized in Table C.2. It is important to note that measured pressure and bulk liquid temperature are used in the calculation to decouple the simulation from the energy and momentum conservation equations, similar to the one-group coupled validation, discussed in Chapter 4. Additionally, the group-1 and group-2 void-weighted gas velocities are provided from the two-group drift-flux model, to be consistent with the one-group IATE calculations in the previous chapter. The void-weighted drift velocity correlations correspond to the distorted bubbly flow regime and slug flow regime for group-1 and group-2 respectively (Brooks et al., 2012a). The two-group void transport equations and IATE are solved using a first-order forward finite difference scheme with a mesh size of 1 mm, similar to the one-group IATE calculations.

The results of the validation using the proposed model are presented in Figures 5.9-5.11 for three chosen cases from the criterion established in Chapter 4 to be identified as two-group condensing conditions: Case K-7, Case K-12, and Case K-47. The plots show the change in group void fraction and interfacial area concentration and the local void fraction and local interfacial area concentration magnitudes alongside experimental measurements. Simulated inter-group mass

transfer coefficients and inter-group mass transfer change for Case K-12 is shown in Figure 5.13. Finally, the one-group and two-group IATE model predictions of total void fraction and total interfacial area concentration are shown in Figure 5.14 for Case K-7, Case K-12 and Case K-47.

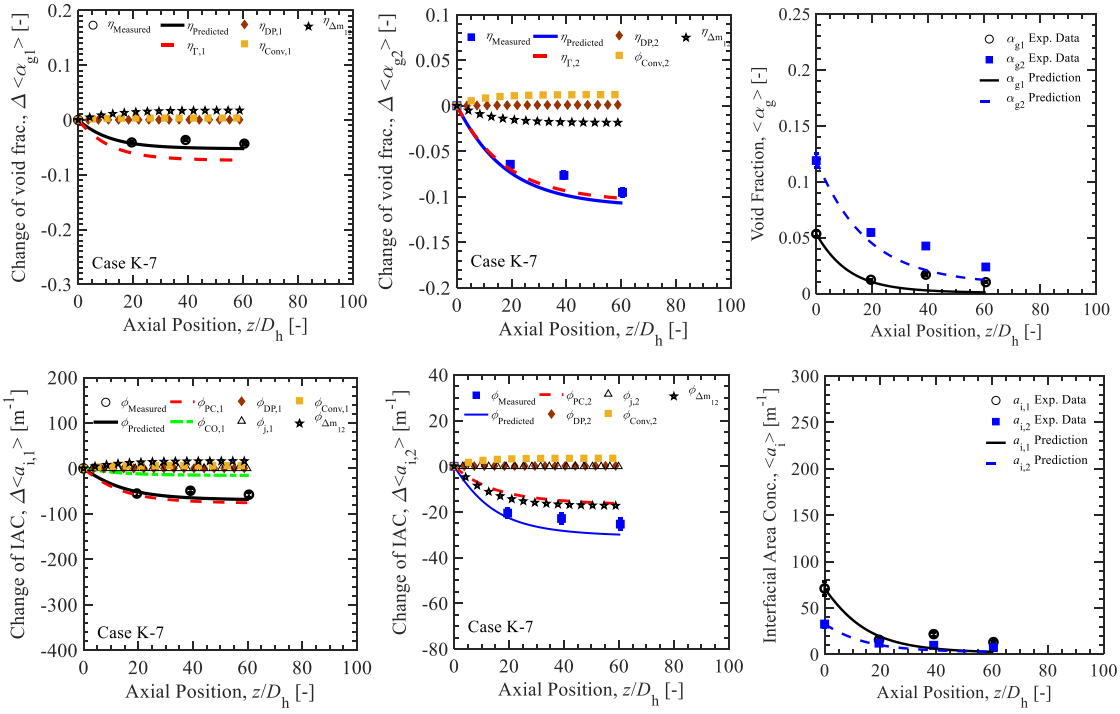

Figure 5.10: Validation of proposed two-group IATE formulation coupled with void transport equations for Case K-7.

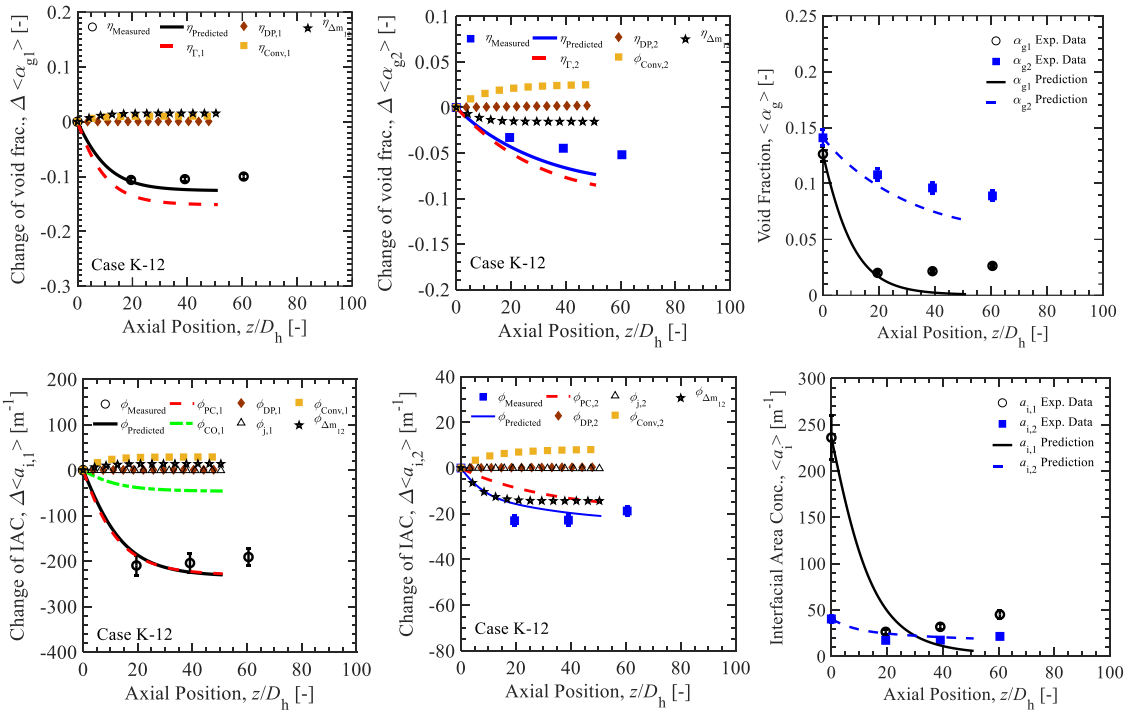

Figure 5.11: Validation of proposed two-group IATE formulation coupled with void transport equations for Case K-12.

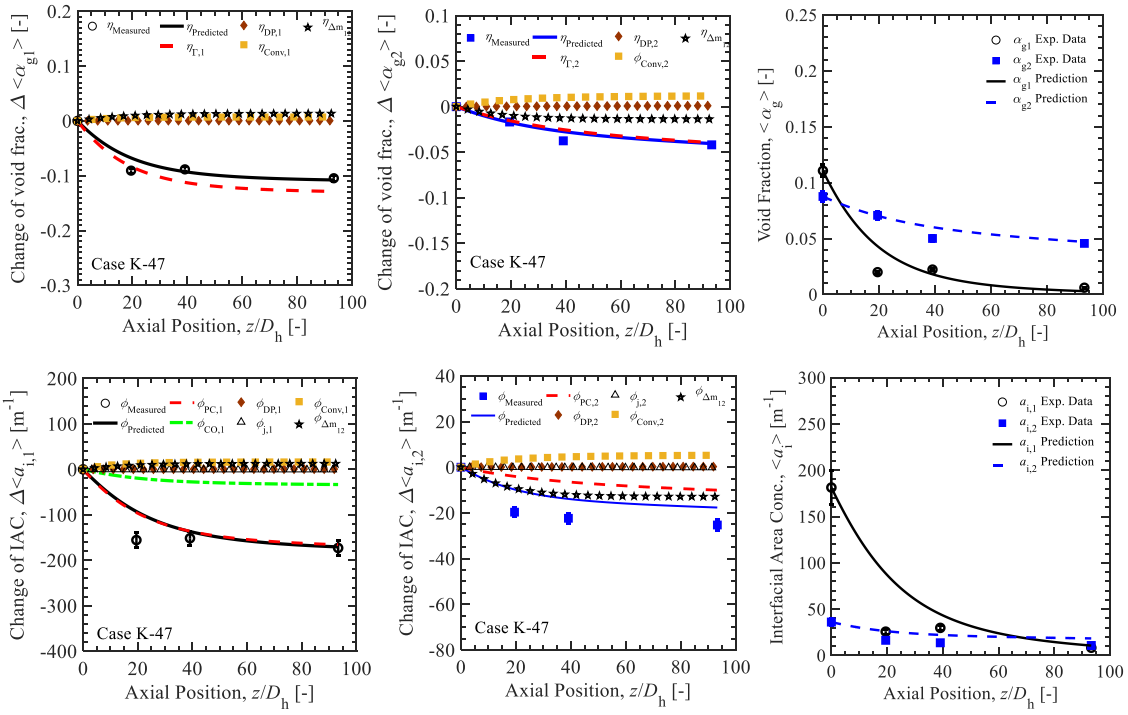

Figure 5.12: Validation of proposed two-group IATE formulation coupled with void transport equations for Case K-47.

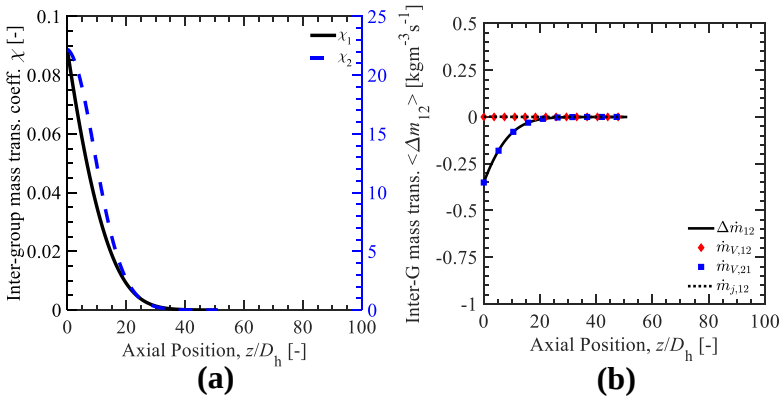

Figure 5.13: Results of proposed two-group IATE formulation coupled with void transport equations for Case K-12 showing (a) inter-group mass transfer coefficients (b) axial variation of the inter-group mass transfer term.

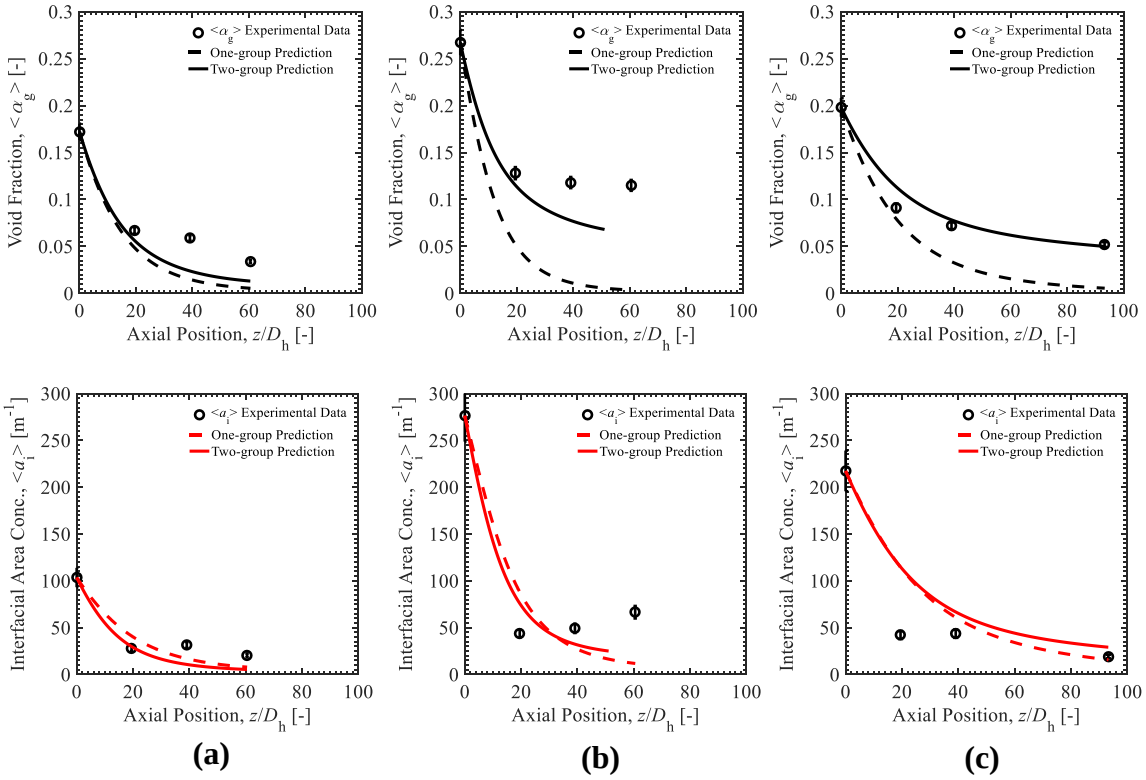

Figure 5.14: Validation of proposed one-group and two-group IATE formulations coupled with void transport equations for (a) Case K-7 (b) Case K-12 (c) Case K-47.

Keeping in mind that the expansion terms and interaction mechanisms are negligible for similar reasons as shown for the current model, three general observations can be made regarding the results in Figures 5.10-5.12. First, inter-group mass transfer and thermally controlled condensation are the significant source and sink terms which contribute to the change in void fraction and interfacial area concentration for group-2 while the change in group-2 void fraction

and interfacial area concentration is dominated by the thermally controlled condensation sink term. The results for the three cases highlight the effectiveness of the group-2 Nusselt number correlation based on the liquid film thickness. Second, there is a much larger contribution of the thermally controlled condensation sink term relative to the inertially controlled condensation sink term for group-1 bubbles which is consistent with previous findings (discussed in Chapter 4). As the thermally controlled condensation sink term is predicted by the continuity equation, it is critical that a coupled calculation of the void transport and IATE is performed to validate the IATE phase change terms, a point highlighted in the one-group IATE study in the previous chapter. Third from Figure 5.13, it can be observed that the net inter-group mass transfer decreases along the flow length due to the reduction in group-2 condensation as the subcooling decreases. This follows from its fundamental definition as it is expected that the distribution of group-1 bubbles per unit volume at the critical bubble volume decreases faster than the (average) group-1 bubble number density in condensing flows (Zhu et al., 2019). On the other hand, the trend in χ_2 is dictated by both the variation in χ_1 and the variation in the ratio of group-1 to group-2 bubble number density. Finally, with the new group-2 heat transfer coefficient and inter-group transfer coefficients incorporated in the two-group model, it is observed that group-2 void transport and group-2 IATE are not reduced to a single equation as postulated in Kumar and Brooks (2018). This is because thermally controlled condensation is the dominant sink term for group-2 void fraction while inter-group mass transfer is equally dominant for group-2 interfacial area concentration. From Figure 5.14, it can be observed that the one-group IATE simulations over predict condensation for all three cases with varying degrees depending on the local group-2 void fraction in the downstream ports. In general, the two-group IATE performs better for all three cases, especially Case K-12, as observed from Figure 5.14. The comparison of simulated change in group and total void fraction and interfacial area concentration versus experimental data is shown in Figure 5.15 for all conditions. The mean errors in total void fraction and interfacial area concentration for the forty-five cases of Kumar et al. (2019) are 16.2% and 13.2%, respectively. The corresponding mean errors for the forty-eight cases of Kumar et al. (2019) using the one-group IATE simulation are 17.6% and 14.2% for the void fraction and interfacial area concentration, respectively. Therefore, there is a ~1.5% improvement in total change in void fraction prediction using the two-group IATE model over the one-group IATE model. Although it is marginal, these errors could add up when simulating the complete test facility described in Chapter 3, for example, wherein subcooled boiling is followed by condensing flow. Furthermore, if the database had more two-group conditions, i.e. significant two-group void fraction throughout the unheated section, the two-group IATE model is expected to perform much better in comparison to one-group IATE.

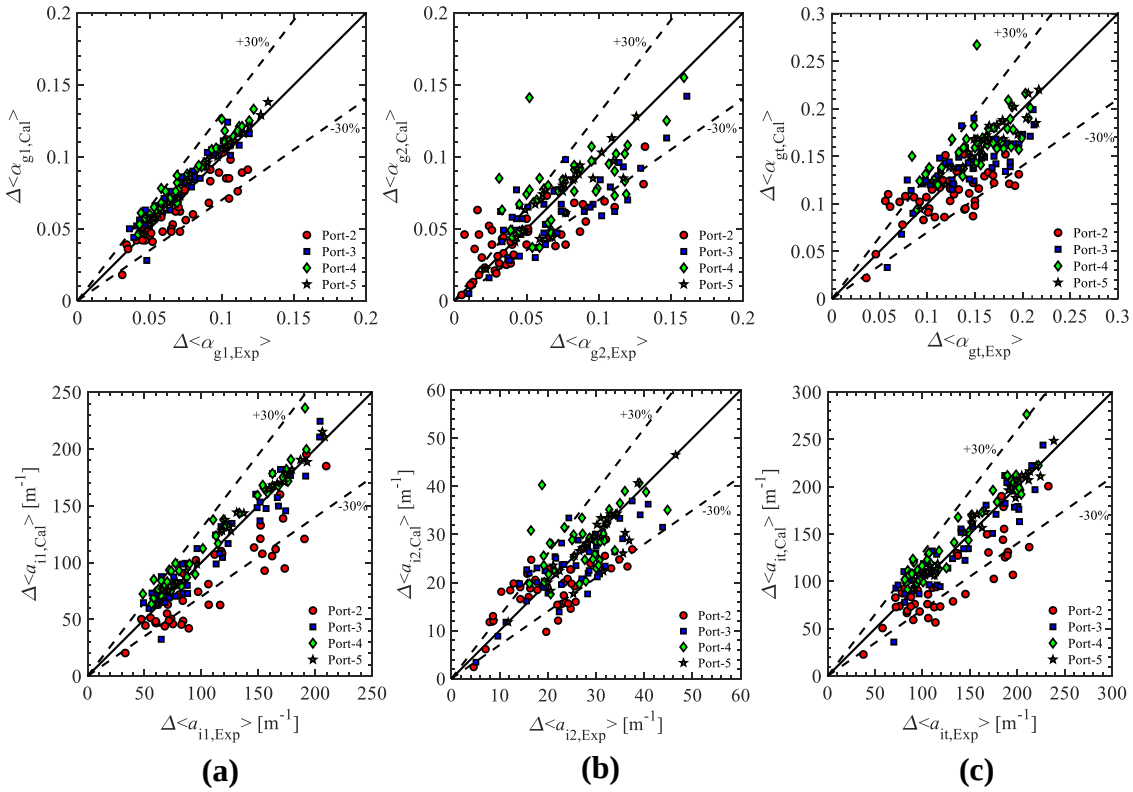

Figure 5.15 Comparison of simulated change in group void fraction (top) and group interfacial area concentration (bottom) with experimental data of Kumar et al. (2019) for (a) group-1 (b) group-2 (c) total based on the proposed coupled two-group model.

5.4. Conclusions

The current two-group two-fluid IATE model is reviewed for application in gas-dispersed condensing flows, and it is determined that the inter-group mass transfer term needs to be revised. The inter-group mass transfer model plays a crucial role in the closure of the two-group model, but past studies have largely focused on adiabatic air-water flows with limited studies in flows with phase change. In adiabatic air-water flows as well as subcooled boiling flows, the expansion of group-1 bubbles to group-2 bubbles dominates the inter-group mass term for which its applicability has been thoroughly validated. However, in condensing flows, the inter-group mass transfer term is driven by the condensation of group-2 bubbles to group-1 bubbles which the current model does not consider. In general, the shortcoming of the current two-group IATE model is that it cannot predict inter-group mass transfer due to volume change of group-2 bubbles. Validation of the current two-group steady-state area-averaged coupled void fraction transport and IATE model is undertaken with forty-five conditions from the database of Kumar et al. (2019). The current model gives poor overall results because the inter-group mass transfer term is incorrectly defined, driven by the net condensation of group-1 bubbles which acts as a source term for group-1 bubbles.

The current two-group model is modified to provide a general expression applicable to all flow conditions by expanding the definition of the inter-group mass transfer to account for mass transfer from group-2 to group-1. The proposed formulation ensures that the direction of inter-group mass transfer due to expansion from group-1 to group-2 is positive and the direction of inter-group mass transfer due to contraction from group-2 to group-1 is negative, which is achieved using the maximum and minimum functions. This ensures that the condensation of group-1 bubbles does not also generate group-1 through inter-group transfer, and the expansion of group-2 does not become a source of group-2 through inter-group transfer. A new inter-group mass transfer coefficient, χ_2, is also introduced for mass transfer from group-2 to group-1 and simplified bubble distribution cases indicate that the magnitude of χ_2 can become large when the bubble size is close to the critical diameter. A newly developed correlation for χ_1 is used in the χ_2 correlation with a functional form which ensures that the χ_2 correlation smoothly goes to zero as χ_1 and/or group-2 bubble number density tend to zero. Finally, a modification to the group-2 Nusselt number correlation is proposed to use the liquid film thickness instead of the Sauter mean diameter as an appropriate length scale for heat transfer of group-2 bubbles. A sensitivity analysis using the proposed two-group IATE model predicts an optimum value of 25% of the channel gap width for the liquid film thickness.

Validation of the proposed model was performed with forty-five two-group condensing flow conditions from the database of Kumar et al. (2019), similar to the current model validation. Three observations can be made regarding the two-group predictions. First, the proposed model predicts the correct trend for inter-group mass transfer term unlike the current model. Inter-group mass transfer and thermally controlled condensation are the major source/sink terms for both the bubble groups. Second, the three highlighted conditions in the previous chapter, give good predictions with the two-group IATE model in comparison to the poor void fraction predictions using the one-group IATE model. Third, the overall mean errors in change in total void fraction and total interfacial area concentration using the proposed model are 16.2% and 13.2%, respectively, better than the one-group IATE model predictions. One reason identified for the marginal benefit using the two-group IATE model using the current dataset is the lack of conditions with significant two-group void fraction throughout the simulation domain. However, when simulating a flow condition which could involve subcooled flow boiling followed by condensation, the errors introduced by the one-group IATE model could stack up. This demonstrates the need for the two-group IATE model which accounts for the differences in the transport properties between the two bubble groups.

CHAPTER 6. CONCLUSIONS

The application of IATE to phase change flows has largely focused on subcooled boiling and saturated boiling flows which involve complex phenomena such as wall nucleation, evaporation, condensation heat/mass transfer, etc. In order to isolate some of the interfacial phase change phenomenon, the focus of this work is on adiabatic steam-water flows, specifically condensing gas-dispersed flows through a combination of experimental and analytical approaches. The concluding chapter presents a summary of the research and lists the major contributions of this work along with future work/recommendations.

6.1. Summary of Findings

The two-fluid model coupled with interfacial area concentration for gas-dispersed condensing flows is studied in this work through a three-stage process of experimentation, modeling and benchmarking of the data.

A new database of steam-water flow in a vertical annulus experimental test facility was developed focusing on condensing, saturated and flashing flow. Five instrumentation ports in the unheated section provided local two-phase multi-group measurements of void fraction, interfacial area concentration and gas velocity along with pressure and liquid temperature. The dataset was designed for validation of one-dimensional system codes and multi-dimensional fluid dynamics codes and fills an important gap in the literature with high-resolution measurements for adiabatic two-phase flow. Local measurements for three representative cases were discussed. Parametric analysis was conducted using a one-dimensional flow description, provided by area-averaging and void-weighted averaging of two-phase parameters.

A total of eighty-five conditions were recorded with twenty-nine conditions at low pressure (less than 400 kPa) and fifty-six conditions at elevated pressure (between 500 and 930 kPa). The conditions spanned port 1 subcooling of 0-3.3^{o}C, port-1 area-average void fraction of ~ 3-43%, and test section mass flux of 258-1688 kg/m^2-s. A total of 48 condensing flow conditions were recorded, out of which 45 conditions had significant group-2 void fraction at the first measurement port and therefore classified as two-group condensing cases.

From the local measurements it was observed that at port 1, the group-1 void fraction had a heated-wall profile for subcooled inlet and a more uniform profile for a saturated inlet condition. It was found that the liquid temperature profile mirrored the void fraction profile with the local subcooling highest at the outer wall with the wall-peaked temperature profile eventually flattening out at the downstream ports as the flow got mixed. Another important observation was that group-

2 bubbles are generated even at low void fractions (less than 10%) with the group-2 void fraction profile showing an off-wall peaking as it is generated due to coalescence and expansion of group-1 bubbles. Furthermore, at the downstream ports, the group-2 bubbles tended to migrate to the center of the channel, and this lateral migration is beneficial for benchmarking of interfacial forces. It was shown that the interfacial area concentration profile is dominated by group-1 bubbles because of their greater surface area per unit volume relative to group-2 bubbles.

The system variables for the parametric analysis were system pressure, inlet mass flux, and port-1 subcooling. It was shown that a small temperature difference, be it subcooling or superheating, can drive rapid condensation or rapid void production due to flashing (at low system pressure), presenting a substantial challenge for modeling. For saturated inlet conditions, the void fraction profile was shown to increase much more rapidly at low pressure due to flashing in comparison to a steady increase in void fraction profile at elevated pressure conditions. Saturated inlet conditions did not exhibit any mass flux effect in comparison to subcooled inlet conditions which were shown to have a more rapid void fraction decrease along the test section at lower mass fluxes because of longer bubble residence times.

Using the newly acquired dataset as well as two other datasets available in the public domain, a comprehensive benchmarking of the one-group IATE was performed to validate the existing condensation model. The model of Park et al. (2007) was used in the current analysis wherein condensation sink terms are divided into thermally controlled condensation (decrease in bubble volume) and inertially controlled condensation (decrease in bubble number density). The drift flux model was used for gas velocity and was found to closely match the available gas velocity measurements. Similar to previous studies, it was found that the IATE model is dominated by phase change terms with negligible contributions from interaction mechanisms. By decoupling the IATE from the void fraction transport equation, called the decoupled model, it was found that the Nusselt number correlation of Zeitoun (1994) should be based on the boundary diameter with a dimensionless boundary diameter of 0.4 in order to replicate the current IATE approach. It was noted that this requirement stems from the fact that in the IATE model, the Nusselt number correlation is based on an average Sauter mean diameter whereas the correlation is derived based on the local Sauter mean diameter.

In order to be consistent with the Γ_g model in both the continuity equation and the IATE, a coupled validation of the IATE and void transport equation was conducted. It was found that the thermally controlled condensation sink term is the main driver for the decrease in void fraction. It was also found that the impact of using the boundary diameter in the Nusselt number correlation is higher than for the coupled model because the error in the void fraction prediction from the void

transport equation propagates to the IATE and vice versa. Overall, the coupled model was found to predict the void fraction and interfacial area concentration with reasonable accuracy across sixty conditions with mean errors of 19.0% and 16.6% in the change of void fraction and interfacial area concentration, respectively. A two-group approach was recommended when the inlet experimental group-2 void fraction to total void fraction (from the new database) exceeded 0.4 with a caveat that a significant group-2 void fraction was present in the downstream ports. The sensitivity analysis confirmed that the Nusselt number correlation of Zeitoun (1994), which was used for the current analysis, gave the best predictions across the three datasets. It was also found that the coupled IATE model is sensitive to gas velocity, highlighting the need to accurately model interfacial drag when solving the momentum equation.

The current two-group two-fluid IATE model was reviewed using the new dataset, and it was found that the current inter-group mass transfer term, responsible for bubble accounting, is erroneously defined leading to poor predictions. The error rose from that fact that previous two-group validation studies focused on subcooled boiling where the inter-group mass transfer term is dominated by expansion of group-1 bubbles to group-2 bubbles in comparison to condensation where group-2 bubbles condense to group-1 bubbles, an effect not considered by the present model.

The two-group two-fluid model was rederived to provide a general expression applicable to all flow conditions. The proposed formulation ensured that the inter-group mass transfer term included the effect of mass transfer from group-2 bubbles to group-1 bubbles. A new group-2 inter-group mass transfer coefficient was introduced and was defined to be proportional to the group-1 mass transfer coefficient and the ratio of group-1 to group-2 bubble number densities. A newly developed correlation was used for the group-1 mass transfer coefficient and correct limiting behavior was obtained for the inter-group transfer coefficients. A modification was also proposed to the group-2 Nusselt number correlation based on the liquid film thickness, defined as a fraction of the channel gap width, as an appropriate length scale for heat transfer of group-2 bubbles. In general, the group-2 predictions were found to be sensitive to heat transfer length scale.

The validation of the proposed model was conducted for forty-five two-group condensing flow conditions. The proposed model was found to predict the correct trends for void fraction and interfacial area concentration for both the bubble groups. Overall, the mean errors in the change in total void fraction and total interfacial area concentration predicted by the proposed model were 15.5% and 13.8%. Furthermore, the proposed model gave better predictions in total change in void fraction and interfacial area concentration in comparison to the one-group model for three chosen two-group condensing cases. It was concluded that the marginal benefit of the two-group model analysis with the current dataset was due to lack of adequate two-group condensing cases.

6.2. Major Contributions

The contributions of this work to the understanding of gas-dispersed condensation modeling for the two-fluid model can be summarized as follows:

1. A thorough review of the current state of the art interfacial area concentration prediction approaches is presented including past models and experimental datasets for gas-dispersed condensing flows.

2. A new adiabatic steam-water flow dataset is developed from a newly built test facility, providing high-resolution local two-phase group measurements of void fraction, gas velocity and interfacial area concentration, spanning across pressures, mass fluxes, and inlet subcooling, and significantly adding to the available experimental data.

3. Comprehensive benchmarking of the one-group condensing flow IATE model is performed with three experimental datasets across a range of pressure, mass flux, inlet subcooling, and inlet void fraction. A modification to the existing model has been proposed and good predictions are obtained with the new model. A criterion has been proposed to identify two-group condensing cases where the modified model is shown to do poorly.

4. The current two-fluid multi-group model has been rederived to obtain a generalized formulation for the inter-group mass term and a new correlation has been proposed for the group-2 inter-group mass transfer coefficient. The new inter-group mass transfer term ensures that physically consistent results are obtained for application of the multi-group two-fluid model to predict condensing flows.

5. The proposed model is benchmarked with the newly acquired condensing flow dataset. The predictions obtained with the new model are thoroughly presented and compared with the predictions obtained using the current two-group model as well as the one-group model.

6.3. Recommendations for Future Work

Future research opportunities emanating from the advances and challenges in the current work in terms of experimentation and interfacial modeling for the two-fluid model are as follows:

1. Recommendation for future experimental research could expand the newly acquired

steady-state database in vertical pipe flow to increase the heater power to generate higher group-2 void fraction at the inlet of the unheated section and validate the proposed two-group model. These experiments would have to be performed with high inlet liquid subcooling at sufficiently elevated pressures in order to avoid flashing. For higher void fraction, high-speed imaging in combination with a liquid film thickness sensor could be used to overcome the uncertainties involved with conductivity probes due to large vertical gaseous interfaces.

2. Recommended extension of the current work is to validate subcooled boiling flows using available state of the art wall boiling models along with the improved condensation model using the proposed two-group two-fluid formulation. With increased confidence in the condensation model, the wall boiling models could be isolated and benchmarked, including the onset of nucleate boiling.

3. Future benchmarks of the proposed two-group two-fluid model could include the momentum equation, to validate the interfacial transfer terms in adiabatic flow using the gas velocity measurements from the new dataset. Using the foundational approach established in the current work, the one-group/two-group IATE model could be incorporated in Computational Fluid dynamics codes (CFD) such as CFX, STAR-CCM+, etc. and thermal hydraulic system codes such as COBRA-TF, RELAP5, etc. and validated using the new dataset.

4. Future modeling opportunities in extending the current work could be the following: exploring the sensitivity of the characteristic heat transfer length scale using a more representative group-2 bubble shape, investigating the effect of group-2 bubble shapes on condensation sink terms, incorporating the effect of temperature gradient in the flow field in a one-dimensional flow description through covariances in averaged values, etc.

REFERENCES

Abdelmessih, A.H., Hooper, F.C., Nangia, S., "Flow effects on bubble growth and collapse in surface boiling," *Int. J. Heat Mass Trans.*, 15, pp. 115-125 (1972).

Akiyama, M., "Bubble collapse in subcooled boiling," Bulletin of JSME, 16, pp. 570-575 (1973).

Alali, A., "Development and Validation of a New Solver Based on the Interfacial Area Transport Equation for the Numerical Simulation of Sub-cooled Boiling with OpenFOAM CFD Code for Nuclear Safety Applications," PhD Thesis (2014).

Bae, B.U., Yun, B.J., Yoon, H.Y., Song, C.H. and Park, G.C., "Analysis of subcooled boiling flow with one-group interfacial area transport equation and bubble lift-off model," *Nuclear Engineering and Design*, 240, pp. 2281-2294 (2010).

Basu, N., Warrier, G. R., Dhir, V. K., "Wall heat flux partitioning during subcooled flow boiling: Part 1 - model development," *J. Heat Trans.*, 127, 131-140 (2005).

Brooks, C.S. and Hibiki, T., "Modeling and validation of interfacial area transport equation in subcooled boiling flow," *Journal of Nuclear Science and Technology*, pp. 1-13 (2016).

Brooks, C.S., Hibiki, T., "Wall nucleation modeling in subcooled boiling flow," *Int. J. Heat Mass Transf.*,", 86, pp. 183-196 (2015).

Brooks, C.S., Hibiki, T., Ishii, M., "Interfacial drag force in one-dimensional two-fluid model," *Progress in Nuclear Energy*, 61, pp. 57-68 (2012c).

Brooks, C.S., Ozar, B., Hibiki, T., "Interfacial area transport of subcooled boiling flow in a vertical annulus," *Nucl. Eng. Des.*, 269, pp. 152-163 (2014).

Brooks, C.S., Ozar, B., Hibiki, T., Ishii, M., "Two-group drift-flux model in boiling flow," *Int. J. Heat Mass Trans.*, 55, pp. 6121-6129 (2012b).

Brooks, C.S., Paranjape, S.S., Ozar, B., Hibiki, T. and Ishii, M., "Two-group drift-flux model for closure of the modified two-fluid model," *Int. J. Heat Mass Transf.*, 37, pp. 196-208 (2012a).

Chen, Y.M., Mayinger, F., "Measurement of heat transfer at phase interface of condensing bubble," *Int. J. Multiphase Flow*, 18, pp. 877-890 (1992).

Dandekar, A.V., Brooks, C.S., "Modeling of Void Fraction Covariance in Two-phase Flows with Phase Change," International Journal of Heat and Mass Transfer, 100, 231-242 (2016).

Dejesus, J.M., Kawaji, M. "Investigation of interfacial area and void fraction in upward, cocurrent gas-liquid flow," *The Canadian Journal of Chemical Engineering*, 68, pp. 904-912 (1990).

Delhaye, J. M., "Some issues related to the modeling of interfacial areas in gas–liquid flows I. The conceptual issues," *Comptes Rendus de l'Académie des Sciences-Series IIB-Mechanics*, 329, 5, pp. 397-410 (2001).

Florschuetz, L.W., B.T. Chao, "On the mechanics of vapor bubble collapse," *J. Heat Trans.,* 87, pp. 209-220 (1965).

Fu, X. Y., Ishii, M., "Two-group interfacial area transport in vertical air-water flow: I. Mechanistic model," *Nucl. Eng. Des.*, 219, pp. 143-168 (2003a).

Fu, X. Y., Ishii, M., "Two-group interfacial area transport in vertical air–water flow-II. Model evaluation," *Nucl. Eng. Des.*, 219, pp. 169-190 (2003b).

Fu, Xinyu, "Interfacial area measurement and transport modeling in air-water two-phase flow," Ph.D. Thesis, Purdue University (2001).

Fullmer, W.D., Kumar, V., Brooks, C.S., "Validation of RELAP5/MOD3. 3 for subcooled boiling, flashing and condensation in a vertical annulus," *Progress in Nuclear Energy*, 93, pp. 205-217 (2016).

Garimella, S., Agarwal, A., Fronk, B. M., "Condensation heat transfer in rectangular microscale geometries," *International Journal of Heat and Mass Transfer*, 100, pp. 98-110 (2016).

Goodheart, K., Alleborn, N., Chatelain, A., Keheley, T., "Analysis of the interfacial area transport model for industrial two-phase boiling flow applications," NURETH-15, Pisa, Italy (2013).

Grober, H., Erk, S., Grigull, U., "*Die grundgesetze der Warmeubertragung*," Springer (1955).

Hibiki, Ishii, M., "Two-group interfacial area transport equations at bubbly-to-slug flow transition," *Nucl. Eng. Des.*, 202, pp. 39-76 (2000b).
Hibiki, T., Ishii, M., "Active nucleation site density in boiling systems," *Int. J. Heat Mass Transf.*, 46, pp. 2587-2601 (2003).
Hibiki, T., Ishii, M., "Distribution parameter and drift velocity of drift-flux model in bubbly flow," *Int. J. Heat Mass Transf.*, 45, pp. 707-721 (2002).
Hibiki, T., Ishii, M., "One-group interfacial area transport of bubbly flows in vertical round tubes," *Int. J. Heat Mass Transf.*, 43, pp. 2711-2726 (2000a).
Hibiki, T., Situ, R., Mi, Y., Ishii, M., "Modeling of bubble-layer thickness for formulation of one-dimensional interfacial area transport equation in subcooled boiling two-phase flow," *Int. J. Heat Mass Transf.*, 46, pp. 1409-1423 (2003).
Hibiki, T., Takamasa, T., Ishii, M., "Interfacial area transport of bubbly flow in a small diameter pipe," *Journal of Nuclear Science and Technology*, 38, pp. 614-620 (2001).
Hsu, Y. Y., "Condensation heat transfer," *Thermohydraulics of Two-Phase Systems for Industrial Design and Nuclear Engineering*, Delhaye, J.M., Giot, M. and Riethermuller, M.L., Eds., McGraw-Hill, New York, pp. 297-304 (1981).
Isenberg, J. Sideman, S., "Direct contact heat transfer with change of phase: bubble condensation in immiscible liquids," *Int. J. Heat Mass Transf.*, 13, pp. 997-1011, (1970).
Ishii, M., "One-dimensional drift-flux model and constitutive equations for relative motion between phases in various two-phase flow regimes," Technical report ANL-77-47, Argonne National Laboratory, Chicago, IL, USA (1977).
Ishii, M., Hibiki, T., Thermo-Fluid Dynamics of Two-phase Flow, Springer, New York, 2nd Ed., (2011).
Ishii, M., Kim, S., "Development of one-group and two-group interfacial area transport equation," *Nuclear science and engineering*, 146, pp. 257-273 (2004).
Ishii, M., Mishima, K., "Study of Two-fluid Model and Interfacial Area," NUREG/CR-1873. ANL-80-111, USA (1980).
Ishii, M., Mishima, K., "Two-fluid model and hydrodynamic constitutive relations," *Nucl. Eng. Des.*, 82, pp. 107-126 (1984).
Ishii, M., Thermo-fluid dynamic theory of two-phase flow, Eyrolles (1975).
Ishii, M., Wu, Q., Assad., A, Uhle, J., "Interfacial area transport equation for two-fluid model formulation," Proceedings of MUST Meeting (1998).
Ishii, M., Zuber, N., "Drag coefficient and relative velocity in bubbly, droplet or particulate flows," *AIChE Journal*, 25, pp. 843-55 (1979).
Kataoka, I., Ishii, M., Serizawa, A., "Local formulation and measurements of interfacial area concentration in 2-phase flow," *International Journal of Multiphase Flow*, 12, pp. 505-529 (1986).
Kim, S., "Interfacial area transport equation and measurement of local interfacial characteristics," (Unpublished doctoral dissertation), Nuclear Engineering, Purdue University, West Lafayette, IN (1999).
Kim, S., Fu, X., Wang, X., Ishii, M., "Development of the miniaturized four sensor conductivity probe and the signal processing scheme," *Int. J. Heat Mass Transfer*, 43, pp. 4101-4118 (2000).
Kocamustafaogullari, G., Ishii M., "Foundation of the interfacial area transport equation and its closure relations," *Int. J Heat Mass Transf.*, 38, pp. 481-493, (1995).
Kosky, P.G., "Bubble growth measurements in uniformly superheated liquids," *Chemical Engineering Science*, 23, pp. 695-706 (1968).
Kumar, V., Brooks, C.S., "Inter-group mass transfer modeling in the two-group two-fluid model with interfacial area transport equation in condensing flow," *Int. J. Heat Mass Transf.*, 119, pp. 688-703 (2018).

Kumar, V., Brooks, C.S., "Validation and model sensitivity of the interfacial area transport equation in condensing flows," *Int. J. Heat Mass Transf.*, 113, pp. 647-661 (2017).
Kumar, V., Ooi, Z. J., Brooks, C.S., "Forced convection steam-water experimental database in a vertical annulus with local measurements," *Int. J. Heat Mass Transf.*, 137, pp. 216-228 (2019).
Lin, C.H., Hibiki, T., "Databases of interfacial area concentration in gas–liquid two-phase flow," *Progress in Nuclear Energy*, 74, pp.91-102 (2014).
Ma, K., Guo, L., Wang, Y., "Interfacial area transport of subcooled water–steam condensing bubbly flow in vertical pipe," *Int. J. Heat Mass Transf.*, 86, pp. 78-89 (2015).
Manera, A., Prasser, H. M., Lucas, D., Van Der Hagen, T. H. J. J., "Three-dimensional flow pattern visualization and bubble size distributions in stationary and transient upward flashing flow," *International journal of multiphase flow*, 32, pp. 996-1016 (2006).
Michta, E., "Modeling of Subcooled Nucleate Boiling with OpenFOAM," M.Sc. thesis, Royal Institute of Technology, Stockholm, Sweden (2011).
Mishima, K., Ishii, M., "Flow regime transition criteria for upward two-phase flow in vertical tubes," *Int. J. Heat Mass Transf.*, 27, pp. 723-737 (1984).
Neal, L. G., Bankoff, S. G., "A high resolution resistivity probe for determination of local void properties in gas-liquid flow," *AIChE Journal*, 9, pp. 490-494 (1963).
Nguyen, V. T., Song, C. H., Tran, C. T., "CFD prediction of subcooled boiling with advanced mechanistic models of interfacial area transport equation," NURETH-16, Chicago, U.S.A (2015).
Ooi, Z. J., Kumar, V., Bottini, J. L., Brooks, C. S., "Experimental investigation of variability in bubble departure characteristics between nucleation sites in subcooled boiling flow," *Int. J. Heat Mass Transf.*, 118, 327-339 (2018).
Ozar, B., "Interfacial area transport of steam-water two phase flow in a vertical annulus at elevated pressures," PhD thesis, Purdue University, West Lafayette, IN (2009).
Ozar, B., Brooks, C.S., Hibiki, T., Ishii, M., "Interfacial area transport of vertical upward steam-water two-phase flow in an annular channel at elevated pressures," *Int. J. Heat Mass Transf.*, 57, pp. 504-518 (2013).
Ozar, B., Dixit, A., Chen, S.W., Hibiki, T., Ishii, M. "Interfacial area concentration in gas–liquid bubbly to churn-turbulent flow regime," *Int. J. of Heat and Fluid Flow*, 38 pp. 168-179 (2012).
Ozar, B., Jeong, J. J., Dixit, A., Julia, J. E., Hibiki, T., Ishii, M., "Flow structure of gas-liquid two-phase flow in an annulus," *Chemical Engineering Science*, 63, pp. 3998-4011 (2008).
Park, H.S., Lee, T.H., Hibiki, T., Baek, W.P., Ishii, M., "Modeling of the condensation sink term in an interfacial area transport equation," *Int. J. Heat Mass Transf.*, 50, pp. 5041-5053 (2007).
Park, I.K., Yoon, H.Y. and Cho, H.K., "Simulations of air–water flow and subcooled boiling flow using the CUPID code," *Journal of Nuclear Science and Technology*, 50, pp. 813-827 (2013).
Prosperetti, A., "Vapor bubbles," *Annual Review of Fluid Mechanics*, 49, pp. 221-248, (2017).
Rayleigh, J.W.S., "On the pressure developed in a liquid during the collapse of a spherical cavity," Philos. Mag. 34, pp. 94-98 (1917).
RELAP5/MOD3.3, Code Manual Volume IV: Models and Correlations. U.S. NRC Contractors Report, NUREG/CR-5535/Rev P4-Vol IV (2010).
Revankar, S. T., Ishii, M., "Theory and measurement of local interfacial area using a 4 sensor probe in 2-phase flow," *Int. J. Heat Mass Transf.*, 36, pp. 2997-3007 (1993).
Ruckenstein, E., "On heat transfer between vapor bubbles in motion and the boiling liquid from which they are generated," *Chem. Eng. Sci.*, 10, pp. 22-30 (1959).
Schlegel, J.P., Hibiki, T. and Ishii, M., "Two-group modeling of interfacial area transport in large diameter channels," *Nuclear Engineering and Design*, 293, pp.75-86 (2015).

Schlegel, J.P., Hibiki, T., Shen, X., Appathurai, S., Subramani, H., "Prediction of interfacial area transport in a coupled two-fluid model computation," *Journal of Nuclear Science and Technology*, 54, pp. 58-73 (2017).

Shademan, M., Balachandar, R., Barron, R., "CFD Simulation of Boiling Heat Transfer Using OPENFOAM," Proceedings of the ASME 2014 International Mechanical Engineering Congress and Exposition, Montreal (2014).

Spore, J.W., et al., TRACM/ FORTRAN 90 (Version 3.0) Theory Manual, LA-UR-00-910, Los Alamos National Laboratory, Los Alamos, New Mexico and Penn State University, State College, Pennsylvania (2000).

Sun, X. D., Ishii, M., Kelly, J. M., "Modified two-fluid model for the two-group interfacial area transport equation," Annals of Nuclear Energy, 30, pp. 1601-1622 (2003).

Sun, X., Kim, S., Ishii, M., Beus, S.G., "Model evaluation of two-group interfacial area transport equation for confined upward flow," *Nucl. Eng. Des.*, 230, pp. 27-47 (2004b).

Sun, X., Kim, S., Ishii, M., Beus, S.G., "Modeling of bubble coalescence and disintegration in confined upward two-phase flow," *Nucl. Eng. Des.*, 230, pp.3-26, (2004a).

TRACE V5.0 User's Manual Vol. 2: Modeling Guidelines, U.S. Nuclear Regulatory Commission (2007).

Wallis, G. B., ''Review - Theoretical Models of Gas-Liquid Flows,'' *J. Fluid Eng.*, 104, pp. 279-283 (1982).

Worosz, T.S., "Interfacial area transport equation for bubbly to cap-bubbly transition flows," PhD Thesis, The Pennsylvania State University, U.S.A. (2015).

Worosz, T.S., Bernard, M., Kong, R., Toptan, A., Kim, S. and Hoxie, C., "Sensitivity studies on the multi-sensor conductivity probe measurement technique for two-phase flows," *Nucl. Eng. Des.*, 310, pp. 552-563 (2016).

Wu, Q., Ishii, M., "Sensitivity study on double-sensor conductivity probe for the measurement of interfacial area concentration in bubbly flow," *International Journal of Multiphase Flow*, 25, pp. 55-173 (1999).

Wu, Q., Kim, S., Ishii, M., Beus, S.G., "One-group interfacial area transport in vertical bubbly flow," Int. J Heat Mass Transfer., 41, pp. 1103-1112 (1998).

Yao, W., Morel, C., "Volumetric interfacial area prediction in upward bubbly two-phase flow," *Int. J Heat Mass Transf.*, 47, pp. 307-328 (2014).

Zeitoun, O. M., "Subcooled flow boiling and condensation," PhD Thesis, McMaster University, Canada (1994).

Zeitoun, O., Shoukri, M., Chatoorgoon, V. "Measurement of interfacial area concentration in subcooled liquid-vapour flow," *Nuclear Engineering and Design* 152, pp. 243-255 (1994).

Zhu, Longxiang., Ooi, Z.J., Brooks, C.S., "Current Intergroup Mass Transfer Limitations in the Multi-group Two-fluid Model," The 18th International Topical Meeting on Nuclear Reactor Thermal Hydraulics (NURETH-18), Portland, USA, August 18-23, 2019.

Zuber, N., "The dynamics of vapor bubbles in nonuniform temperature fields," *Int. J. Heat Mass Transf.*, 2, pp. 83-98 (1961).

Zuber, N., Findlay, J., "Average volumetric concentrations in two-phase flow systems." *J. Heat Transf.* 87, pp. 453-568 (1965).

Zwick, S.A., Plesset, M.S., "On the dynamics of small vapor bubbles in liquids," *J. Math. Phys.*, 33, pp. 308-330 (1955).

APPENDIX A IAC correlations and models for one-group IATE study.

Table A.1 List of IAC correlations.

Reference	Interfacial area concentration correlation
RELAP5/MOD3.3 (2010)	$\langle a_i \rangle = \frac{3.6\langle \alpha_g \rangle}{\langle D_b \rangle}, \langle D_b \rangle = 5\sigma / \rho_f \left(v_g - v_f \right)^2$
TRACE V5.0 (2007)	$\langle a_i \rangle = \frac{6.0\langle \alpha_g \rangle}{\langle D_b \rangle}, \langle D_b \rangle = 2\sqrt{\sigma / g\left(\rho_f - \rho_g \right)}$
Zeitoun et al. (1994)	$\langle a_i \rangle = 3.24\left\{ \sigma / g\left(\rho_f - \rho_g \right) \right\}^{-0.55} \langle \alpha_f \rangle^{0.757} \left(G / \mu_f \right)^{-1}$
Dejesus & Kawaji (1990)	$\langle a_i \rangle = 167.6 \langle j_g \rangle^{0.61} \langle j_f \rangle^{0.34}$

Table A.2 List of Nusselt number correlations.

Reference	Nusselt number correlation
Ruckenstein (1959)	$Nu_c = \frac{4}{\sqrt{\pi}} \mathrm{Re}_b^{0.5} \mathrm{Pr}_\mathrm{f}^{0.5}$
Isenberg and Sideman (1970)	$Nu_c = \frac{1}{\sqrt{\pi}} \mathrm{Re}_b^{0.5} \mathrm{Pr}_\mathrm{f}^{1/3}$
Akiyama (1973)	$Nu_c = 0.37 \mathrm{Re}_b^{0.6} \mathrm{Pr}_\mathrm{f}^{1/3}$
Zeitoun (1994)	$Nu_c = 2.04 \mathrm{Re}_b^{0.61} \alpha_g^{0.328} Ja^{-0.308}$
TRAC-M/F90 (2000)	$Nu_c = \begin{cases} 2 + \left(0.4 \mathrm{Re}_b^{0.5} + 0.06 \mathrm{Re}_b^{2/3} \right) \mathrm{Pr}_\mathrm{f}^{0.4} & \mathrm{Re}_b \le 400 \\ 0.185 \mathrm{Re}_b^{0.7} \mathrm{Pr}_\mathrm{f}^{0.5} & 400 \le \mathrm{Re}_b \le 10^4 \\ 116.7 \mathrm{Pr}_\mathrm{f}^{0.5} & \mathrm{Re}_b \ge 10^4 \end{cases}$

Table A.3 Model constants used in the IATE (Hibiki and Ishii, 2000a).

Parameter	Value
Random collision	$C_{RC}^{(1)} = 0.188$
	$C_{RC}^{(2)} = 0.29$
Turbulent impact	$C_{TI}^{(1)} = 0.264$
	$C_{TI}^{(2)} = 1.37$
Interfacial area shape factor	$\psi_{ai} = 1/36\pi$
Maximum allowable void fraction	$\alpha_{\max} = 0.52$

APPENDIX B Summary of databases for validating IATE.

Table B.1 Summary of databases from Zeitoun (1994) and Ozar et al. (2013) for benchmarking one-group IATE.

Reference	**Case ID**	**Pressure P_{P1} [kPa]**	**Subcooling $\Delta T_{sub,P1}$ [^oC]**	**Mass flux G [kg/m^2-s]**	**Void frac. $\alpha_{g,P1}$ [%]**	**IAC $a_{i,P1}$ [m^{-1}]**
Zeitoun (1994)	Z-1	110	4.8	205.5	18.1	177.3
	Z-2	135	7.5	327.4	18.1	156.1
	Z-3	103	6.3	205.5	6.7	86.3
	Z-4	128	9.8	327.4	6.7	92.9
	Z-5	162	10.7	413.9	14.9	150.2
	Z-6	170	13.4	492.39	24.1	216.6
	Z-7	180	18.8	506.24	20.3	154.7
	Z-8	103	2.6	139.3	16.2	165.1
Ozar (2013)	O-1	504	1.35	947.8	18.7	216.7
	O-2	947	1.10	937.4	20.2	250.4
	O-3	946	1.27	927.3	17.0	231.8
	O-4	750	1.55	933.0	15.7	242.8

Table B.2 Summary of new database for benchmarking one-group & two-group IATE.

Case ID	P_{in} [kPa]	$\Delta T_{sub,P1}$ [^oC]	G [kg/m^2-s]	$\alpha_{g1,P1}$ [%]	$\alpha_{g2,P1}$ [%]	$a_{i1,P1}$ [m^{-1}]	$a_{i2,P1}$ [m^{-1}]
Run 1	197	2.37	938	7.4	10.5	99.3	29.3
Run 2	197	2.49	938	5.7	18.2	78.4	40.7
Run 3	191	2.23	1170	7.2	13.3	96.1	36.3
Run 4	192	2.33	1299	7.2	16.4	95.8	42.6
Run 5	193	2.13	1432	8.4	14.2	109.4	40.0
Run 6	192	2.20	1688	10.7	10.2	137.6	30.1
Run 7	348	2.05	508	4.8	12.5	70.9	32.6
Run 8	349	2.09	691	5.4	11.8	75.0	32.0
Run 9	349	2.15	702	5.3	13.3	75.8	34.2
Run 10	355	2.41	927	6.5	11.8	87.2	31.0
Run 11	354	1.77	928	6.2	13.3	89.4	35.6
Run 12	333	1.69	948	12.1	14.6	236.1	40.3
Run 13	344	1.97	1173	7.7	14.8	106.2	36.5
Run 14	343	1.90	1370	8.4	14.7	115.6	37.4
Run 15	503	2.62	352	4.4	9.4	75.0	31.5
Run 16	504	2.27	359	4.9	8.1	80.0	28.0
Run 17	505	2.46	492	5.4	10.0	83.0	28.8
Run 18	505	2.31	492	6.0	7.8	92.8	23.5
Run 19	503	2.00	702	9.7	10.4	165.7	40.7
Run 20	507	2.67	704	5.7	9.3	82.8	27.1
Run 21	503	2.27	929	10.3	11.7	169.7	46.5
Run 22	504	1.92	933	11.8	8.9	181.0	36.2
Run 23	498	2.23	1158	9.4	12.8	133.9	37.3
Run 24	725	3.20	258	5.8	6.2	98.6	20.0
Run 25	724	2.51	262	5.0	7.4	76.3	25.6
Run 26	727	2.75	364	9.8	8.4	178.4	33.4
Run 27	727	3.06	365	2.5	6.9	63.5	28.1
Run 28	726	2.25	493	8.0	8.8	137.6	32.3
Run 29	725	2.85	500	7.4	9.2	128.2	34.1
Run 30	724	3.25	685	10.4	3.4	210.5	11.8
Run 31	735	1.16	706	6.8	4.3	101.3	16.3
Run 32	726	2.83	708	8.6	8.3	143.4	29.6
Run 33	733	2.12	940	9.1	6.7	136.9	20.6
Run 34	732	2.22	944	9.1	9.2	144.2	26.5
Run 35	727	2.22	1115	12.8	8.8	215.2	33.3
Run 36	731	1.44	1143	3.3	0.1	68.0	0.0
Run 37	737	1.07	1168	5.6	2.2	79.3	8.7
Run 38	737	0.92	1338	6.3	2.2	91.0	9.0
Run 39	899	3.17	262	6.4	6.1	112.3	19.8

Table B.2 (*cont.*)

Case ID	**P_{in} [kPa]**	**$\Delta T_{sub,P1}$ [ºC]**	**G [kg/m^2-s]**	**$\alpha_{g,P1}$ [%]**	**$\alpha_{g,P2}$ [%]**	**$a_{i,P1}$ [m^{-1}]**	**$a_{i,P2}$ [m^{-1}]**
Run 40	900	2.26	271	5.7	9.3	92.6	30.8
Run 41	909	3.04	496	10.0	5.9	182.0	22.4
Run 42	910	2.25	504	9.6	7.1	168.1	28.2
Run 43	906	2.42	689	10.0	6.5	190.6	21.7
Run 44	904	2.51	693	9.5	9.3	164.3	34.4
Run 45	905	1.74	890	8.8	1.2	135.2	5.0
Run 46	900	2.42	897	10.8	9.0	186.5	34.8
Run 47	903	1.63	911	10.1	9.8	181.3	36.1
Run 48	900	2.10	1115	12.1	8.8	199.6	34.9

APPENDIX C Closure relations for one-group and two-group IATE model.

Table C.1 Modeling and closure of coupled validation of one-group IATE and void transport in upward gas-dispersed condensing flows.

Model and contributing work	**Equations**
IATE pressure change and convection sources/sink terms	$\langle \phi_{DP} \rangle = -\frac{2}{3}\left(\frac{\langle a_i \rangle}{\langle \alpha_g \rangle}\right)\left\{\frac{\langle \alpha_g \rangle}{\rho_g}\langle\langle v_g \rangle\rangle \frac{d\langle \rho_g \rangle}{dz}\right\}, \langle \phi_{Conv} \rangle = -\langle a_i \rangle \frac{d\langle\langle v_g \rangle\rangle}{dz}.$
IATE interaction mechanisms sources/sink terms Based on: Hibiki and Ishii (2000a)	$\langle \phi_{RC} \rangle = -\left(\frac{\langle \alpha_g \rangle}{\langle a_i \rangle}\right)^2 \frac{C_{RC}^{(1)} \langle \alpha_g \rangle^2 \varepsilon^{1/3}}{\langle D_{Sm} \rangle^{11/3}\left(\alpha_{g,\max} - \langle \alpha_g \rangle\right)} \exp\left(-C_{RC}^{(2)}\left(\frac{\langle D_{Sm} \rangle^5 \rho_f^3 \varepsilon^2}{\sigma^3}\right)^{1/6}\right)$ $\langle \phi_{TI} \rangle = \left(\frac{\langle \alpha_g \rangle}{\langle a_i \rangle}\right)^2 \frac{C_{TI}^{(1)}\left(1-\langle \alpha_g \rangle\right)\varepsilon^{1/3}}{\langle D_{Sm} \rangle^{11/3}\left(\alpha_{g,\max} - \langle \alpha_g \rangle\right)} \exp\left(-C_{TI}^{(2)}\left(\frac{\sigma}{\rho_f \langle D_{Sm} \rangle^{5/3} \varepsilon^{2/3}}\right)\right)$
Condensation model Based on: Park et al. (2007)	$\langle \phi_{CO} \rangle = -\pi \beta_{bc}^2 \langle D_{Sm} \rangle^2 \frac{\langle n_b \rangle}{\langle t_c \rangle}, \langle \eta_{CO} \rangle = -\frac{\pi \beta_c^3 \langle D_{Sm} \rangle^3}{6}\frac{\langle n_b \rangle}{\langle t_c \rangle}$ $\langle \phi_{PC} \rangle = -4\pi(1-p_c)\langle n_b \rangle \langle Nu_c \rangle \langle Ja \rangle \langle \alpha_t \rangle$ $\langle \eta_{PC} \rangle = -\pi(1-p_c)\langle D_{Sm} \rangle \langle n_b \rangle \langle Nu_c \rangle \langle Ja \rangle \langle \alpha_t \rangle$ $\langle t_c \rangle = \frac{\langle D_{Sm} \rangle^2 \left(1-\beta_{bc}^2\right)}{4}\frac{\rho_g h_{fg}}{\langle Nu_c \rangle k_f \langle \Delta T_{sub} \rangle}$ *Where,* $\langle \mathrm{Re}_b \rangle = \frac{\rho_f \langle U_b \rangle \langle D_{bc} \rangle}{\mu_f}, \langle U_b \rangle = \frac{1.53}{1-\langle \alpha_g \rangle}\left(\frac{\Delta \rho g \sigma}{\rho_f^2}\right)^{1/4}, \langle D_{bc} \rangle = \beta_{bc} \langle D_{Sm} \rangle$ $\langle Ja \rangle = \frac{\rho_f c_{pf}\left(\langle T_{sat} \rangle - \langle T_f \rangle\right)}{\rho_g h_{fg}}.$
Drift-Flux model (DFM) Based on: Zuber and Findlay (1965) Ishii (1977) Hibiki and Ishii (2002)	$\langle\langle v_g \rangle\rangle = C_o \langle j \rangle + \langle\langle v_{gj} \rangle\rangle$ $C_o = \left[C_\infty - (C_\infty - 1)\sqrt{\frac{\rho_g}{\rho_f}}\right]$ $\langle\langle v_{gj} \rangle\rangle = \sqrt{2}\left(\frac{\Delta \rho g \sigma}{\rho_f^2}\right)^{1/4}\left(1-\langle \alpha_g \rangle\right)^{7/4}$
Decoupled IATE	$\Delta\langle a_i \rangle = \frac{\Delta z}{\langle\langle v_g \rangle\rangle}\left\{\langle \phi_{PC} \rangle + \langle \phi_{DP} \rangle + \sum_j \langle \phi_j \rangle + \langle \phi_{CO} \rangle + \langle \phi_{Conv} \rangle\right\}$
Coupled void transport equation and IATE	$\Delta\langle \alpha_g \rangle = \frac{\Delta z}{\langle\langle v_g \rangle\rangle}\left\{\langle \eta_{PC} \rangle + \langle \eta_{CO} \rangle + \langle \eta_{DP} \rangle + \langle \eta_{Conv} \rangle\right\}$ $\Delta\langle a_i \rangle = \frac{\Delta z}{\langle\langle v_g \rangle\rangle}\left\{\langle \phi_{PC} \rangle + \langle \phi_{DP} \rangle + \sum_j \langle \phi_j \rangle + \langle \phi_{CO} \rangle + \langle \phi_{Conv} \rangle\right\}$ *Where,* $\langle \eta_{DP} \rangle = -\langle\langle v_g \rangle\rangle \frac{\langle \alpha_g \rangle}{\rho_g}\frac{d}{dz}\langle \rho_g \rangle,$ $\langle \eta_{Conv} \rangle = -\langle \alpha_g \rangle \frac{d}{dz}\langle\langle v_g \rangle\rangle.$

Table C.2 Modeling and closure of coupled validation of two-group IATE and void transport in upward gas-dispersed condensing flows.

Model and contr. work	Equations
Coupled void transport equation and IATE	$\Delta\langle\alpha_{g1}\rangle=\frac{\Delta z}{\langle\langle v_{g1}\rangle\rangle}\left\{\langle\eta_{\Gamma,1}\rangle+\langle\eta_{DP,1}\rangle-\langle\eta_{\Delta m_{12}}\rangle+\langle\eta_{Conv,1}\rangle\right\}$, $\Delta\langle a_{i,1}\rangle=\frac{\Delta z}{\langle\langle v_{g1}\rangle\rangle}\left\{\langle\phi_{PC,1}\rangle+\langle\phi_{DP,1}\rangle+\sum_j\langle\phi_{j,1}\rangle-\langle\phi_{\Delta m_{12}}\rangle+\langle\phi_{CO,1}\rangle+\langle\phi_{Conv,1}\rangle\right\}$ $\Delta\langle\alpha_{g2}\rangle=\frac{\Delta z}{\langle\langle v_{g2}\rangle\rangle}\left\{\langle\eta_{\Gamma,2}\rangle+\langle\eta_{DP,2}\rangle+\langle\eta_{\Delta m_{12}}\rangle+\langle\eta_{Conv,2}\rangle\right\}$, $\Delta\langle a_{i,2}\rangle=\frac{\Delta z}{\langle\langle v_{g2}\rangle\rangle}\left\{\langle\phi_{PC,2}\rangle+\langle\phi_{DP,2}\rangle+\sum_j\langle\phi_{j,2}\rangle+\langle\phi_{\Delta m_{12}}\rangle+\langle\phi_{Conv,2}\rangle\right\}$.
Group void transport source/sink terms	$\langle\eta_{\Gamma,1}\rangle=\langle\eta_{PC,1}\rangle+\langle\eta_{CO,1}\rangle$, $\langle\eta_{DP,1}\rangle=-\langle\langle v_{g1}\rangle\rangle\frac{\langle\alpha_{g1}\rangle}{\langle\rho_g\rangle}\frac{d\langle\rho_g\rangle}{dz}$, $\langle\eta_{Conv,1}\rangle=-\langle\alpha_{g1}\rangle\frac{d\langle\langle v_{g1}\rangle\rangle}{dz}$, $\langle\eta_{\Gamma,2}\rangle=\langle\eta_{PC,2}\rangle$, $\langle\eta_{DP,2}\rangle=-\langle\langle v_{g2}\rangle\rangle\frac{\langle\alpha_{g2}\rangle}{\langle\rho_g\rangle}\frac{d\langle\rho_g\rangle}{dz}$, $\langle\eta_{Conv,2}\rangle=-\langle\alpha_{g2}\rangle\frac{d\langle\langle v_{g2}\rangle\rangle}{dz}$.
Group IATE sources/sink terms	$\langle\phi_{DP,1}\rangle=-\frac{2}{3}\left(\frac{\langle a_{i,1}\rangle}{\langle\alpha_{g1}\rangle}\right)\left\{\frac{\langle\alpha_{g1}\rangle}{\langle\rho_g\rangle}\langle\langle v_{g1}\rangle\rangle\frac{d\langle\rho_g\rangle}{dz}\right\}$, $\langle\phi_{Conv,1}\rangle=-\langle a_{i,1}\rangle\frac{d\langle\langle v_{g1}\rangle\rangle}{dz}$, $\langle\phi_{DP,2}\rangle=-\kappa\left(\frac{\langle a_{i,2}\rangle}{\langle\alpha_{g2}\rangle}\right)\left\{\frac{\langle\alpha_{g2}\rangle}{\langle\rho_g\rangle}\langle\langle v_{g2}\rangle\rangle\frac{d\langle\rho_g\rangle}{dz}\right\}$, $\langle\phi_{Conv,2}\rangle=-\langle a_{i,2}\rangle\frac{d\langle\langle v_{g2}\rangle\rangle}{dz}$.
Condensation model Based on: Park et al. (2007) Zeitoun (1994)	$\langle\phi_{CO,1}\rangle=-\pi\beta_{bc}^2\langle D_{Sm,1}\rangle^2\langle n_{b1}\rangle\frac{4\langle Nu_{c1}\rangle\langle Ja\rangle\langle\alpha_t\rangle}{\langle D_{Sm,1}\rangle^2(1-\beta_{bc}^2)}$, $\langle\eta_{CO,1}\rangle=-\frac{\pi\beta_{bc}^3\langle D_{Sm,1}\rangle^3}{6}\langle n_{b1}\rangle\frac{4\langle Nu_{c1}\rangle\langle Ja\rangle\langle\alpha_t\rangle}{\langle D_{Sm,1}\rangle^2(1-\beta_{bc}^2)}$, $\langle\eta_{PC,1}\rangle=-\pi(1-p_c)\langle D_{Sm,1}\rangle\langle n_{b1}\rangle\langle Nu_c\rangle\langle Ja\rangle\langle\alpha_t\rangle$, $\langle\eta_{PC,2}\rangle=-\langle A_{b2}\rangle\langle n_{b2}\rangle\frac{\langle Nu_{c2}\rangle}{L_c}\langle Ja\rangle\langle\alpha_t\rangle$, $\langle\phi_{PC,1}\rangle=\frac{2}{3}\left(\frac{\langle a_{i,1}\rangle}{\langle\alpha_{g1}\rangle}\right)\langle\eta_{PC,1}\rangle$, $\langle\phi_{PC,2}\rangle=\kappa\left(\frac{\langle a_{i,2}\rangle}{\langle\alpha_{g2}\rangle}\right)\langle\eta_{PC,2}\rangle$, $\langle Nu_{c1}\rangle=2.04\,\mathrm{Re}_{b1}^{0.61}\alpha_{g1}^{0.328}\mathrm{Ja}^{-0.308}$, $\langle Nu_{c2}\rangle=0.023\,\mathrm{Re}_{b1}^{0.8}\,\mathrm{Pr}_f^{0.4}$, $\langle\mathrm{Re}_{b1}\rangle=\frac{\rho_f\langle U_{b1}\rangle\langle D_{bc,1}\rangle}{\mu_f}$, $\langle\mathrm{Re}_{b2}\rangle=\frac{\rho_f\langle U_{b2}\rangle\langle D_{Sm,2}\rangle}{\mu_f}$, $\langle U_{b1}\rangle=\frac{\sqrt{2}}{1-\langle\alpha_{g1}\rangle}\left(\frac{\Delta\rho g\sigma}{\rho_f^2}\right)^{1/4}\left(1-\langle\alpha_{g1}\rangle\right)^{7/4}$, $\langle U_{b2}\rangle=\frac{0.35}{1-\langle\alpha_{g2}\rangle}\left(\frac{\Delta\rho g D_h}{\rho_f}\right)^{1/4}$, $\langle Ja\rangle=\frac{\rho_f c_{pf}\left(\langle T_{sat}\rangle-\langle T_f\rangle\right)}{\rho_g h_{fg}}$, $\langle D_{bc,1}\rangle=\beta_{bc}\langle D_{Sm,1}\rangle$.

Table C.2 (*cont.*)

Model and contr. work	**Equations**
Inter-group transfer terms	$\left\langle \eta_{\Delta m_{12}} \right\rangle = \sum_j \left\langle \eta_{j,12} \right\rangle + \max\left(0, \left\langle \eta_{V,12} \right\rangle\right) + \min\left(0, \left\langle \eta_{V,21} \right\rangle\right),$ $\left\langle \eta_{V,12} \right\rangle = \left\langle \eta_{\Gamma,12} \right\rangle + \left\langle \eta_{DP,12} \right\rangle,\ \left\langle \eta_{V,21} \right\rangle = \left\langle \eta_{\Gamma,21} \right\rangle + \left\langle \eta_{DP,21} \right\rangle,$ $\left\langle \phi_{\Delta m_{12}} \right\rangle = \sum_j \left\langle \phi_{j,12} \right\rangle + \max\left(0, \left\langle \phi_{V,12} \right\rangle\right) + \min\left(0, \left\langle \phi_{V,21} \right\rangle\right),$ $\left\langle \phi_{V,12} \right\rangle = \left\langle \phi_{\Gamma,12} \right\rangle + \left\langle \phi_{DP,12} \right\rangle,\ \left\langle \phi_{V,21} \right\rangle = \left\langle \phi_{\Gamma,21} \right\rangle + \left\langle \phi_{DP,21} \right\rangle,$ $\left\langle \eta_{\Gamma,12} \right\rangle = \chi_1 \left(\frac{D_c}{\left\langle D_{Sm,1} \right\rangle} \right)^3 \left(\frac{\left\langle \Gamma_{g1} \right\rangle - \left\langle \eta_{CO,1} \right\rangle \left\langle \rho_g \right\rangle}{\left\langle \rho_g \right\rangle} \right),$ $\left\langle \eta_{DP,12} \right\rangle = -\chi_1 \left(\frac{D_c}{\left\langle D_{Sm,1} \right\rangle} \right)^3 \left(\frac{\left\langle \alpha_{g1} \right\rangle}{\left\langle \rho_g \right\rangle} \right) \left\langle \left\langle v_{g1} \right\rangle \right\rangle \frac{d\left\langle \rho_g \right\rangle}{dz},$ $\left\langle \eta_{\Gamma,21} \right\rangle = \chi_2 \left(\frac{D_c}{\left\langle D_{Sm,2} \right\rangle} \right)^3 \frac{\left\langle \Gamma_{g2} \right\rangle}{\left\langle \rho_g \right\rangle},\quad \left\langle \eta_{DP,21} \right\rangle = -\chi_2 \left(\frac{D_c}{\left\langle D_{Sm,2} \right\rangle} \right)^3 \left(\frac{\left\langle \alpha_{g2} \right\rangle}{\left\langle \rho_g \right\rangle} \right) \left\langle \left\langle v_{g2} \right\rangle \right\rangle \frac{d\left\langle \rho_g \right\rangle}{dz},$ $\left\langle \phi_{\Gamma,12} \right\rangle = \chi_1 \left(\frac{D_c}{\left\langle D_{Sm,1} \right\rangle} \right)^2 \left(\frac{\left\langle a_{i,1} \right\rangle}{\left\langle \alpha_{g1} \right\rangle} \right) \left(\frac{\left\langle \Gamma_{g1} \right\rangle - \left\langle \eta_{CO,1} \right\rangle \left\langle \rho_g \right\rangle}{\left\langle \rho_g \right\rangle} \right),\ \left\langle \phi_{\Gamma,21} \right\rangle = \chi_2 \left(\frac{D_c}{\left\langle D_{Sm,2} \right\rangle} \right)^2 \left(\frac{\left\langle a_{i,2} \right\rangle}{\left\langle \alpha_{g2} \right\rangle} \right) \frac{\left\langle \Gamma_{g2} \right\rangle}{\left\langle \rho_g \right\rangle},$ $\left\langle \phi_{DP,12} \right\rangle = -\chi_1 \left(\frac{D_c}{\left\langle D_{Sm,1} \right\rangle} \right)^2 \left(\frac{\left\langle a_{i,1} \right\rangle}{\left\langle \alpha_{g1} \right\rangle} \right) \left(\frac{\left\langle \alpha_{g1} \right\rangle}{\left\langle \rho_g \right\rangle} \right) \left\langle \left\langle v_{g1} \right\rangle \right\rangle \frac{d\left\langle \rho_g \right\rangle}{dz},$ $\left\langle \phi_{DP,21} \right\rangle = -\chi_2 \left(\frac{D_c}{\left\langle D_{Sm,2} \right\rangle} \right)^2 \left(\frac{\left\langle a_{i,2} \right\rangle}{\left\langle \alpha_{g2} \right\rangle} \right) \left(\frac{\left\langle \alpha_{g2} \right\rangle}{\left\langle \rho_g \right\rangle} \right) \left\langle \left\langle v_{g2} \right\rangle \right\rangle \frac{d\left\langle \rho_g \right\rangle}{dz}.$
Coefficients Based on: Nukiyama-Tanasawa distribution	$\chi_1 = 4.5 \left(\frac{D_c}{\left\langle D_{Sm,1} \right\rangle} \right)^3 \exp\left(-3 \frac{D_c}{\left\langle D_{Sm,1} \right\rangle} \right),\quad \chi_2 = \chi_1 \frac{\left\langle n_{b1} \right\rangle}{\left\langle n_{b2} \right\rangle},$ $\psi_1 = \psi_2 = \frac{1}{36\pi},\ \kappa = \frac{2}{3}$ $\left\langle A_{b2} \right\rangle = \pi \left\langle D_{Sm,2} \right\rangle^2, \beta_{bc} = 0.4, L_c = \max\left(0.25G, \left\langle D_{Sm,1} \right\rangle\right).$
Drift-Flux model (DFM) Based on: Zuber and Findlay (1965) Ishii (1977) Brooks et al. (2012a)	$\left\langle \left\langle v_{g1} \right\rangle \right\rangle = C_{o1} \left\langle j \right\rangle + \left\langle \left\langle v_{gj,1} \right\rangle \right\rangle, \left\langle \left\langle v_{g2} \right\rangle \right\rangle = C_{o2} \left\langle j \right\rangle + \left\langle \left\langle v_{gj,2} \right\rangle \right\rangle,$ $C_{o1} = \left[C_\infty - \left(C_\infty - 1 \right) \sqrt{\frac{\rho_g}{\rho_f}} \right], C_{o2} = \left[C_\infty - \left(C_\infty - 1 \right) \sqrt{\frac{\rho_g}{\rho_f}} \right],$ $\left\langle \left\langle v_{gj,1} \right\rangle \right\rangle = \sqrt{2} \left(\frac{\Delta\rho g \sigma_i}{\rho_f^2} \right)^{0.25} \left(1 - \left\langle \alpha_{g1} \right\rangle \right)^{7/4}, \left\langle \left\langle v_{gj,2} \right\rangle \right\rangle = 0.35 \left(\frac{\Delta\rho g D_h}{\rho_f} \right)^{0.5},$ $\left\langle j_g \right\rangle = \left\langle \left\langle v_{gj,1} \right\rangle \right\rangle \left\langle \alpha_{g1} \right\rangle + \left\langle \left\langle v_{gj,2} \right\rangle \right\rangle \left\langle \alpha_{g2} \right\rangle, \left\langle j_f \right\rangle = \frac{G - \rho_g \left\langle j_g \right\rangle}{\rho_f},$ $\left\langle j \right\rangle = \left\langle j_g \right\rangle + \left\langle j_f \right\rangle.$

Table C.2 (*cont.*)

Model and contr. work	Equations
Interaction mechanisms area sources/sink terms Based on: Sun et al. (2004a)	$\left\langle \phi_{RC}^{(1)} \right\rangle = -0.17 C_{RC}^{(1)} \frac{\varepsilon^{1/3} \left\langle \alpha_{g1} \right\rangle^{1/3} \left\langle a_{i,1} \right\rangle^{5/3}}{\alpha_{g1,\max}^{1/3} \left(\alpha_{g1,\max}^{1/3} - \left\langle \alpha_{g1} \right\rangle^{1/3} \right)} \left[1 - \exp\left(-C_{RC1} \frac{\alpha_{g1,\max}^{1/3} \left\langle \alpha_{g1} \right\rangle^{1/3}}{\left(\alpha_{g1,\max}^{1/3} - \left\langle \alpha_{g1} \right\rangle^{1/3} \right)} \right) \right]$ $\left\langle \phi_{RC}^{(2)} \right\rangle = -13.6 C_{RC}^{(2)} \frac{\left\langle \alpha_{g2} \right\rangle^2 \varepsilon^{1/3}}{W^2 W_G} \left\langle R_{2,\max} \right\rangle^{4/3} \left(1 - 2.0 \left\langle R_c^* \right\rangle^2 + \frac{9.0 W_G}{\left\langle R_{2,\max} \right\rangle} \right) \left[1 - \exp\left(-C_{RC2} \left\langle \alpha_{g2} \right\rangle^{1/2} \right) \right]$ $\left\langle \phi_{RC,1}^{(12,2)} \right\rangle = -4.85 C_{RC}^{(12,2)} \frac{\varepsilon^{1/3} \left\langle a_{i,1} \right\rangle \left\langle \alpha_{g1} \right\rangle^{2/3} \left\langle \alpha_{g2} \right\rangle^2}{\left\langle R_{2,\max} \right\rangle^{2/3}} \left[1 - \exp\left(-C_{RC1} \frac{\alpha_{g1,\max}^{1/3} \left\langle \alpha_{g1} \right\rangle^{1/3}}{\left(\alpha_{g1,\max}^{1/3} - \left\langle \alpha_{g1} \right\rangle^{1/3} \right)} \right) \right]$ $\left\langle \phi_{RC,2}^{(12,2)} \right\rangle = 13.6 C_{RC}^{(12,2)} \frac{\varepsilon^{1/3} \left\langle \alpha_{g1} \right\rangle^{5/3} \left\langle \alpha_{g2} \right\rangle^2}{\left\langle R_{2,\max} \right\rangle^{2/3} W_G} \left(1 + \frac{10.3 W_G}{\left\langle R_{2,\max} \right\rangle} \right) \left[1 - \exp\left(-C_{RC1} \frac{\alpha_{g1,\max}^{1/3} \left\langle \alpha_{g1} \right\rangle^{1/3}}{\left(\alpha_{g1,\max}^{1/3} - \left\langle \alpha_{g1} \right\rangle^{1/3} \right)} \right) \right]$ $\left\langle \phi_{RC,2}^{(11,2)} \right\rangle = 0.68 C_{RC}^{(1)} \frac{\varepsilon^{1/3} \left\langle \alpha_{g2} \right\rangle^2 \left\langle a_{i,1} \right\rangle^{2/3}}{\alpha_{g1,\max}^{2/3} W_G} \left[1 - \exp\left(-C_{RC1} \frac{\alpha_{g1,\max}^{1/3} \left\langle \alpha_{g1} \right\rangle^{1/3}}{\left(\alpha_{g1,\max}^{1/3} - \left\langle \alpha_{g1} \right\rangle^{1/3} \right)} \right) \right]$ $\left[1 + 0.7 W_G^{7/6} \left(\left\langle a_{i,1} \right\rangle \Big/ \left\langle \alpha_{g1} \right\rangle \right)^{1/2} \left(\frac{\sigma}{g \Delta\rho} \right)^{-1/3} \right] \left(1 - \frac{2}{3} \left\langle D_{c1}^* \right\rangle \right)$ $\left\langle \phi_{\mathrm{WE}}^{(1)} \right\rangle = -0.27 C_{WE}^{(1)} \left\langle v_{r,1} \right\rangle \left\langle C_{D,1} \right\rangle^{1/3} \left\langle a_{i,1} \right\rangle^2$ $\left\langle \phi_{\mathrm{WE}}^{(2)} \right\rangle = -15.9 C_{WE}^{(2)} \frac{\left\langle \alpha_{g2} \right\rangle^2}{\left\langle R_{2,\max}^2 \right\rangle} \sqrt{\left\langle C_{D,2} \right\rangle g W_G} \left(1 + 0.51 \left\langle R_c^* \right\rangle \right)$ $\left\langle \phi_{\mathrm{WE},2}^{(11,2)} \right\rangle = 1.08 C_{WE}^{(11,2)} \left\langle v_{r,1} \right\rangle \left\langle C_{D,1} \right\rangle^{1/3} \frac{\left\langle a_{i,1} \right\rangle \left\langle \alpha_{g1} \right\rangle}{\left\langle R_{2,\max} \right\rangle} \left(1 - \frac{2}{3} \left\langle D_{c1}^* \right\rangle \right) \left[1 + 0.7 W_G \left(\frac{\left\langle a_{i,1} \right\rangle}{\left\langle \alpha_{g1} \right\rangle} \right)^{1/2} \left(\frac{\sigma}{g \Delta\rho} \right)^{-1/3} \right]$ $\left\langle \phi_{\mathrm{WE},1}^{(12,2)} \right\rangle = -4.35 C_{WE}^{(12,2)} \sqrt{g \left\langle C_{D,2} \right\rangle W_G} \frac{\left\langle a_{i,1} \right\rangle \left\langle \alpha_{g2} \right\rangle}{\left\langle R_{2,\max} \right\rangle}$ $\left\langle \phi_{\mathrm{WE},2}^{(12,2)} \right\rangle = 26.1 C_{WE}^{(12,2)} \left\langle \alpha_{g1} \right\rangle \left\langle \alpha_{g2} \right\rangle \sqrt{\frac{g \left\langle C_{D,2} \right\rangle}{W_G}} \frac{1}{\left\langle R_{2,\max} \right\rangle} \left(1 + 4.31 \frac{G}{\left\langle R_{2,\max} \right\rangle} \right)$ $\left\langle \phi_{\mathrm{TI},1}^{(1)} \right\rangle = 0.12 C_{TI}^{(1)} \frac{\varepsilon^{1/3} \left(1 - \left\langle \alpha_{gt} \right\rangle \right) \left\langle a_{i,1} \right\rangle^{5/3}}{\left\langle \alpha_{g1} \right\rangle^{2/3}} \exp\left(-\frac{We_{c,TI1}}{We_1} \right) \sqrt{\left(1 - \frac{We_{c,TI1}}{We_1} \right)}$ $\left\langle \phi_{\mathrm{TI},2}^{(2)} \right\rangle = 1.4 C_{TI}^{(2)} \frac{\varepsilon^{1/3} \left\langle \alpha_{g2} \right\rangle \left(1 - \left\langle \alpha_{gt} \right\rangle \right) W_G \left(1 - 2 \left\langle R_c^* \right\rangle \right)}{\left\langle R_{2,\max} \right\rangle^{8/3}} \exp\left(-\frac{We_{c,TI2}}{We_2} \right) \sqrt{\left(1 - \frac{We_{c,TI2}}{We_2} \right)}$ $\left\langle \phi_{\mathrm{TI},1}^{(2,1)} \right\rangle = 2.71 C_{TI}^{(2)} \frac{\varepsilon^{1/3} \left\langle \alpha_{g2} \right\rangle \left(1 - \left\langle \alpha_{gt} \right\rangle \right) W_G^{2/3} \left\langle R_c^* \right\rangle^{5/3} \left(1 - \left\langle R_c^* \right\rangle^{5/3} \right)}{\left\langle R_{2,\max} \right\rangle^{7/3}} \exp\left(-\frac{We_{c,TI2}}{We_2} \right) \sqrt{\left(1 - \frac{We_{c,TI2}}{We_2} \right)}$

Table C.2 (*cont.*)

Model and contr. work	Equations
Interaction mechanisms area sources/sink terms (cont.)	$\left\langle \phi_{SO,1}^{(2,12)} \right\rangle = 64.51 C_{SO} C_d^2 \dfrac{\left\langle \alpha_{g2} \right\rangle \left\langle v_{r2} \right\rangle}{W_G \left\langle R_{2,\max} \right\rangle} \left(1 - \left(- \dfrac{We_{c,\mathrm{SO}}}{We_{2,\max}} \right)^3 \right)$ $\left\langle \phi_{SO,2}^{(2,12)} \right\rangle = -21.50 C_{SO} C_d^3 \left(\dfrac{\sigma}{\rho_f} \right)^{3/5} \dfrac{\left\langle \alpha_{g2} \right\rangle}{\left\langle v_{rb} \right\rangle_i^{1/5} W_G^{8/5} \left\langle R_{2,\max} \right\rangle} \left[\begin{array}{l} 1 - \left(\dfrac{We_{c,\mathrm{SO}}}{We_{2,\max}} \right)^3 \\ + \dfrac{3.24G}{\left\langle R_{2,\max} \right\rangle} \left(1 - \left(\dfrac{We_{c,\mathrm{SO}}}{We_{2,\max}} \right)^2 \right) \end{array} \right]$ $\left\langle \phi_{SI}^{(2)} \right\rangle = 1.25 \left\langle \alpha_{g2} \right\rangle^2 \left(\dfrac{\sigma}{g \Delta \rho} \right)^{-1} \left[\begin{array}{l} C_{RC}^{(2)} \dfrac{\varepsilon^{1/3}}{W^2} \left(\dfrac{\sigma}{g \Delta \rho} \right)^{7/6} \left\{ 1 - \exp\left(-C_{RC2} \left\langle \alpha_{g2} \right\rangle^{1/2} \right) \right\} \\ + 2.3.10^{-4} C_{WE}^{(2)} \sqrt{\left\langle C_{D,2} \right\rangle g W_G} \end{array} \right]$ *Where,* $\sum_j \left\langle \phi_{j,1} \right\rangle = \left\langle \phi_{RC}^{(1)} \right\rangle + \left\langle \phi_{RC,1}^{(12,2)} \right\rangle + \left\langle \phi_{\mathrm{WE}}^{(1)} \right\rangle + \left\langle \phi_{\mathrm{WE}}^{(12,2)} \right\rangle + \left\langle \phi_{\mathrm{TI},1}^{(1)} \right\rangle + \left\langle \phi_{\mathrm{TI},1}^{(2,1)} \right\rangle + \left\langle \phi_{SO,1}^{(2,12)} \right\rangle,$ $\sum_j \left\langle \phi_{j,2} \right\rangle = \left\langle \phi_{RC}^{(2)} \right\rangle + \left\langle \phi_{RC,2}^{(11,2)} \right\rangle + \left\langle \phi_{RC,2}^{(12,2)} \right\rangle + \left\langle \phi_{\mathrm{WE},2}^{(11,2)} \right\rangle + \left\langle \phi_{\mathrm{WE},2}^{(12,2)} \right\rangle + \left\langle \phi_{\mathrm{TI},1}^{(2)} \right\rangle + \left\langle \phi_{SO,2}^{(2,12)} \right\rangle + \left\langle \phi_{SI}^{(2)} \right\rangle.$ $C_{RC}^{(1)} = 0.005,\ C_{RC}^{(2)} = 0.005, C_{RC}^{(12,2)} = 0.005,\ C_{RC2} = 3.0, C_{WE}^{(1)} = 0.002, C_{WE}^{(2)} = 0.002, C_{WE}^{(12,2)} = 0.002,$ $C_{TI}^{(1)} = 0.03,\ C_{TI}^{(2)} = 0.02, C_{SO} = 3.8.10^{-5}, C_d = 4.80, We_{c,TI2} = 7.0, We_{c,SO} = 4500, \alpha_{\max} = 0.62$ $\left\langle R_c^* \right\rangle = \dfrac{D_c / 2}{\left\langle R_{2,\max} \right\rangle}, \left\langle D_{c1}^* \right\rangle = \dfrac{D_c}{\left\langle D_{Sm,1} \right\rangle}, D_c = 1.7 W_G^{1/3} \left(\dfrac{\sigma}{g \Delta \rho} \right)^{1/3}$ $\left\langle \alpha_{gt} \right\rangle = \left\langle \alpha_{g1} \right\rangle + \left\langle \alpha_{g2} \right\rangle, \left\langle C_{D,1} \right\rangle = \dfrac{24 \left(1 + 0.1 \left\langle \mathrm{Re}_{b1} \right\rangle^{0.75} \right)}{\left\langle \mathrm{Re}_{b1} \right\rangle}, \left\langle C_{D,2} \right\rangle = 8/3 \left(1 - \left\langle \alpha_{gt} \right\rangle \right)^2,$ $\left\langle \mathrm{Re}_{b1} \right\rangle = \dfrac{\left(1 - \left\langle \alpha_{gt} \right\rangle \right) \left\langle v_{r1} \right\rangle \left\langle D_{Sm,1} \right\rangle}{\nu_f}, \left\langle v_{r1} \right\rangle = \sqrt{\dfrac{4 g \left\langle D_{Sm,1} \right\rangle \Delta \rho}{3 \left\langle C_{D,1} \right\rangle \rho_f}}, \left\langle v_{r2} \right\rangle = 0.35 \sqrt{\dfrac{\sigma}{g \Delta \rho}}.$
Interaction mechanisms volume sources/sink terms Based on: Sun et al. (2004a)	$\sum_j \left\langle \eta_{j,2} \right\rangle = \left\langle \eta_{RC,2}^{(11,2)} \right\rangle + \left\langle \eta_{RC,2}^{(12,2)} \right\rangle + \left\langle \eta_{WE,2}^{(11,2)} \right\rangle + \left\langle \eta_{WE,2}^{(12,2)} \right\rangle + \left\langle \eta_{TI,2}^{(2,1)} \right\rangle + \left\langle \eta_{SO}^{(2,12)} \right\rangle,$ $\left\langle \eta_{RC,2}^{(11,2)} \right\rangle = 3.4 C_{RC}^{(1)} \dfrac{\varepsilon^{1/3} \left\langle \alpha_{g2} \right\rangle^2 \left\langle a_{i,1} \right\rangle^{2/3}}{\alpha_{g1,\max}^{2/3}} \left[1 - \exp\left(-C_{RC1} \dfrac{\alpha_{g1,\max}^{1/3} \left\langle \alpha_{g1} \right\rangle^{1/3}}{\left(\alpha_{g1,\max}^{1/3} - \left\langle \alpha_{g1} \right\rangle^{1/3} \right)} \right) \right] \left(1 - \dfrac{2}{3} \left\langle D_{c1}^* \right\rangle \right)$ $\left\langle \eta_{RC,2}^{(12,2)} \right\rangle = 4.85 C_{RC}^{(12,2)} \dfrac{\varepsilon^{1/3} \left\langle \alpha_{g1} \right\rangle^{5/3} \left\langle \alpha_{g2} \right\rangle^2}{\left\langle R_{2,\max} \right\rangle^{2/3}} \left[1 - \exp\left(-C_{RC1} \dfrac{\alpha_{g1,\max}^{1/3} \left\langle \alpha_{g1} \right\rangle^{1/3}}{\left(\alpha_{g1,\max}^{1/3} - \left\langle \alpha_{g1} \right\rangle^{1/3} \right)} \right) \right]$ $\left\langle \eta_{WE,2}^{(11,2)} \right\rangle = 5.40 C_{WE}^{(11,2)} \left\langle v_{r1} \right\rangle \left\langle C_{D,1} \right\rangle^{1/3} \left\langle \alpha_{g1} \right\rangle \left\langle a_{i,1} \right\rangle \left(1 - \dfrac{2}{3} \left\langle D_{c1}^* \right\rangle \right)$ $\left\langle \eta_{WE,2}^{(12,2)} \right\rangle = 4.35 C_{WE}^{(12,2)} \sqrt{W_G g \left\langle C_{D,2} \right\rangle} \dfrac{\left\langle \alpha_{g1} \right\rangle \left\langle \alpha_{g2} \right\rangle}{\left\langle R_{2,\max} \right\rangle}$ $\left\langle \eta_{TI,2}^{(2,1)} \right\rangle = -0.34 C_{TI}^{(2)} \left\langle \alpha_{g2} \right\rangle \left(1 - \left\langle \alpha_{gt} \right\rangle \right) \dfrac{W_G \varepsilon^{1/3} \left\langle R_c^* \right\rangle^{7/3} \left(1 - \left\langle R_c^* \right\rangle^{5/3} \right)}{\left\langle R_{2,\max} \right\rangle^{5/3}} \exp\left(- \dfrac{We_{c,TI2}}{We_2} \right) \sqrt{\left(1 - \dfrac{We_{c,TI2}}{We_2} \right)}$ $\left\langle \eta_{SO}^{(2,12)} \right\rangle = -10.75 C_{SO} C_d^3 \left(\dfrac{\sigma}{W_G \rho_f} \right)^{3/5} \dfrac{\left\langle \alpha_{g2} \right\rangle}{\left\langle v_{r2} \right\rangle \left\langle R_{2,\max} \right\rangle} \left(1 - \left(- \dfrac{We_{c,\mathrm{SO}}}{We_{2,\max}} \right)^3 \right).$